universität wien

MASTERARBEIT | MASTER'S THESIS

Titel | Title

The Existence and Formation Dynamics of Supramolecular Chains in Equilibrated and Sheared Ring Polymer Melts

verfasst von | submitted by

Nora-Elen Giesinger BSc

angestrebter akademischer Grad | in partial fulfilment of the requirements for the degree of

Master of Science (MSc)

Wien | Vienna, 2025

Studienkennzahl lt. Studienblatt | Degree programme code as it appears on the student record sheet:	UA 066 876
Studienrichtung lt. Studienblatt | Degree programme as it appears on the student record sheet:	Masterstudium Physics
Betreut von | Supervisor:	Univ.-Prof. Dipl.-Ing. Dr. Christos Likos
Mitbetreut von | Co-Supervisor:	Jan Smrek PhD

Acknowledgements

I would like to express my sincere gratitude to all those who have supported me during the course of my master thesis.

First and foremost, I am deeply grateful to my supervisor, Jan Smrek, for overseeing my thesis and providing valuable guidance throughout the process. I would also like to thank him for always having an open ear to my concerns and for his constant support with complex tasks.

I would like to thank Christos Likos for sparking my interest for soft matter physics and hosting me in his research group during my master project.

I am also thankful to my fellow master and PhD students in the research group—Lydia Morscher, Sadia Schülke, Rayhaneh Afghahi Ferimani, Lisa Sappl and Maximilian Negedly—who were always willing to listen to my problems, helped me think through difficult concepts, and offered emotional support during tough moments.

Finally, I would like to express my deepest gratitude to my family and friends for their unwavering emotional support throughout this journey. A special thanks to my boyfriend, Arthur Wostry, whose encouragement and understanding were invaluable to me.

Thank you all for making this thesis possible.

Abstract

Despite significant advances in polymer physics, the entanglement mechanisms between ring polymers remain largely unexplored. This thesis investigates the existence and formation dynamics of deadlocks - temporary topological constraints that can form between rings - in melts of nonconcatenated and unknotted rings under both equilibrium and steady-state shear conditions.

To enable this investigation, we enhanced an existing topology-based deadlock detection algorithm, allowing for a more detailed classification of the deadlocked state by defining a new statistical quantity: the degree of deadlocking $\xi(t)$.

Under equilibrium conditions, we find that deadlocks are a natural feature of the ring polymer melt, with a population of deadlocked pairs constituting approximately 1% of all linearly non-separable pairs. Among these, only 5% exhibit a strong deadlocked state. The degree of deadlocking is strongly correlated with the persistence of deadlocked pairs: those with a low degree of deadlocking disentangle rapidly, while those with a high degree exhibit meta-stability, persisting for several diffusion times. Static analysis reveals that deadlocked pairs with a high degree of deadlocking maintain closer center-of-mass distances and share significant overlap in volume, while low-deadlocking pairs show minimal overlap and more elongated conformations. Dynamically, although individual chain motion remains largely unaffected by deadlocks, the relative mean squared displacement between highly deadlocked rings plateaus, indicating a maximal separation distance comparable the center of mass distance between deadlocked pairs.

Under steady-state shear conditions, we examine the behavior of deadlocks in melts at two shear rates: Wi = 8.8 and Wi = 30.0. Our findings show that the number of deadlocks is significantly higher under shear compared to equilibrium, with pairs exhibiting a high degree of deadlocking being more than 15 times as frequent. We observe two distinct regimes for the degree of deadlocking: (A) pairs with a low degree of deadlocking disentangle rapidly, with the population fluctuating around a mean value, and (B) pairs with a high degree of deadlocking, which persist for longer times and exhibit periodic deviations from the mean. These periodic fluctuations suggest an underlying physical mechanism, potentially related to the tumbling dynamics of the melt.

We devised a method to detect and classify entanglements in rings and showed them being relevant in dynamical context in- and out- of equilibrium.

Deutschsprachiger Abstrakt

Trotz erheblicher Fortschritte in der Polymerphysik sind die Entanglementmechanismen zwischen Ringpolymeren noch weitgehend unerforscht. Diese Arbeit untersucht die Existenz- und Bildungsdynamik von Deadlocks – temporäre topologische Einschränkungen, die sich zwischen Ringen bilden können – im Schmelzen von nicht verketteten und unverknoteten Ringen unter Gleichgewichts- und stationären Scherbedingungen.

Um diese Untersuchung zu ermöglichen, haben wir einen bestehenden topologiebasierten Deadlock-Erkennungsalgorithmus erweitert, der eine detailliertere Klassifizierung des Deadlock-Zustands ermöglicht, indem wir eine neue statistische Größe definieren: den Deadlock-Grad $\xi(t)$.

Unter Gleichgewichtsbedingungen zeigen unsere Ergebnisse, dass Deadlocks ein natürliches Merkmal der Ringpolymerschmelze sind, wobei die Population von Deadlock-Paaren etwa 1% aller linear nicht trennbaren Paare ausmacht. Von diesen weisen nur 5% einen starken Deadlock-Zustand auf. Der Deadlock-Grad korreliert stark mit der Lebensdauer von Deadlock-Paaren: Paare mit einem geringen Deadlock-Grad entwirren sich schnell, während Paare mit einem hohen Grad Metastabilität aufweisen und mehrere Diffusionszeiten lang bestehen bleiben. Statische Analysen zeigen, dass Deadlock-Paare mit einem hohen Deadlock-Grad engere Schwerpunktsabstände beibehalten und eine signifikante Überlappung im Volumen aufweisen, während Paare mit einem geringen Deadlock-Grad nur eine minimale Überlappung und eine stärkere Anisotropie der Konformationen aufweisen. Obwohl die Bewegung einzelner Ketten dynamisch weitgehend unbeeinflusst von Deadlocks bleibt, erreicht die relative mittlere quadrierte Verschiebung zwischen stark deadlocked Ringen ein Plateau, was auf einen maximalen Trennungsabstand hinweist, der mit dem Schwerpunktabstand zwischen deadlocked Paaren vergleichbar ist.

Unter stationären Scherbedingungen untersuchen wir das Verhalten von Deadlocks in Schmelzen bei zwei Scherraten: $\mathrm{Wi} = 8,8$ und $\mathrm{Wi} = 30,0$. Unsere Ergebnisse zeigen, dass die Anzahl der Deadlocks unter Scherbedingungen deutlich höher ist als im Gleichgewicht, wobei Paare mit hohem Deadlock-Grad mehr als 15-mal häufiger auftreten. Wir beobachten zwei unterschiedliche Regime abhängig vom Deadlocking-Grad: (A) Paare mit einem niedrigen Deadlocking-Grad entwirren sich schnell, wobei die Population um einen Mittelwert schwankt, und (B) Paare mit einem hohen Deadlocking-Grad bleiben über längere Zeit bestehen und weisen periodische Abweichungen vom Mittelwert auf. Diese periodischen Schwankungen deuten auf einen zugrunde liegenden physikalischen Mechanismus hin, der möglicherweise mit der Tumblingdynamik der Schmelze unter Scheerung zusammenhängt.

Deutschsprachiger Abstrakt

Wir haben eine Methode entwickelt, um Deadlocks in Ringen zu erkennen und zu klassifizieren, und gezeigt, dass sie im dynamischen Kontext sowohl im als auch außerhalb des Gleichgewichts relevant sind.

Contents

1. Introduction

Entanglement in polymer systems is a fascinating yet complex phenomenon. Despite extensive research in flexible linear and branched polymer systems [1, 2], the entanglement mechanisms of different polymer architectures are still not fully understood [3]. Understanding how entanglements form and evolve, particularly in complex polymer architectures like ring polymers, remains a significant challenge in polymer physics, mainly because of two reasons: first, entanglements are complex many-body effects making them computationally expensive, and second, for ring polymers, the fixed topology - where the chains must remain unlinked and unknotted - introduces nonlocal constraints that make theoretical models difficult to apply.

This thesis focuses on investigating entanglements in ring polymer melt systems. Unlike systems of linear polymers, which are well-studied and understood through established models [1, 2], ring polymers have limited theoretical understanding. As a result, very little is known about how entanglements manifest in ring polymers - or whether they even form at all and what is their nature.

In equilibrium, flexible linear polymers in a melt adopt random coil conformations [2]. As a consequence of their equilibrium conformation, each segment of the polymer chain is surrounded almost exclusively by other chains [4], creating a dense environment where each polymer chain interacts with multiple neighboring chains. This number of neighboring chains scales as $N^{1/2}$, where N is the degree of polymerization. These conformations lead to entanglements, where the motion of one linear chain is hindered by the presence of neighboring chains, forming complex entanglement networks [2]. These entanglements affect the polymers dynamics and the *tube* or *reptation model* [1, 2] is often used to describe their motion. According to this model, the polymer chains are confined to a *tube-like* region defined by the surrounding chains, and their motion is largely limited to one dimensional diffusion along the tube. As the ends of the chain are free to move, they mediate the chains conformational changes within the confining tube [5].

Flexible ring polymers in a melt, in contrast, present a different challenge to our understanding of entanglement. These polymer do not have free ends, and as a result, their behavior deviates from that of linear polymer systems [5]. Although a ring polymer might, in principle, form a linear chain if folded, this conformation is entropically unfavorable. Instead, ring polymers adopt branched conformations, which include multiple "ends", leading to complex interactions. Furthermore, these branched structures allow for mutual threading of the rings, complicating their description further. Threadings between two rings refers to a geometrical configuration, where a section of one polymer ring passes

through an opening created by another ring.
While linear chains in a melt adopt random coil conformations, ring polymers tend to adopt more compact, globular conformations [6]. As a consequence of the equilibrium conformations, the rings do not exhibit entanglements in the same *tube-like* sense that linear chains do. Some entanglements have been identified in ring systems and were termed *deadlocks* or *supramolecular chains*. A deadlock is a temporary topological restriction, formed by a mutual threading between two rings. The existence and behavior of these deadlocks are largely unexplored.

Recent studies have begun to shed light on the phenomenon of ring polymer entanglements. Under specific stress conditions, such as uniaxial stretching, deadlocks have been observed to form in ring polymer melts. A recent experimental study [6] observed a unique stress-relaxation response of the system, where the viscosity of the material increases dramatically at low stretch rates ($\mathrm{Wi} \ll 1$). A computational study [7] further investigated the unusual response of the ring polymer melt to weak elongational flow. While linear chains elongate independently during extension, some rings spontaneously assemble into supramolecular chains that are stabilized and pulled tight by the flow. These supramolecular chains dominate the nonlinear viscosity and the viscosity thickening of the material directly coincides with the elongation of the supramolecular chains, emphasizing the role of deadlocks in the rheology of ring melts.
Additionally, a study by Micheletti et al. [8] investigated a system of active ring polymers in a melt, where part of the ring is modeled at a higher effective temperature. By introducing an active part on the chains, stresses are generated internally. After the onset of activity, more and more rings participate in a growing web of deadlocked states. This deadlocked cluster entraps other rings by threadings, eventually resulting in the complete arrest of the system. Despite these findings, the role of deadlocks in the equilibrium state of the ring polymer melt, in the absence of external stresses, remains unexplored. This thesis will address this gap by investigating whether deadlocks are a natural feature of the equilibrium state of ring polymers and, if so, to characterize their behavior. Notably, the definition of what constitutes a "deadlock" is not yet fully clear, and part of this thesis will aim to establish a more precise definition, acknowledging that a deadlock is likely not a binary property.

In steady-state shear flow, polymer melts exhibit characteristic rheological behaviors, which can be categorized into various regimes depending on the shear rate [9, 2]. At low shear rates ($\dot{\gamma} < \tau_{relax}$, where τ_{relax} is the longest relaxation time in equilibrium), the systems viscosity remains constant despite increasing shear rate [2]. In this regime, the chain relaxation compensates the effects of the applied shear forces [10] and the chains conformations are similar to their equilibrium conformations. As the shear rate increases, the system enters the *shear thinning regime*, where the viscosity decreases. This behavior arises because the polymer chains stretch and align in the direction of the applied shear force, reducing entanglement interactions and decreasing viscosity [4]. However, the chains do not permanently align, instead they undergo *tumbling*, a dynamic

rearrangement driven by the competition between shear forces and random fluctuations.

Under certain types of stress, such as in elongational flow and active systems, deadlocked structures have been observed and these deadlocks played a key role in the viscosity thickening. Given that deadlocks influence viscosity in these non-equilibrium conditions, an important question arises: is there a similar relationship between deadlocks and the shear-thinning behavior of the melt? In the first part of this thesis, we will show that deadlocks naturally exist in equilibrium. When the system is subjected to shear flow, the viscosity decreases. This raises further questions: Do deadlocks disappear under shear? If they remain, why don't they influence viscosity in the same way as in elongational flow? These questions will be addressed in the second part of the thesis, where we investigate the behavior of deadlocks under shear flow and their impact on the system's rheological properties.

To address the behavior of deadlocks in both, equilibrated and sheared ring polymer melts, this thesis begins with a detailed explanation of the theoretical models used to simulate ring polymer systems (Section 2.1). This is followed by an introduction into Knot Theory (Section 2.2), which is a central concept of the deadlock detection method. The computational models employed, such as molecular dynamics and corresponding thermostats and integration schemes, are discussed in Section 3.1, followed by a description of the deadlock detection algorithm in Section 3.2. We then present the results of the equilibrium simulation (Section 4), where the deadlock composition, deadlock persistence as well as static and dynamic properties of deadlocks in equilibrium are analyzed. The final chapter (Section 5) focuses on the behavior of deadlocks under steady-state shear forces, where we examine the composition, persistence and static properties of deadlocks for two different shear rates: Wi = 8.8 and Wi=30.0. The conclusion summarizes our findings of deadlocks in equilibrated and sheared ring polymer melts and proposes potential directions for future research.

2. Theory

2.1. Polymer Theory

2.1.1. Coarse-Graining of Macromolecules

When studying polymers, we often employ coarse-graining techniques to reduce the complexity of the system while maintaining physical accuracy. At the most detailed level, a polymer molecule consists of numerous atoms connected through chemical bonds, with each atom exhibiting its own degrees of freedom in terms of position and velocity. For a typical polymer melt containing hundreds or thousands of polymers, with each chain comprising thousands of atoms, an atomistic simulation would require great computational resources—if at all possible.

To address these issues, we can exploit the fractal nature of polymer chains. Polymers exhibit self-similarity across different length scales, meaning that their statistical properties remain invariant under a change of scale. When examining a polymer chain at different magnifications, similar structural patterns are observed. This self-similarity principle allows us to represent segments of the polymer chain as single **beads**, where each bead represents multiple chemical repeating units of the original polymer.

Using coarse-grained models, we can reduce the degrees of freedom in the simulation. This allows for the simulation of larger systems or longer time scales compared to fully atomistic simulations. Coarse-grained models are particularly effective when we focus on universal physical properties, since they allow for an efficient description of large-scale phenomena. However, if one is interested in specific details related to the chemistry or atomistic behavior of the system, the finer atomistic details become important.

The coarse-grained model preserves the essential physics of the system through carefully chosen effective interactions between the beads. These interactions incorporate the averaged effects of all the atomic-scale forces that would be present in a fully detailed simulation. For some universal properties, such as those observed in melt simulations, the explicit choice of coarse-grained interactions may not be as important, due to the screening of interaction potentials. However, for other properties, such as the entanglement length, the choice of potential remains important as it depends on the chain stiffness.

Thus, while the coarse-graining approach provides a simplified representation of the system, its effectiveness still relies on selecting appropriate interaction potentials, particularly when certain detailed properties should be captured.

2.1.2. Interaction Potentials

In our coarse-grained polymer simulation, we employ a combination of three interaction potentials that together capture the essential physics of polymer behavior. The parameters of these potentials can be tuned to represent the chemistry of many typical polymers [11]. These choices have been commonly used in many theoretical and computational studies [11], [12].

Weeks-Chandler-Andersen (WCA) Potential

The WCA potential mimics the excluded volume interactions between beads, preventing them from overlapping. It is a modification of the Lennard-Jones potential that is cut off at its minimum and shifted to zero, making the potential purely repulsive. This potential models the short-range repulsion between polymer segments, whether they are bonded or not. The WCA potential takes the form

$$U_{WCA}(r) = \begin{cases} 4\epsilon \left[\left(\frac{\sigma}{r}\right)^{12} - \left(\frac{\sigma}{r}\right)^{6} \right] + \epsilon, & \mathrm{r} < 2^{1/6}\sigma \\ 0, & \mathrm{r} \geq 2^{1/6}\sigma \end{cases},$$

where σ is the bead diameter and r is the distance between two coarse-grained beads [13]. A visual representation of the Lennard-Jones and WCA potential can be seen in the left and central panel of Figure 2.1, respectively.

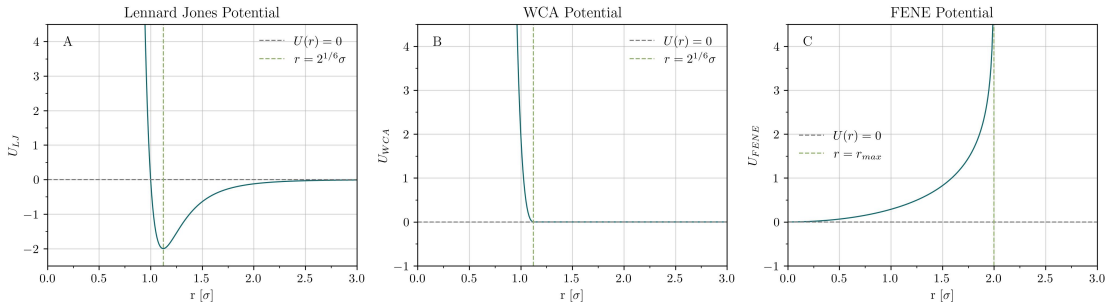

Figure 2.1.: Lennard-Jones Potential, WCA potential and FENE potential. The dashed gray line represents U(r)=0.

Finite Extensible Nonlinear Elastic (FENE) Potential

The FENE potential models the bonds between consecutive beads along the polymer chain. Unlike a simple harmonic spring, the FENE potential includes a finite extension limit, preventing unphysical bond stretching that could occur in a simulation. This characteristic makes it suitable for polymer simulations, as real chemical bonds cannot be stretched indefinitely. The FENE potential takes the form

$$U_{FENE}(r) = -\frac{1}{2} \cdot K \cdot r_{max}^2 \cdot \log\left[1 - \left(\frac{r}{r_{max}}\right)^2\right] ,$$

with spring constant K and maximal stretching length r_{max} [14].
The combination of WCA and FENE potentials for bonded pairs creates a harmonic-like potential with a well-defined minimum, leading to stable bond lengths while preventing bond crossings, provided the values of K, r_{max} and the temperature are chosen appropriately. The non-crossability of chains is especially important for maintaining the correct polymer topology. A sketch of the FENE potential is shown in the right panel of Figure 2.1.

Cosine Angle Potential

The cosine angle potential introduces chain stiffness by adding an energetic penalty for sharp bends between consecutive bonds. This three-body potential depends on the angle formed between three consecutive beads along the chain, θ. The cosine bending potential is expressed as

$$U_{bend} = k_{bend}\left(1 - \cos(\theta - \pi)\right), \tag{2.1}$$

where k_{bend} is the bending stiffness of the polymer.

2.1.3. Polymer Analysis

Having established the framework for the coarse-grained simulation models and the role of interaction potentials, we now introduce a series of theoretical models that quantify the behavior of polymer chains. Understanding the structural and dynamical properties of macromolecules requires a set of analytical tools that describe the polymers spatial configurations and motion.
The Gyration tensor and its eigenvalues offer insight into the shape and compactness of polymer rings, while the mean-squared displacement is a central quantity in understanding the polymers motion and relaxation behavior. Additionally, a theoretical framework is introduced for quantifying the tumbling behavior of ring polymers under shear forces.

Gyration Analysis

The Gyration analysis is a fundamental method for studying the spatial configuration of polymer chains. It is a measure of size and shape of polymers, offering insights into their conformational properties.
At the core of gyration analysis is the gyration tensor, which characterizes the distribution of monomers relative to the polymers center of mass. The gyration tensor S_{mn} describes the second moments of position of a collection of N monomers of a polymer

$$S_{mn} = \frac{1}{N}\sum_{i=1}^{N} r_m^{(i)} r_n^{(i)}, \tag{2.2}$$

where $r_m^{(i)}$ is the m^{th} Cartesian coordinate of the position vector $r^{(i)}$ of particle i relative to the center of mass of the polymer [15]. The monomer's center of mass r_{COM} is given by

$$r_{COM} = \frac{1}{N}\sum_{i=1}^{N} r^{(i)} \tag{2.3}$$

and must be shifted to origin (e.g. $r_{COM} = 0$), in order for equation 2.2 to be applicable. The gyration tensor is a symmetric 3×3 matrix, which can be diagonalized

$$\mathbf{S} = \begin{bmatrix} \lambda_1^2 & 0 & 0 \\ 0 & \lambda_2^2 & 0 \\ 0 & 0 & \lambda_3^2 \end{bmatrix}, \tag{2.4}$$

where the axis are chosen such that the diagonal elements are ordered according to their value, with $\lambda_1^2 \geq \lambda_2^2 \geq \lambda_3^2$. The diagonal elements are the eigenvalues, or *principle moments* of the gyration tensor [16].
The principle moments provide insight into the polymers shape and the extend of the polymer along each principle axes, providing a way to measure the polymers anisotropy. If all three principle moments are roughly equal, the overall shape of the polymer is roughly spherical. If one principle moment is much larger than the others, the polymer is elongated. The relative magnitudes of the principle moments help distinguish between different conformational states, such as coils, ellipsoids or rods.
One of the key quantities derived from the gyration tensor is the radius of gyration R_g, which represents the square root of the mean squared displacement of the monomers from the center of mass of the polymer. It is a measure of the overall size of the polymer and is calculated as the trace of the diagonalized gyration tensor [16]

$$R_g^2 = \mathrm{Tr}(\mathbf{S}) = (\lambda_1^2 + \lambda_2^2 + \lambda_3^2). \tag{2.5}$$

The radius of gyration is commonly used to describe how compact or extended a polymer is in space.

Mean-Squared-Displacement

The dynamics of polymers can be studied by tracking how the polymer's center of mass moves over time. One important tool for analyzing this motion is the mean-squared displacement (MSD) of the polymer's center of mass, often referred to as $g_3(t)$.
The $g_3(t)$ is calculated by following the trajectory of the COM of each polymer as

$$g_3(\Delta t) = \langle \vec{R}_{COM}(t) - \vec{R}_{COM}(t + \Delta t) \rangle^2, \tag{2.6}$$

where $\vec{R}_{COM}(t)$ is the position of the center of mass of the polymer at time t, and $\vec{R}_{COM}(t + \Delta t)$ is the position of the center of mass at a later time $t + \Delta t$. The angle brackets $\langle \cdot \rangle$ represent an ensemble average [17]. To improve the statistic, time-averaging over equilibrium or steady-state periods can be applied.

Typically in ring polymer melts, the MSD exhibits different scaling behaviors depending on the time regime. Initially, during the early stages of the polymer's motion, the MSD grows sublinearly due to the constrained movement of the polymer in the melt:

$$g_3(\Delta t) \sim \Delta t^{\alpha} \qquad \text{with} \quad \alpha < 1 \quad \text{for} \quad \Delta t < \tau_{\text{relax}}, \tag{2.7}$$

where τ_{relax} is the time scale for the polymer to reach an uncorrelated conformation. This behavior typically applies for times shorter than the relaxation time τ_{relax}, after which the polymer's motion becomes diffusive. For a system of nonconcatenated ring polymers in a melt, α has been found to be approximately $\frac{3}{4}$ [17]. This sublinear growth eventually transitions into a diffusive regime, where $g_3(\Delta t)$ grows linearly with time, indicative of normal diffusion:

$$g_3(\Delta t) = 6D\Delta t \quad \text{for diffusion}, \tag{2.8}$$

where D is the diffusion constant. The scaling of $g_3(\Delta t)$ thus provides a way to assess whether the system has entered a diffusive regime.

Tumbling

Polymers in shear flow exhibit a dynamic phenomenon known as *tumbling*, which refers to the aperiodic collapse and reorientation of the polymer as it interacts with shear forces. This motion occurs due to the competition between the polymer aligning with the flow direction and random fluctuations. As a result, the polymer repeatedly elongates, collapses, and reorients, leading to cyclical but aperiodic tumbling behavior.
Tumbling can be detected by studying the time-dependent fluctuations of the polymer's shape, which can be described by its gyration tensor S_{mn}. The gyration tensor provides information about the polymer's extension along different spatial directions, with S_{xx} and S_{yy} representing the extensions along the x and y directions, respectively. In shear simulations, the x-direction typically represents the flow direction, where the polymer aligns with the shear flows, while the y-direction corresponds to the gradient flow direction, perpendicular to the flow. As a consequence of the shear forces, the polymer elongates in the flow direction, resulting in a large S_{xx} and a small S_{yy}. During tumbling, this elongation in S_{xx} collapses, while S_{yy} increases. Subsequently, the polymer reorientates, characterized by a rapid increase in S_{xx} and a decrease in S_{yy}. Since the fluctuations in shape along the x- and y-axes become significant during tumbling, these fluctuations can be used to track and characterize tumbling events. By analyzing the cross-correlation function $C_{xy}(\tau, \dot{\gamma})$, which captures the correlation between fluctuations in S_{xx} and S_{yy} over a time delay τ, we can identify the characteristic oscillations associated with tumbling events. This correlation function is given by:

$$C_{xy}(\tau, \dot{\gamma}) = \frac{\langle \delta S_{xx}(t, \dot{\gamma}) \delta S_{yy}(t + \tau, \dot{\gamma}) \rangle_t}{\sigma_{xx}(\dot{\gamma}) \sigma_{yy}(\dot{\gamma})} \tag{2.9}$$

where $\delta S_{\alpha\alpha}(t, \dot{\gamma}) = S_{\alpha\alpha}(t, \dot{\gamma}) - \langle S_{\alpha\alpha}(\dot{\gamma}) \rangle$ represents the fluctuation around the mean, and $\sigma_{\alpha\alpha}(\dot{\gamma})$ is the standard deviation of $S_{\alpha\alpha}$ [18]. When tumbling occurs, the cross-

correlation function exhibits damped oscillations, with a pronounced maximum followed by a minimum, revealing the reorientation dynamics of the polymer under shear.
A key feature of this analysis is the *tumbling frequency* $f_{\mathrm{tb}}(\dot{\gamma})$, which describes how frequently a polymer completes a tumbling cycle at a given shear rate $\dot{\gamma}$. The oscillation period $\tau_{\mathrm{tb}}(\dot{\gamma})$ of the correlation function can be extracted from the times $t^{-}(\dot{\gamma})$ (the time of the maximum peak) and $t^{+}(\dot{\gamma})$ (the time of the minimum peak) as

$$\tau_{\mathrm{tb}}(\dot{\gamma}) = 2\left(t^{-}(\dot{\gamma}) - t^{+}(\dot{\gamma})\right). \tag{2.10}$$

The tumbling frequency is then given by

$$f_{\mathrm{tb}}(\dot{\gamma}) = \frac{1}{\tau_{\mathrm{tb}}(\dot{\gamma})}, \tag{2.11}$$

which provides insight into the timescale of polymer reorientation, offering a measure of how the polymer responds to the shear forces.

2.2. Knot Theory

This thesis aims to understand the entanglement and topological interactions that occur between ring polymer chains in a melt. Ring polymers possess the ability to thread through one another multiple times, leading to intrinsic entanglements called deadlocks or supramolecular chains. Individual chains become increasingly constrained by threadings with neighboring chains, ultimately acting as topological obstacles to one another.
The conformational diversity of long ring polymers presents an important challenge for this research: how can we reliably distinguish between a freely moving polymer chain and one constrained by topological interactions with its neighbors? Methods of visual inspection often fall short when confronted with the numerous embeddings of these entanglements. Knot theory, a mathematical branch of topology, provides tools that can be adapted to address this challenge. While knot theory traditionally focuses on classifying single closed curves in space – a scenario different from our multi-chain polymer systems – its mathematical framework offers concepts that we can apply to our specific research problem. Of particular importance are knot invariants – quantities that remain unchanged regardless of how a topological structure is embedded in three-dimensional space. While no single invariant can distinguish between all knot types, certain invariants, such as the Alexander Polynomial, have proven particularly effective for identifying topological differences between structures.
The Alexander Polynomial, which will be central to our analysis, offers a systematic approach to identify the knot type of a closed-loop-structure. This mathematical tool allows us to develop algorithmic criteria for identifying deadlocked states. The practical implementation of this concept, including how we adapt knot theory concepts to our specific multi-chain system, will be detailed in Chapter 3.2. To understand these adaptations, we first need to introduce some fundamental concepts of knot theory.

2.2.1. Introduction to Knot Theory

In mathematical terms, a knot is defined as "an embedding of a circle $\mathbb{S}^1$ into three-dimensional Euclidean space $\mathbb{R}^3$" [19]. This formal definition differs from everyday knots, as mathematical knots are closed curves without endpoints; they are considered infinitely thin, and the curve must not pass through itself [20].
Three-dimensional knots are often studied through their two-dimensional representations, called *knot diagrams*. These diagrams project the knot onto a plane while indicating over- and under-crossings through a simple visual convention: at each crossing, a small break in the lower strand shows where one part of the knot passes beneath another. By indicating the over- and under-crossings, all essential topological information of the original three-dimensional structure is preserved. Examples of knot diagrams are shown in Figure 2.2.

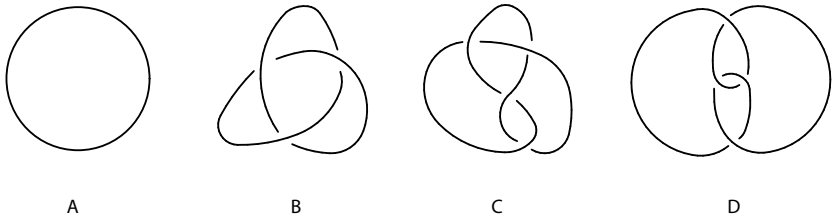

Figure 2.2.: Knot diagrams of different knots. A) Knot diagram of the unknot, B) Knot diagram of the Trefoil, C) Knot diagram of the Figure-8-Knot, D) Knot diagram of a different embedding of the Figure-8-Knot.

One of the fundamental questions in knot theory is determining whether two knots should be considered the same. Two knots are mathematically equivalent if one can be smoothly deformed into the other without cutting the knot or allowing it to pass through itself [20]. These transformations, known as ambient isotopies, preserve the topological properties of the knot while allowing for geometric changes [19].
The challenge of determining knot equivalence lies in the infinite variety of possible representations of the same knot. A single knot can be twisted, stretched, or distorted in countless ways while maintaining its fundamental topological structure [20]. Two different embeddings of the same topological structure, the Figure-8-Knot, are shown in panel C and D of Figure 2.2.

2.2.2. Topological invariants - The Alexander Polynomial

To address the challenge of knot equivalence, mathematicians have developed topological invariants—quantities that remain unchanged under ambient isotopy. These invariants serve as *fingerprints* of knots, providing a way to distinguish between different knot types regardless of their specific geometric representation [21].
The Alexander Polynomial $\Delta_K(t)$ is one of most powerful and computationally accessible topological invariants. It provides a tool for distinguishing between knot types and is particularly effective for knots with a low crossing number [19]. It is important to note, however, that while the Alexander Polynomial is effective in distinguishing between many knot types, it cannot distinguish a knot from its mirror image or chiral enantiomer - a knot type formed by changing the sign of all crossings in the knot diagram, see Figure 2.4 [19]. Another limitation is that while the Alexander Polynomial is able to distinguish between many knot types, there are some knot types that share the same Alexander Polynomial, meaning that the invariant does not uniquely identify every knot type.

Calculation of the Alexander Polynomial

The process of computing the Alexander Polynomial starts with a knot diagram of a knot K and follows a series of steps, where the knot diagram is mapped onto a matrix $\mathbf{M}(t; K)$ and the determinant of a minor of this matrix gives rise to the Alexander Polynomial [22]. To summarize the process, we now outline the key steps to compute the Alexander Polynomial, without delving into the underlying derivations, which would require more extensive treatment than this thesis allows.

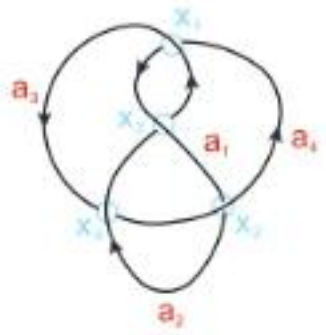

Figure 2.3.: Labeled Knot Diagram of the Figure-8-Knot.

- **Orientation :** First, we assign an arbitrary orientation to the knot diagram. This orientation is usually indicated by arrows along the curve, which define the direction in which we will translate the diagram.
- **Label Under-Crossings :** Next, we label the n crossings in the knot diagram with variables $x_1, x_2, ..., x_n$. Starting from an arbitrary under-crossing (which we call x_1), we follow the orientation of the knot diagram and assign an increasing index to all

the under-crossings in the diagram until all n crossings are labeled. Under-crossings refer to the crossings where the current segment passes below another segment.

- **Label Arcs :** Arcs are defined as the strands that connect consecutive under-crossings. Starting from the crossing x_1 and following the orientation of the knot diagram, we assign an increasing index to all n arcs $(a_1, a_2, ..., a_n)$. Arc a_i connects under-crossings x_i and x_{i+1}, with periodic boundary conditions (i.e. a_n connects x_n back to x_1).
- **Crossing Sign :** Next, we identify whether a crossing in the knot diagram is a positive or negative crossing (as illustrated in Fig 2.4). Moving on the over-crossing arc along the orientation of the knot diagram, we identify whether the under-crossing arc enters the crossing from the right (positive crossing) or from the left (negative crossing).

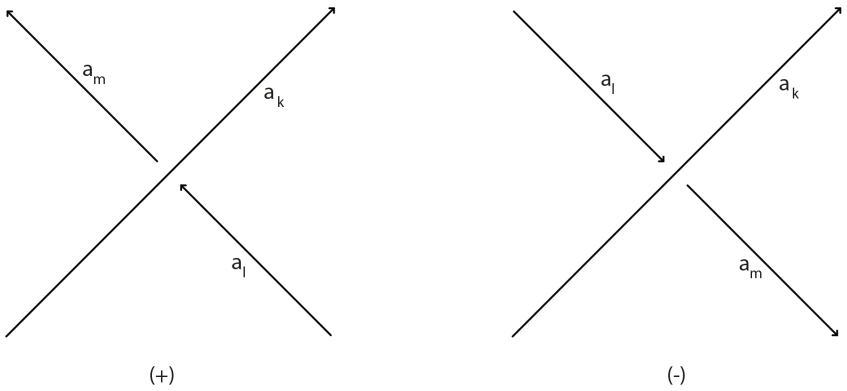

Figure 2.4.: Crossing sign convention. a_k labels the over-crossing arc, a_l the incoming under-crossing arc and a_m the outgoing under-crossing arc.

- **Matrix Construction :** Then, we construct an $n \times n$ matrix $\mathbf{M}(t; K)$, where the rows correspond to the crossings and the columns correspond to the arcs. For each crossing x_i, there are three arcs associated with it: the over-crossing arc a_k, the incoming under-crossing arc a_l and the outgoing under-crossing arc a_m. The matrix $\mathbf{M}(t; K)$ is then filled with specific expressions for each crossing based on its sign, where arcs not involved in this crossing are set to 0:
  - For **positive** crossings, the values are:
    - $a_k = 1 - t$
    - $a_l = -1$
    - $a_m = t$

  - For **negative** crossings, the values are:
    * $a_k = 1 - t$
    * $a_l = t$
    * $a_m = -1$

- **Minor Calculation and Alexander Polynomial :** After constructing the Matrix $\mathbf{M}(t; K)$, we select any minor of order $(n-1) \times (n-1)$ and calculate its determinant. This yields the Alexander Polynomial $\Delta_K(t)$.

To illustrate the calculation of the Alexander Polynomial, we show an example of the Figure-8-Knot, whose knot diagram is shown in Figure 2.3.

$$\begin{array}{c} \\ a_1 \\ a_2 \\ a_3 \\ a_4 \end{array} \begin{array}{c} \begin{array}{cccc} x_1^{(+)} & x_2^{(-)} & x_3^{(+)} & x_4^{(-)} \end{array} \\ \begin{pmatrix} t & t & 1-t & 0 \\ 0 & -1 & -1 & 1-t \\ 1-t & 0 & t & t \\ -1 & 1-t & 0 & -1 \end{pmatrix} \end{array} \Longrightarrow \begin{vmatrix} t & t & 1-t \\ 0 & -1 & -1 \\ 1-t & 0 & t \end{vmatrix} \Longrightarrow t^2 - 3t + 1$$

3. Methods

3.1. Simulation Methods

This chapter presents the fundamental methodologies employed in our molecular dynamics studies, focusing on techniques needed to conduct equilibrium and non-equilibrium molecular dynamics simulations.
We begin by discussing the use of reduced units, followed by an introduction into the Velocity-Verlet Algorithm, our chosen numerical integrator to solve the equations of motion. To control temperature in our simulations, we employ two distinct thermostating approaches: the deterministic Nosé-Hoover thermostat and the stochastic Langevin thermostat. The latter part of the chapter focuses on non-equilibrium molecular dynamics methods for simulating steady-state shear flows, namely the Müller-Plathe and the SLLOD method.

3.1.1. Reduced Units

In molecular dynamics simulations, physical constants and parameters often span several orders of magnitude. For instance, the thermal energy at room temperature in SI units is approximately 10^{-21} J, while the typical monomer diameter ranges from 10^{-10}m to 10^{-8}m. If these numerical values are used directly in the equations of motion, it can lead to numerical instabilities and errors. To avoid this, a common approach is to use reduced units [23]. These units scale all relevant physical parameters and constants to dimensionless quantities that are approximately of the same order, typically near unity. A typical set of reduced units involves rescaling the **thermal energy** (k_BT), the **mass** of the monomers (m_m) and the **monomer diameter** (σ) to unity. This rescaling is done by dividing each physical quantity by a reference value, which normalized all values and produces dimensionless numbers. The conversion of all relevant physical parameters to their reduced forms is summarized in Table 3.1.

Physical Parameter	Parameter Abbreviation	Reduced Form
thermal energy	k_BT	$k_BT^* = k_BT \ / \ \epsilon$
mass	m	$m^* = m \ / \ m_m$
distance	d	$d^* = d \ / \ \sigma$
time	t	$t^* = \sqrt{\frac{m^*}{k_BT^*}} d^*$
viscosity	η	$\eta^* = \eta \cdot \frac{d^{*2}}{\sqrt{m^* \cdot k_BT^*}}$

Table 3.1.: Reduced Units : Conversion Table.

In this framework, the thermal energy is normalized by the characteristic energy scale, ϵ, the mass is divided by the monomer mass m_m and the distance is scaled by the monomer diameter σ. Additionally, other important quantities such as time and viscosity are derived from the chosen reduced units. For example the reduced time scale (t^*) and the reduced viscosity (η^*) are functions of the reduced mass, thermal energy and distance.

3.1.2. Velocity-Verlet Algorithm

Our system is described using a classical framework where the time evolution of a particle is governed by Newton's second law

$$\vec{F_i} = m_i \cdot \frac{d^2\vec{r_i}}{dt^2} \ ,$$

with $\vec{F_i}$ representing the force on particle i, m_i its mass and the second derivative of the position $\frac{d^2\vec{r_i}}{dt^2}$ its acceleration. However, when simulating many-body systems, the equations of motion can no longer be solved analytically. Instead, we rely on numerical approximations to propagate the system in time.
One such approximation scheme involves discretizing time into small intervals δt and applying finite-difference methods to integrate the equations of motion step by step. In this context, the Velocity-Verlet algorithm [24] offers a way to update the position ($\vec{r_i}$) and velocity ($\vec{v_i}$) of particle i at each time-step δt:

$$\vec{r_i}(t+\delta t) = \vec{r_i}(t) + \vec{v_i}(t) \cdot \delta t + \frac{\vec{F_i}(t)}{2m_i} \cdot \delta t^2 + \mathcal{O}(\delta t^4), \tag{3.1}$$

$$\vec{v_i}(t+\delta t) = \vec{v_i}(t) + \frac{\vec{F_i}(t) + \vec{F_i}(t+\delta t)}{2m_i} \cdot \delta t + \mathcal{O}(\delta t^3), \tag{3.2}$$

where $\vec{r_i}(t+\delta t)$ and $\vec{v}_i(t+\delta t)$ are the position and velocity of particle i at time $t+\delta t$. The total force acting on particle i is obtained by taking the derivative of the total potential energy $U_{tot}(\vec{r}_j(t+\delta t))$

$$\vec{F}_i(t+\delta t) = -\vec{\nabla}_{\vec{r_i}} U_{tot}(\vec{r_j}(t+\delta t)). \tag{3.3}$$

The Velocity-Verlet algorithm possesses several advantages that make it particularly well-suited for molecular dynamics simulations. It preserves the symplectic structure of Hamilton's equations, ensuring long-term energy conservation. This energy conservation property means the algorithm naturally simulates the microcanonical (NVE) ensemble, where the number of particles, volume, and total energy remain constant. Additionally, the algorithm is time-reversible (up to numerical precision) and it conserves the phase-space volume in accordance with Liouville's theorem, which is crucial for maintaining the statistical properties of the ensemble. Unlike some other integration schemes, such as the Euler algorithm, the Velocity-Verlet algorithm is self-starting, requiring only initial positions and velocities, and does not suffer from the energy drift associated with the Euler algorithm.

3.1.3. Thermostats

Molecular dynamics simulations typically involve solving the equations of motion for a molecular system, which inherently corresponds to the microcanonical ensemble (NVE ensemble). However, it is often necessary to sample configurations from a canonical ensemble, where the temperature is held constant (NVT ensemble). This is achieved by modifying the simulation through the use of thermostat algorithms, which regulate the system's temperature over time [25].

Nosé-Hoover Thermostat

The Nosé-Hoover thermostat provides a deterministic approach to simulate the canonical (NVT) ensemble by extending the system's Hamiltonian with an additional degree of freedom, $\zeta(t)$, that acts as a thermal reservoir. This variable modulates the system's temperature by rescaling the velocities of the particles, either slowing them down or speeding them up, to ensure that the system's temperature matches the target value [26]. The temperature is computed from the system's kinetic energy, which is related by the equipartition theorem

$$\frac{3N}{2} k_B T = \sum_i \frac{1}{2} m_i \vec{v_i}^2 \tag{3.4}$$

where k_B is the Boltzmann constant, T the temperature, N the number of particles in the simulations and $\vec{v_i}$ is the velocity of particle i. The variable $\zeta(t)$ is used to modify the equations of motion, ensuring that the system samples a canonical ensemble by enforcing

temperature regulation while allowing the system's dynamics to remain deterministic and continuous. The modified equations of motion are given by equations 3.5 and 3.6.

$$\frac{d\vec{p_i}}{dt} = \vec{F_i} - \zeta(t)\vec{p_i} \tag{3.5}$$

$$\frac{d\zeta(t)}{dt} = \frac{1}{Q}\left(\sum_{i=1}^{N}\frac{1}{2}m_i v_i^2 - 3Nk_BT\right) \tag{3.6}$$

Here, Q controls the relaxation time of the thermostat and T is the target temperature. In this study, Q is set to 1.0, which is a typical value for many systems, though it can vary depending on the system's dynamics and the desired accuracy of temperature regulation. Note that the system *tends* towards the target temperature, rather than maintaining it exactly at every instant, with a characteristic time scale of approximately Q^{-1} for reaching thermal equilibrium.

Langevin Thermostat

An alternative approach to simulating the canonical ensemble is the Langevin thermostat, which mimics the interaction of the system with a heat bath through the addition of random forces and friction. The Langevin equation of motion for particle i is given by: [27]

$$m_i\frac{d^2\vec{r_i}}{dt^2} = \vec{F_i} - \gamma\vec{v_i} + \sqrt{2\gamma k_BT}\,\vec{\xi}_i(t), \tag{3.7}$$

where γ is the friction coefficient, which, in reduced time units, is set to 1.0 in this study. This value is commonly used in Langevin dynamics simulations. $\vec{\xi}_i(t)$ represents Gaussian white noise with the properties:

$$\langle\vec{\xi_i}(t)\rangle = 0, \quad \langle\vec{\xi_i}(t)\vec{\xi_i}(t')\rangle = \delta_{ij}\delta(t-t') \tag{3.8}$$

The noise term ensures that the system satisfies the fluctuation-dissipation theorem, which means that the source of the random forces is the same as the source of the friction (i.e., both involve the same friction coefficient, γ). The combination of equations 3.7 and 3.8 guarantees that the fluctuation-dissipation theorem holds. While the friction in the Langevin equation corresponds to the damping due to the thermostat, there is an additional friction arising from the interactions between particles, which is typically much higher than the value of γ used in this context.
The Langevin dynamics can be integrated using a modified Velocity-Verlet scheme. The velocity update at the midpoint of the time step is given by equation 3.9, the position update equation by equation 3.10 and finally the velocity update equation at the end of the time step is given by equation 3.11.

$$\vec{v_i}(t+\frac{\delta t}{2}) = \vec{v_i}(t) - \frac{\delta t}{2}\left(\frac{\vec{F_i}(t)}{m_i} + \gamma\vec{v_i}(t)\right) + \sqrt{\frac{\delta t}{2}}\,\vec{\xi_i}(t) \tag{3.9}$$

$$\vec{r_i}(t+\delta t) = \vec{r_i}(t) + \vec{v_i}(t+\frac{\delta t}{2})\delta t \tag{3.10}$$

$$\vec{v_i}(t+\delta t) = \vec{v_i}(t+\frac{\delta t}{2}) - \frac{\delta t}{2}\left(\frac{\vec{F_i}(t+\delta t)}{m_i} + \gamma\vec{v_i}(t+\delta t)\right) \tag{3.11}$$

These modifications to the Velocity-Verlet scheme ensure the system is governed by Langevin dynamics, balancing the effects of friction and random noise to regulate temperature.

3.1.4. Müller-Plathe Method

The Müller-Plathe (MP) method provides an efficient approach to calculate the shear viscosity η of a material through non-equilibrium molecular dynamics simulations (NEMD). While traditional experimental methods apply a velocity gradient to induce momentum flux, the MP method reverses this cause-and-effect relation: it imposes a momentum flux that generates a velocity gradient, from which the shear viscosity can be determined.
To implement the Müller-Plathe method, the simulation box is divided into N even slabs, with $M = N/2 + 1$ denoting the central slab. In slabs 1 and M, the particles with the largest negative and positive x-components of momentum are identified, respectively. The x-components of momentum between these two particles are exchanged, effectively transferring momentum between the slabs. It is crucial that the two particles have the same mass, ensuring that both the total linear momentum and the total energy of the system are conserved. This momentum exchange is repeated periodically, generating a momentum flux along the z-direction [28].
The total momentum transferred, P_{tot}, is given by the sum of momentum exchanges across the slabs

$$P_{tot} = \sum_i \left(p_{x,M} - p_{x,1}\right), \tag{3.12}$$

where $p_{x,1}$ and $p_{x,M}$ are the x-components of momentum in slabs 1 and M, respectively. The momentum flux $j_z(p_x)$ is defined as the x-component of the momentum that flows through a surface perpendicular to the z-direction during a time t

$$j_z(p_x) = \frac{P_{tot}}{2tL_xL_y}, \tag{3.13}$$

where L_x and L_y are the lengths of the simulation box in the x- and y-directions, respectively. This process generates a linear velocity profile across the system.
Once the system reaches a steady state, the velocity gradient $\frac{\partial v_x}{\partial z}$ is measured. Using linear response theory, the shear viscosity is then determined from the relationship between the momentum flux and the velocity gradient:

$$j_z(p_x) = -\eta \frac{\partial v_x}{\partial z}. \tag{3.14}$$

3.1.5. SLLOD Method

The SLLOD method is a nonequilibrium molecular dynamics (NEMD) simulation method to generate planar Couette flow in molecular systems. The SLLOD algorithm introduces a modified set of equations of motion that incorporates the effects of shear flow directly into the simulation. These equations ensure that particle dynamics include contributions from both, thermal motion and the imposed flow field. In doing so, the SLLOD method maintains a consistent coupling between the particle velocities and the macroscopic flow gradient. Thermostats are applied to control the system temperature, ensuring energy dissipation matches the heat generated by viscous forces.
The *atomic* SLLOD algorithm modifies the equations of motion by a streaming term, applied at the position of each monomer in a molecule

$$\dot{\vec{r}}_{i\alpha} = \frac{\vec{p}_{i\alpha}}{m_{i\alpha}} + \vec{r}_{i\alpha} \cdot \nabla \vec{v} \tag{3.15}$$

$$\dot{\vec{p}}_{i\alpha} = \vec{F}_{i\alpha} - \vec{p}_{i\alpha} \cdot \nabla \vec{v}, \tag{3.16}$$

where $m_{i\alpha}$ is the mass of monomer α of molecule i, $\vec{v}$ is the shear velocity field and the force $\vec{F}_{i\alpha}$ includes all intermolecular forces.
The atomic form of the SLLOD equations is not directly applicable to molecular fluids (e.g. polymer melts), due to their internal degrees of freedom. Applying the streaming velocity to all atomic sites within a molecule ignores contributions from molecular rotation and deformation [29]. Consequently, internal motions are inaccurately coupled to the shear flow, leading to artifacts such as enhanced orientational ordering and molecular rotations. This bias can be corrected by evaluating the streaming velocity at the position of the center of mass of the molecule, rather then at the position of each atom in the molecule:

$$\dot{\vec{r}}_{i\alpha} = \frac{\vec{p}_{i,\alpha}}{m_{i\alpha}} + \vec{r}_i \cdot \nabla \vec{v} \tag{3.17}$$

$$\dot{\vec{p}}_{i\alpha} = \vec{F}_{i,\alpha} - \left(\frac{m_{i\alpha}}{m_i} \right) \vec{p}_i \cdot \nabla \vec{v}. \tag{3.18}$$

The modifications for the *molecular* SLLOD equations of motion were shown to produce identical averages in the steady state compared to the *atomic* SLLOD equations of motion, even though the response of the system is different [29].
In both cases, molecular and atomic SLLOD, periodic boundary conditions are used to mimic a bulk system by ensuring that particles experience continuous, unbroken interactions across the simulation box boundaries.
As particles move between layers in the simulation box, they dissipate part of the shear velocity. If the shear were not maintained externally, the shear velocity would eventually

dissipate completely, leading to zero shear velocity and a higher effective temperature in the system. However, with the SLLOD method, the shear profile *is* maintained externally, enforcing the shear profile onto the system. As energy is dissipated, the system experiences a rise in temperature due to *viscous heating*. To maintain a thermodynamic steady state and remove excess heat, a Nosé-Hoover thermostat is applied to the system. In the case of molecular SLLOD, the molecular center of mass kinetic temperature is thermostated, rather than each monomer individually [29].
For the SLLOD method, the viscosity (η) of the atomistic/molecular fluid is calculated based on the shear strain rate ($\dot{\gamma}$) through the equation

$$\eta(\dot{\gamma}) = -\frac{\sigma_{xy}}{\dot{\gamma}}, \tag{3.19}$$

where σ_{xy} represents an off-diagonal component of the stress tensor, where the index x is the flow direction and the index y indicates the normal direction to the flow [29]. The per-atom stress tensor σ_{ij} is a second-rank tensor that completely characterizes the internal forces acting within a fluid. Mathematically, the per-atom stress tensor is expressed as the sum of kinetic and potential contributions

$$\sigma_{jk} = -mv_j v_k - W_{jk}(\vec{r}^N), \tag{3.20}$$

where m is the mass of the particle, v the velocity and $W_{ij} = \vec{r_i} \cdot \vec{F_j}$ is the virial contribution from intra and intermolecular interactions. The indices j and k take values x, y, z to generate the components of the per-atom stress tensor [30].
Physically, each component σ_{jk} of the stress tensor represents the force per unit area acting on a surface element. Specifically, the first index (j) indicates the direction of the force, while the second index (k) specifies the orientation of the surface normal vector on which the force acts. The diagonal elements (σ_{xx}, σ_{yy}, σ_{zz}) represent normal stresses, acting perpendicular to the surface, while the off-diagonal elements (σ_{xy}, σ_{xz}, σ_{yz}) represent shear stresses, acting parallel to the surface. In the context of planar Couette flow, the shear viscosity is primarily determined by the σ_{xy} component, which characterizes the momentum transfer in the flow direction (x) across planes normal to the velocity gradient direction (y).

3.2. Deadlock Detection algorithm

Two rings in close proximity can become tangled and restrict each others movement, thus, acting as a constraint on each other - called a deadlock. Detecting the deadlock can become quite difficult, as mathematical knots are only defined on closed curves (see section 2.2), where non-catenated and unknotted rings are by definition unknots. However, with a proper cutting and reconnection method, two rings can be cut open and the four dangling ends can be reconnected. This generates a super-ring structure, which is potentially knotted in a mathematical sense. Calculating the Alexander polynomial (see section 2.2.2) reveals the knotted or unknotted state of the super-ring. We consider a

pair of rings deadlocked, if the super-ring topology is knotted, and not deadlocked, when the super-ring reveals the unknot.
The algorithm for detecting deadlocked or disentangled structures was introduced in a previous study [8]. The researchers validated their method by comparing two approaches: first, by cutting the polymer pair open at their most distant monomer positions, interconnecting the ends and evaluating the knotted/unknotted state of the super-ring, and second, by physically pulling the two polymers apart. Importantly, they found that these two methods were equivalent in revealing the deadlocked/non-deadlocked state of the polymer pair.

3.2.1. Preselection : Linear Separability

Prior to the deadlock detection method, the deadlocked/non-deadlocked state of a polymer pair is unknown. This implies, that in general all $M \cdot (M-1)$ ring pairs have to be evaluated, where M is the number of rings in the simulation box. As the calculation of the Alexander polynomial scales with the number of monomers squared N^2, the computation is very inefficient. The linear separability check aims to efficiently preselect polymer pairs that cannot be deadlocked, thus excluding them form the costly Alexander polynomial calculation. Two polymers are deemed linearly separable if there exists a separating plane that divides the two polymers such that their monomers do not overlap when projected onto the surface normal. This preselection finds suitable planes that (potentially) separate two polymers in space. Subsequently, the monomer positions are projected onto one-dimensional space, defined by the surface normal vector, from which the linear separability can be obtained. The linear separability is calculated for all $M \cdot (M-1)$ polymer pairs. The procedure for evaluating the linear separability of polymer i and polymer j consists of the following steps:

- **Convex Hulls** : Convex hulls are computed around polymer i and polymer j, respectively. These hulls represent the minimal bounding shapes for each polymer in space, where the surface is constructed by triangles formed between sets of three vertices of the convex hull. The vertices of the convex hull corresponds to monomer positions that are located at the surface of the convex hull.

- **Closest Vertices** : The closest pair of vertices between the two hulls, q_i and q_j, are identified, where q_i is a vertex monomer of polymer i and q_j a vertex monomer of polymer j.

- **Surface Identification** : Once the closest pair of vertex monomers (q_i, q_j) is identified, the next step involves finding the three nearest vertex monomers on polymer i to the vertex monomer q_j, as well as the three nearest vertex monomers of polymer j to vertex monomer q_i. We are now left with six vertices, three on polymer i and three on polymer j. We identify all triangular surfaces of the convex hull, where at least one vertex of this surface corresponds to one of the six identified vertices. In Figure 3.1, the process is outlined on a two-dimensional example, where

panel B shows the six identified vertices and panel C highlights all (potentially) dividing surfaces.

- **Normal Vectors and Projections** : The normal vectors of the identified surfaces are calculated, and the monomers of both polymers are projected onto the axis defined by each normal vector. A polymer pair is considered linearly separable if, along any of these projection axis, the monomers of polymer i are completely separable from those of polymer j. This means that there exists an axis where all monomers of polymer i are either on the left or right of the monomers of polymer j.
- **Decision** : If any of the projections results in linear separability, the polymer pair is excluded from the full deadlock detection process as the pair cannot be deadlocked. If no such projection is found, the polymer pair is flagged as potentially deadlocked and is subjected to the full deadlock detection algorithm.

By applying the linear separability check, the computational costs of checking all polymer pairs is greatly reduced, as only the potentially deadlocked pairs are further analyzed.

3.2.2. Reconnection Method

Once the potentially deadlocked pairs are identified via the linear separability preselection, the next step in the deadlock detection algorithm is constructing a super-ring structure by reconnecting two (potentially deadlocked) polymer rings [8]. The primary goal of this method is to open both polymer rings by removing one monomer from each polymer and subsequently interconnecting the four dangling ends to form a single closed loop structure. We then evaluate the resulting super-ring for its knotted state using the Alexander polynomial. If the super-ring is knotted, the polymer pair is considered deadlocked; otherwise, it is not.
By removing one monomer on each polymer, we create four openings, two on one chain and two on the other chain. In general, there are two different ways to interconnect the four ends. However, both reconnection approaches will result in a knotted state, if the original pair was deadlocked and an unknotted state, if the original pair was disentangled. Note, that different reconnections can result in different knot types and the complexity of the knot type does not correlate with the complexity of the deadlock. Hence, we only distinguish between knotted and unknotted structures and don't consider different knot types.
A key challenge in the reconnection process is to ensure that the artificially created paths do not introduce any new topological features, such as creating or disentangling a knot. This is ensured, if the newly created arcs do not pierce through the polymer (itself or its neighbor) and the arcs do not intersect. Satisfying these two criteria, we came up with a suitable reconnection procedure:

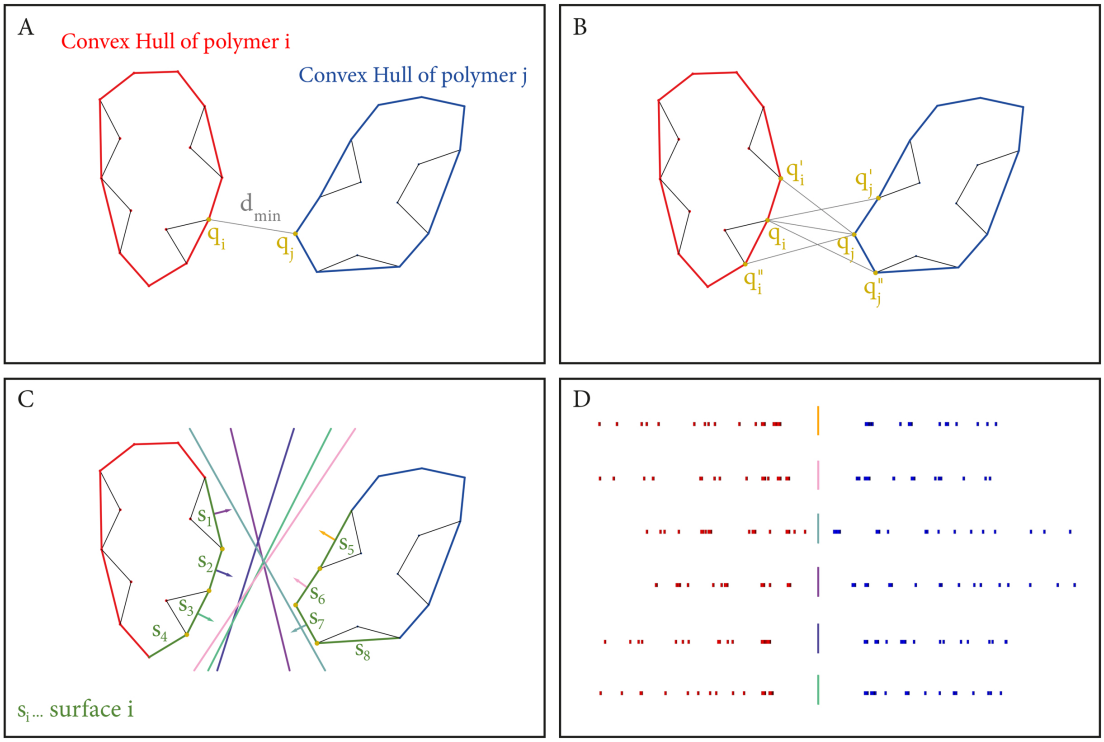

Figure 3.1.: Schematic illustration of the linear separability preselection process shown in 2D for clarity. A) Two polymers with their respective convex hulls (red for polymer i, blue for polymer j) and the identification of their closest vertices (q_i, q_j) with minimum distance d_{min}. B) The three nearest neighboring vertices (q_i', q_i'' and q_j', q_j'') to the closest vertex pair are identified on each polymer. C) Potential separating surfaces (S_1 through S_8) derived from the convex hull edges containing at least one of the six key vertices. D) Projections of all monomer positions onto the normal vectors of the identified surfaces, with red and blue dots representing the projected positions of polymers i and j, respectively. The polymers are linearly separable if their projections do not overlap along at least one of these directions.

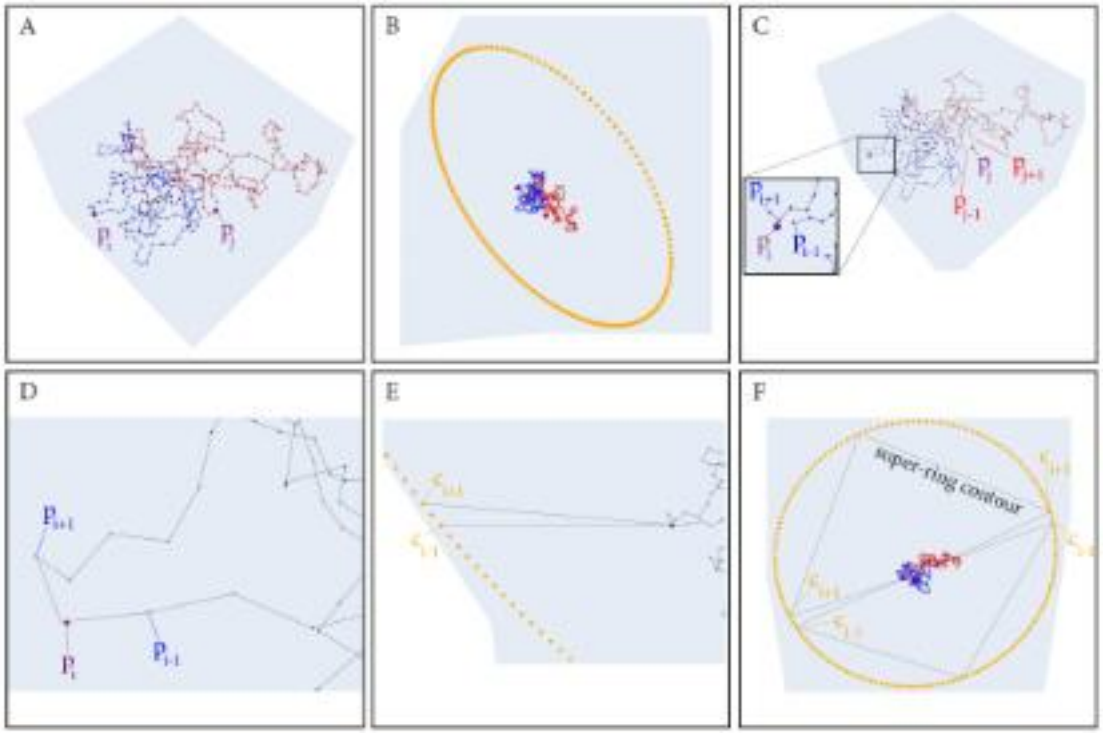

Figure 3.2.: Topological reconnection procedure for ring polymer pairs. (A) Initial configuration of two ring polymers (blue and red) with cut monomers (p_i, p_j) highlighted in purple. (B) Construction of a reference circle (yellow dots) with radius $R = 2d_{max}$ surrounding both polymers. (C) Detailed view of monomer positions after removing cut monomers, with inset showing dangling ends (p_{i-1}, p_{i+1}) near the cut point p_i. (D) Close-up view demonstrating the connection of dangling ends to a small displacement from the original cut point p_i. (E) Extension of polymer termini toward their designated circle points (c_{i-1}, c_{i+1}). (F) Completed super-ring structure showing the final contour with connections through circle points.

- **Choosing the Cutting Points** : The first step is to select a suitable cutting point on each polymer. These cutting points must necessarily be surface monomers, as bulk monomers would create arcs that can easily intersect with the polymer, potentially altering its topology. We create a single convex hull around the polymer pair and identify all vertices of this common convex hull. These vertices correspond to potential cutting points, as they provide a direct path outwards for reconnection. From this set of suitable cutting points, we select one cut monomer p_i on polymer i and one cut monomer p_j on polymer j (Figure 3.2, Panel A).
- **Creating a Circle of Scatter Points around the Polymer Pair** : We create an artificial circle with a radius $R = 2 \cdot d_{max}$ (where d_{max} is the largest distance

between any two monomers of the ring pair) around the polymers. The circle must be positioned so that both cut monomers have a direct path to the circle. To approximate the circle, we chose 200 scatter points (Figure 3.2, Panel B). We identify the points closest to the cut monomers and label them c_i and c_j for the circle points closest to p_i and p_j, respectively.

- **Connection to the Cut Monomer** : The monomer p_i is ensured to be a vertex monomer with a direct path to the closest scatter point c_i. However, this condition may not be true for the dangling ends of the polymer (p_{i-1} and p_{i+1}). To maintain the correct topology, we connect these dangling ends to a small displacement ($\pm 0.05\sigma \cdot (1,1,1)^T$) from the cut monomer ($p_i$), ensuring that the arcs do not intersect with each other. As this only alters the original contour of the polymer by a small displacement, we don't impose any new topological features ((Figure 3.2, Panel D).

- **Connection to the Circle** : Once both termini of polymer i are positioned at a vertex of the convex hull, we extend the arcs outwards towards the circle. The two termini $p_{i\pm1}$ are connected to the corresponding scatter points $c_{i\pm1}$, ensuring that the arcs don't intersect as they reach the circle (Figure 3.2, Panel E).

- **Connection on the Circle** : Following the same procedure for polymer j, four termini are placed on the artificial circle - two of polymer i and two of polymer j. The final step involves connecting these termini in as few steps as possible, by selecting two intermediate points at $\pm\frac{|c_i - c_j|}{2}$ on the circle. This minimizes the number of intermediate points and thus the complexity of the calculation of the Alexander polynomial. After connecting the termini, we have created a super-ring structure (Figure 3.2, Panel F). Finally, we calculate the Alexander Polynomial to assess whether the super-ring is knotted (indicating a deadlock) or unknotted (indicating a disentangled structure).

3.2.3. Degree of Deadlocking

When we examined the results of the deadlock detection method and its limitation, we found that the binary deadlocked/non-deadlocked state of a polymer pair is sensitive to the choice of the cutting points. While one choice of cutting points results in a deadlocked state, another choice results in a non-deadlocked state, meaning that the deadlocked state is not unique. Therefore, we decided to perform multiple reconnections on the same pair at the same timestep and treat the deadlocked state statistically.
In general, we could have performed the reconnection on all possible combination of suitable cutting points. However, many of the reconnections would result in the same super-ring structure, as suitable cutting points could be adjacent along the contour of the polymer. Hence, if suitable cutting points are adjacent along the contour of the polymer or separated by only one monomer, only one representative of this set of suitable cutting points is selected for efficiency. With this procedure, we ensure that all the

relevant cutting points are evaluated, while not wasting resources on already evaluated conformations.
We define a new quantity, the *degree of deadlocking* ξ, which is defined as

$$\xi = \frac{n_{knots}}{n_{all}} \in [0, 1], \tag{3.21}$$

where n_{knots} is the number of reconnections that result in a knot and n_{all} is the number of attempted reconnections. Note, that n_{all} varies greatly depending on the polymers conformation.
Using the protocol of evaluating n_{all} different reconnections of the same pair at the same timestep, we not only gain information on the binary deadlocked/non-deadlocked state of the polymer pair, but also on the degree of deadlocking between them. Based on the value of ξ, we classify the data into tight and loose knots, with the overall goal to investigate whether pairs with a different value of ξ behave differently. Therefore, we define four distinct groups of deadlocks based on their value of ξ. Group 0 consists of non-deadlocked pairs. The motive of keeping this group is to distinguish properties characteristic for deadlocks to those of pairs with similar spacial properties, as elements in Group 0 are also linearly non-separable but they do not show any degree of deadlocking. Representatives of Group 1 are loosely deadlocked, where most of the attempted reconnections result in the non-deadlocked state. Group 3 consists of pairs, in which more then half the reconnections result in a deadlock. Lastly, representatives of Group 2 are intermediately deadlocked rings, bridging the gap between loosely deadlocked and highly deadlocked pairs.

$$\begin{aligned} &\text{Group 0:} && \xi = 0.0 \\ &\text{Group 1:} && 0.0 < \xi \leq 0.1 \\ &\text{Group 2:} && 0.1 < \xi \leq 0.5 \\ &\text{Group 3:} && 0.5 < \xi \leq 1.0 \end{aligned} \tag{3.22}$$

Choosing the boundaries for the individual groups was an iterative process. We noticed, that certain distributions for all deadlocked pairs with $\xi > 0$, e.g. d_C distributions, resemble a sum of distributions with different behaviors. When playing around with the boundaries, the individual distributions eventually emerged and we found that the same grouping leads to nicely discomposed distributions for a variety of analyzed quantities.
The degree of deadlocking ξ itself, rather than the group classification, carries the physical information about the polymer pair's entanglement state. The grouping serves primarily as a tool to investigate whether polymer pairs with similar ξ values exhibit comparable physical behavior. While the boundaries between groups are chosen to effectively separate distinct behavioral regimes, they are not derived from underlying physical principles and could, in principle, be defined differently.

4. Equilibrium

We investigate the properties of deadlocks in a ring polymer melt under equilibrium conditions. The primary aim of this analysis is to determine whether deadlocks emerge in equilibrium and, if so, to characterize their behavior. Specifically, we focus on understanding:

- **Deadlock Formation**: How common are deadlocks in an equilibrated ring polymer melt?
- **Deadlock Persistence**: How long do these structures survive over time?
- **Static Properties**: Do deadlocked rings exhibit distinct structural characteristics compared to non-deadlocked pairs?
- **Dynamic Impact**: How do deadlocks influence the dynamic transport properties of individual polymers in the melt?

4.1. Equilibrium Simulation

A molecular dynamics simulation of a ring polymer melt in equilibrium was performed to generate the particle configurations required for subsequent analysis. Ensuring the system has fully relaxed to equilibrium is essential, as this guarantees that the observed particle motion reflects the expected behavior in a real system.
In the following subsection, we describe the initialization process of the simulation, where the ring polymers are placed into the simulation box, and the system undergoes a series of steps to ensure that it reaches the correct density and topology. This is followed by confirming the equilibrium state of the simulation, where we monitor the system's dynamics, specifically the $g_3(t)$, to verify that the system has fully equilibrated before any data sampling is performed.

4.1.1. Initialization, System Parameters and Integration

We simulate a system comprising $M = 1600$ ring polymers, each of $N = 200$ monomer at a monomer density of $\rho = 0.85\sigma^3$.
The first step of the simulation is to generate initial particle positions, from which the system can be propagated in time. Creating particle positions at high densities is tricky, because particles must be packed closely together without overlapping, while also respecting the polymers chain connectivity.

This conformation was initially set up in a low-density environment, where the individual rings were initialized as perfect circles with random orientations. These circles were placed on a cubic lattice, with a lattice constant exceeding the diameter of the rings to ensure that there was no overlap between rings, thereby avoiding any catenation at this stage. Once the initial configuration was set, the simulation box was gradually shrunk to reach the desired particle density of $0.85\sigma^{-3}$. This controlled compression ensured that the topology of the rings remained unaltered, and no catenation or topological defects were introduced in the system.
The equilibrium MD simulation was carried using LAMMPS [31] (Large-Scale Atomic/-Molecular Massively Parallel Simulator), an open-source software designed for simulating molecular dynamics systems. The specific implementation in LAMMPS, including the chosen interaction potential parameters, as well as the implementation of the Velocity Verlet integration method in combination with a Langevin thermostat is provided in Appendix A.0.1.

4.1.2. Confirming the Equilibrium State

Before we start to sample and analyze equilibrium conformations, we have to confirm that the system has reached equilibrium, meaning that the slowest-relaxing quantities have relaxed. While we don't know what the slowest-relaxing quantity truly is, a good indication is to check wether structural properties, such as the R_g, have relaxed. Typically, when the system reaches a diffusive regime, all structural single-ring properties have relaxed and we consider the system to have reached equilibrium. Therefore, we computed the $g_3(t)$, shown in Figure 4.1 in log-log scale. Initially, the system is in a subdiffusive regime, consistent with literature values for nonconcatenated ring polymers in a melt [17] , before transitioning into a diffusive regime, indicated by the linear scaling in t (e.g. $g_3(t) \propto t$). This linear scaling signifies that the local modes in the polymer have relaxed and the particles are now diffusing.
The diffusion time of the system is defined as the average time it takes for the polymer to diffuse a distance comparable to its own size, e.g. $g_3(\tau_D) = R_g^2$. To extract the diffusion time, we computed the average R_g^2 for each ring, from which we have found that the diffusion time of the system is

$$\tau_D = 28200\tau,$$

as indicated by a blue scatter point in Figure 4.1.
The equilibrium MD simulation was carried out for 10^6 steps $\simeq 35\tau_D$, way longer then one diffusion time, to ensure that the system has lost its memory of the initialization process and has reached equilibrium.

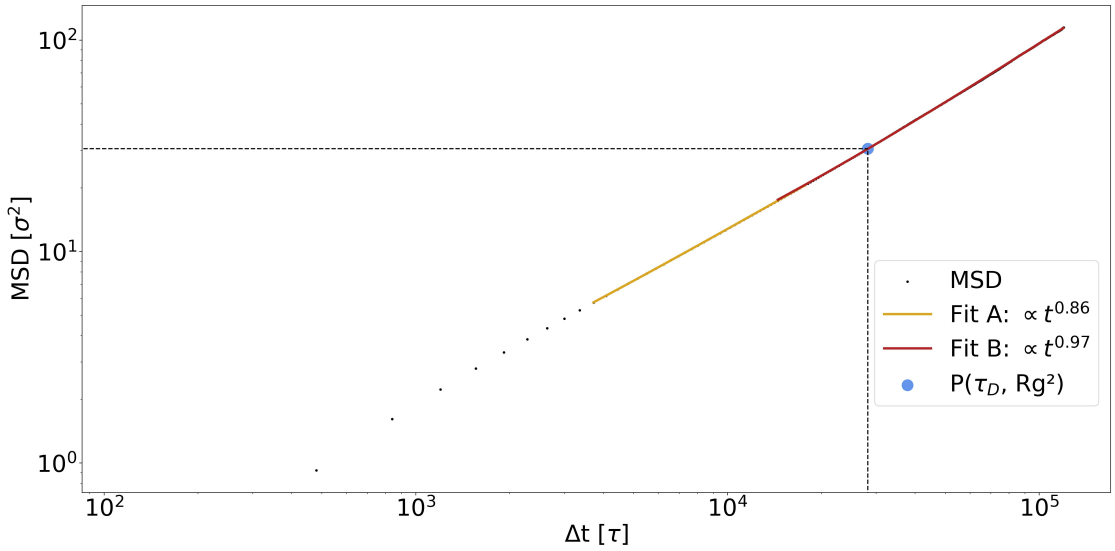

Figure 4.1.: Mean Squared Displacement of the center of mass of the MD equilibrium simulation of $M = 1600$ ring polymer, each of $N = 200$ monomers. The cross at R_g^2 and the diffusion time τ_D is indicated by a blue scatter point.

4.2. Deadlock Detection Series

Once we confirmed the equilibrium state of the molecular dynamics simulation, we selected equilibrated snapshots for the deadlock analysis. Three distinct time-series are analyzed: ts_1, ts_2 and ts_3. Each time-series is designed to address different aspects of the deadlock behavior in the ring polymer melt, including their formation, persistence, static and dynamic properties.
The properties of these time-series are summarized in Table 4.1

Time-Series Abbreviation	Number of Snapshots n_s	Separating Timesteps Δt [τ]	Total Time-Range t_{tot} [τ]
ts_1	14	10800 = 0.38 τ_D	151200 = 5.36 τ_D
ts_2	30	1080 = 0.04 τ_D	32400 = 1.15 τ_D
ts_3	30	4320 = 0.15 τ_D	129600 = 4.56 τ_D

Table 4.1.: Analyzed Time-Series of Deadlocks in Equilibrium.

Time-series ts_1 consists of 14 timesteps, each separated by 10800τ. This longer separation between timesteps is ideal for capturing the overall distribution of deadlocks and their formation frequency in equilibrium. By evaluating these time intervals, we aim to gain insights into how common deadlocked structures are in an equilibrated ring polymer melt.

Time-series ts_2 consists of 30 timesteps separated by 1080τ. This time-series is designed to explore the persistence of deadlocks on shorter time scales. By analyzing the dynamics of deadlocked structures over these intervals, the survival time of deadlocked configurations is determined, and any temporal correlations are examined. Moreover, this time-series serves as a basis for studying the impact of deadlocks on the dynamic transport properties of individual polymers in the melt on small time-scales.
Time-series ts_3 consists of 30 timesteps separated by 4320τ, and covers a broader time range. This time-series is designed to capture the long-term evolution of deadlocks, particularly those that persist beyond the duration of the shorter time-series. The longer time intervals allow for the observation of more stable deadlock configurations, providing additional insight into the survival of deadlocks and their role in the dynamics of the melt over extended time scales. Additionally, this time-series is used to investigate the spatial properties of deadlocks in equilibrium. The properties derived from this time-series complement the analysis of the dynamic behavior of deadlocks observed in ts_2, allowing for a more comprehensive understanding of the relationship between deadlocks and polymer motion over both, short and long timescales.

4.3. Results and Interpretation

We investigate the properties of deadlocks in the ring polymer melt under equilibrium conditions throughout various distributions. Each distribution is presented as an overall distribution for all deadlocked pairs with $\xi > 0$, as well as group-dependent distributions based on the value of ξ, as defined in equation 3.22. Group-dependent distributions include Group 0 as a reference, representing non-deadlocked pairs that share similar spatial arrangements to deadlocked pairs despite not being deadlocked themselves.
To provide a comprehensive overview, all the analyzed properties are displayed in a correlation matrix, which highlights the connection between the various quantities observed throughout the study.

4.3.1. Deadlock Formation in Equilibrium

The primary goal of this section is to determine if deadlocks occur in the equilibrium state of a ring polymer melt. For this purpose, we evaluated time-series ts_1 and the number of deadlocks, $N_\xi(t)$, was tracked as a function of time. On average, the system contains

$$\langle N_{\xi>0} \rangle_t = 659.36 \pm 21.61$$

deadlocked pairs, where each pair is considered deadlocked if $\xi > 0$. However, when only pairs with a higher degree of deadlocking, $\xi > 0.5$, are considered, the average number of deadlocks drops significantly to

$$\langle N_{\xi>0.5} \rangle_t = 33.79 \pm 2.60.$$

This shows, that while deadlocks are common in the system, most of them involve a low degree of deadlocking. Figure 4.2 illustrates this difference, showing that deadlocks with a lower degree of deadlocking are much more frequent than those with higher degrees of deadlocking.

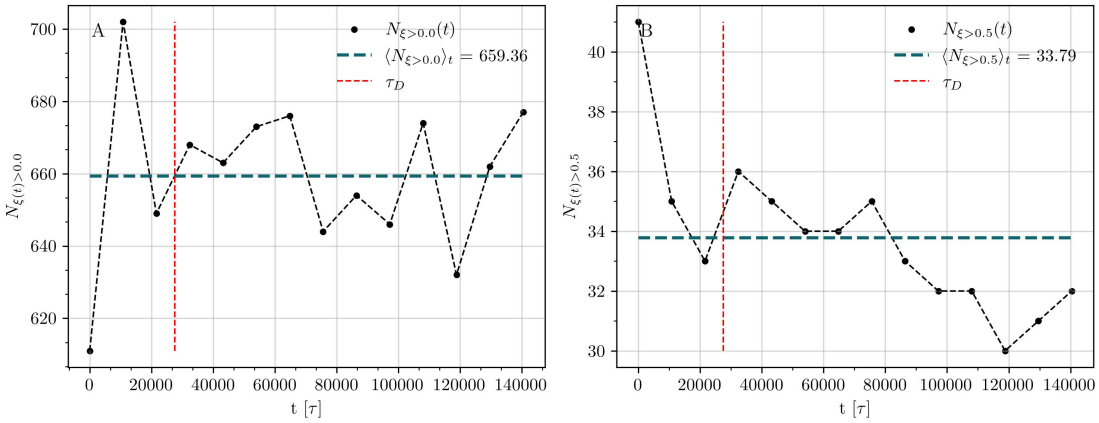

Figure 4.2.: Total number of deadlocks found in time-series ts_1. Panel A shows the population of deadlocks with $\xi > 0$, whereas panel B shows the population of deadlocks with $\xi > 0.5$.

The number of deadlocks remains fairly stable over time, with only minor fluctuations around the average value. This suggests that the process of deadlock formation and disappearance is well balanced. The system appears to reach equilibrium, where deadlocks are constantly forming and disappearing without any large changes in the overall number. Next, the distribution of the degree of deadlocking, ξ, is analyzed for all pairs with $\xi > 0$. The results show that the number of pairs decreases significantly, as ξ increases. Most deadlocks involve a relatively low degree of deadlocking, while pairs with a fully deadlocked state ($\xi = 1$) are quite rare, as shown in Figure 4.3.

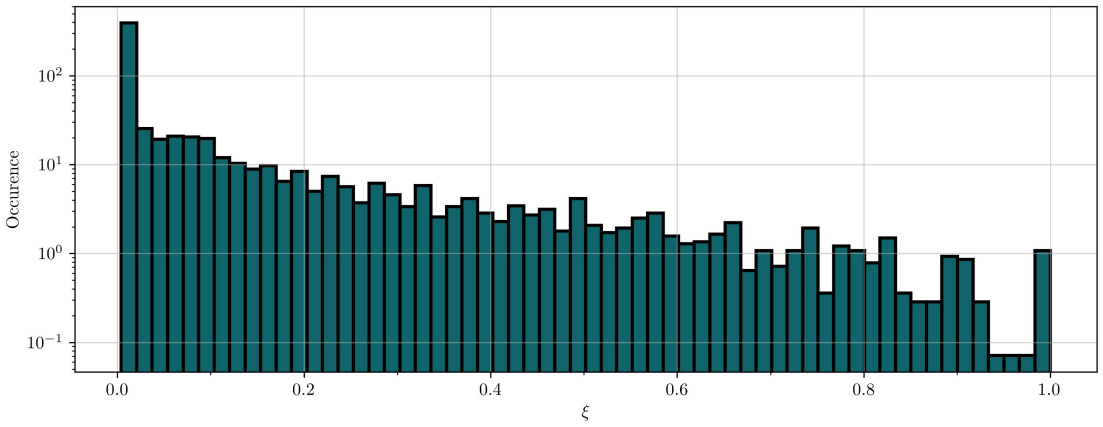

Figure 4.3.: Distribution of the time-averaged occurrence of the degree of deadlocking (ξ) for time-series ts_1, shown with linear-logarithmic axes.

We found, that 99% of non-linear separable pairs that were initially investigated are not deadlocked, and hence belong to Group 0. The remaining 1% of polymer pairs are spread across Groups 1 (75.6%), 2 (19.3%), and 3 (5.2%).
In summary, deadlocks do occur in the system, but they are mostly loosely deadlocked, with only a small fraction of pairs exhibiting tighter deadlocked conformations.

4.3.2. Deadlock Persistence in Equilibrium

In this section, we investigate the persistence, or survival time, of deadlocks in the equilibrium state of the ring polymer melt. The primary goal is to understand how long deadlocked pairs remain locked before becoming disentangled. We examine several properties related to this persistence, including the distribution of the longest survival time of deadlocked pairs and the autocorrelation function as a measure of likelihood that a deadlocked pair remains deadlocked over time.
The first analyzed property is the longest survival time t_s of deadlocks. For this analysis, we generated a binary sequence for each deadlocked pair, where each entry corresponds to a snapshot in the time-series ts_2. Each entry in the sequence is marked as either 1 (deadlocked, with $\xi > 0$) or 0 (not deadlocked, with $\xi = 0$). The longest sequence of consecutive ones corresponds to the longest survival time for a given deadlocked pair.
The distribution of t_s for all deadlocked pairs reveals that most deadlocks persist only for a single timestep, corresponding to a survival time of less than $1080\tau \approx 0.04\tau_D$, a fraction of the diffusion time. This is consistent with the finding that the conformational relaxation time of a ring is much smaller than the diffusion time [17]. However, a small fraction of deadlocks persist for the full duration of the time-series, lasting up to $1.14\tau_D$. These results are shown in Figure 4.4 (panel A).

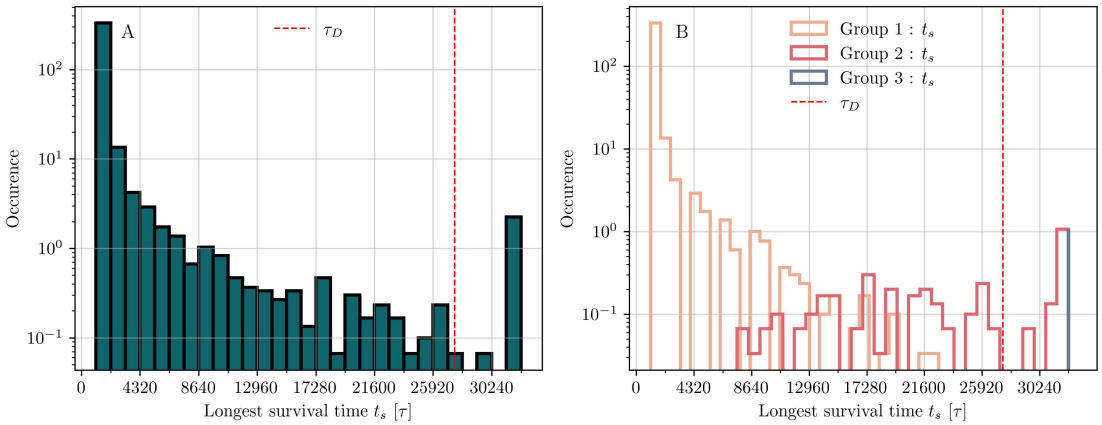

Figure 4.4.: Distribution of the longest survival time t_s of a deadlock for time-series ts_2. Panel A shows the distribution of t_s for all deadlocked pairs. Panel B shows the group-dependent distribution, where the group membership is based on the mean degree of deadlocking over the longest sequence of consecutive deadlocked states.

We then explore whether deadlocks with different degrees of deadlocking exhibit different survival times. By classifying the data based on the mean degree of deadlocking over the longest sequence of consecutive deadlocked states, we observe distinct survival behaviors for each group. Ring pairs with a low degree of deadlocking (Group 1) tend to have shorter survival times, while all pairs in Group 3 persist for the full duration of $1.14\tau_D$. The group-specific distributions of t_s are shown in Figure 4.4 (panel B).
To gain a deeper understanding of deadlock persistence, the autocorrelation function of the binary sequence of deadlocked/non-deadlocked states is computed for all polymer pairs in time-series ts_2. This function reveals the likelihood that a deadlocked pair remains deadlocked over successive timesteps.
The autocorrelation function shows a sharp drop after the first timestep, indicating that most deadlocked pairs disentangle very quickly. After this rapid decay, the function decreases more gradually, suggesting that while most deadlocks are short lived, some do persist for longer times. These results are presented in Figure 4.5.

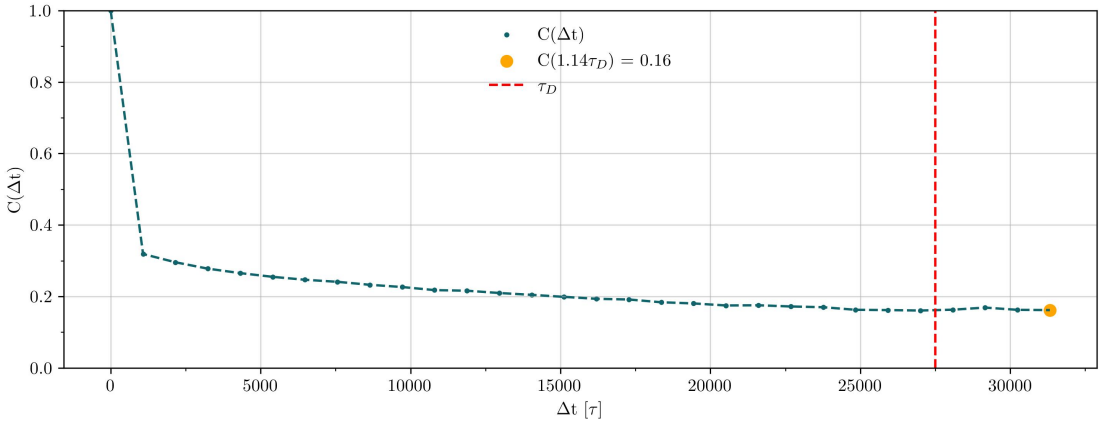

Figure 4.5.: Autocorrelation function of deadlocked pairs as a measure of likelihood of a polymer pair staying deadlocked over time.

To examine the stability of polymer pairs within specific groups, we create binary sequences for Group 1, Group 2, and Group 3, respectively. Each sequence corresponds to one deadlocked pair and consists of 30 values, each representing a timestep in ts_2. An entry in the sequence is marked as 1, if the polymer pair belongs to that group at that timestep and 0, if it belongs to another group. These binary sequences are then used to calculate the autocorrelation function, which measures the likelihood of a polymer pair remaining within the same group over time.
For Group 1, the autocorrelation function decays rapidly after the first timestep, reflecting that pairs with low degrees of deadlocking typically disentangle or change group membership quickly. Group 2 shows a more gradual decay, indicating that some pairs in Group 2 persist for a longer time before transitioning. The autocorrelation function for Group 3 decays very slowly, suggesting that pairs with a high degree of deadlocking remain stable over long timescales, well beyond the observation period. These group-specific autocorrelation functions are shown in Figure 4.6. These results complement and confirm the group-dependent persistence behavior observed above.

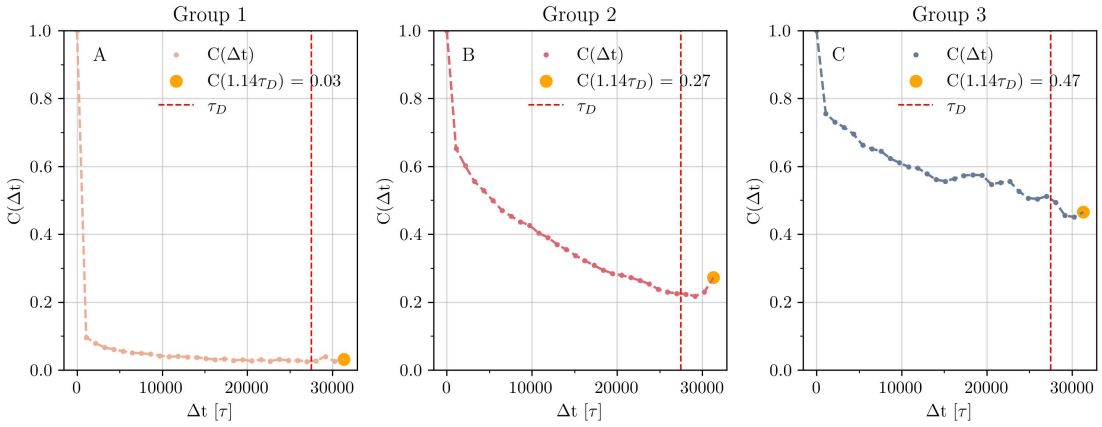

Figure 4.6.: Autocorrelation function of deadlocked pairs remaining in Group 1, Group 2 and Group 3, respectively. The values are based on the analyzed timesteps of time-series ts_2.

Since the autocorrelation function for pairs in Group 2 and Group 3 decays slowly, the time range analyzed so far does not fully capture the long-term persistence of highly deadlocked pairs. To address this, we extend the analysis to a longer time-range of $4.56\tau_D$ using time-series ts_3. This extended time range is sufficient to capture the stability of deadlocked pairs in Group 2, where the autocorrelation function fully decorrelates.
For Group 3, the autocorrelation function remains at approximately 0.21 after a duration exceeding $4\tau_D$, indicating that highly deadlocked pairs remain highly deadlocked for extended periods. This slow decorrelation suggests that some of these highly deadlocked states are strongly meta stable in equilibrium, lasting longer than the observed time-frame in ts_3. The extended analysis is shown in Figure 4.7.

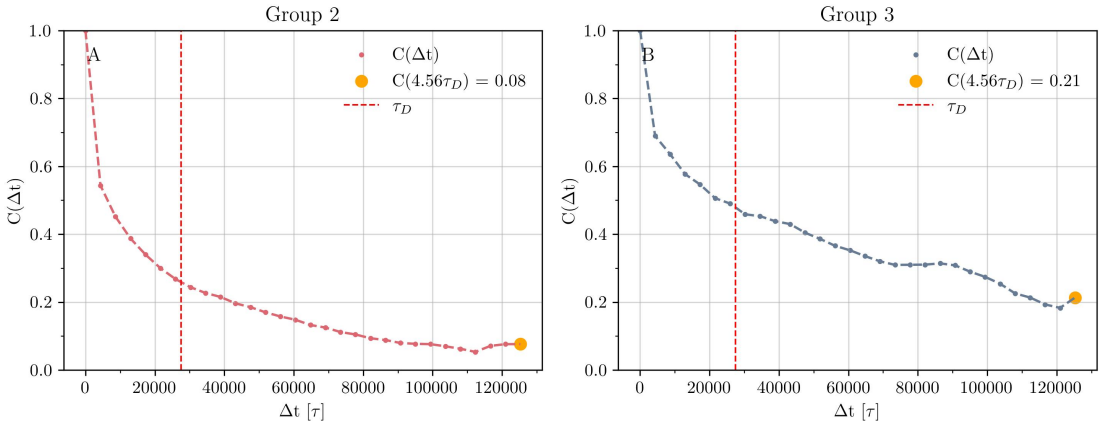

Figure 4.7.: Autocorrelation function of deadlocked pairs remaining in Group 2 and Group 3, respectively. The values are based on the analyzed timesteps of time-series ts_3.

4.3.3. Static Properties of Deadlocks in Equilibrium

The static spatial properties of deadlocked ring polymer pairs in equilibrium are analyzed through a variety of distributions. These include the radius of gyration, the eigenvalues of the gyration tensor, the center of mass distance between the two rings involved in the deadlock and the distribution of the maximal intermonomer distance. Additionally, the spatial characteristics of the deadlocked region is examined by analyzing distributions of the shared volume, the radius of gyration and the eigenvalues of the gyration tensor for monomers within the intersecting region between the deadlocked pairs. The aim is to quantify and compare these static properties to determine whether deadlocked pairs exhibit any distinct structural features relative to non-deadlocked pairs.
All analyzed quantities are based on the analyzed time-series ts_3, providing a detailed view of the equilibrium conformations of both deadlocked and non-deadlocked ring polymer pairs. Furthermore, we found that the analyzed quantities in this section are not time-dependent, hence we present the time-averaged data.

Gyration Analysis

To gain insight into the conformational properties of deadlocked polymer pairs, we examine the distribution of the radius of gyration (R_g) and the eigenvalues of the gyration tensor ($\lambda_1^2 \geq \lambda_2^2 \geq \lambda_3^2$). These quantities provide information about the compactness and shape of the polymer pairs. Specifically, R_g reflects the overall size of the pair, while the eigenvalues describe the spatial distribution along the three principal axes.
We calculate the gyration tensor for each polymer pair using the monomer positions from both rings. The properties derived from the gyration tensor of the polymer pair allow

us to explore the spatial distribution of the pair as a whole, rather than focusing on the properties of each individual ring.
The R_g distribution for all deadlocked pairs is shown in Figure 4.8, panel A. A further breakdown of the data reveals how the radius of gyration varies across different groups of deadlocked pairs. Group 0, which consists of non-deadlocked pairs, shows a relatively large R_g. In contrast, the distributions for Group 2 and Group 3 shift toward smaller values of R_g, indicating a more compact structure of the pair as the degree of deadlocking increases. These group-dependent R_g distributions are shown in Figure 4.8, panel B.
Additionally, we compute the R_g for each pair individually and categorized the data according to ξ, the degree of deadlocking of the pair, each individual ring is involved in. Interestingly, the conformation of each ring individually does not appear to be influenced by the degree of deadlocking. Across all values of ξ, the mean R_g for individual rings was found to be $\langle R_{g,ind} \rangle \approx 5.53\sigma$. While the distribution of R_g for pairs with different values of ξ shows clear differences, the same property for individual rings does not seem to be influenced by the degree of deadlocking.

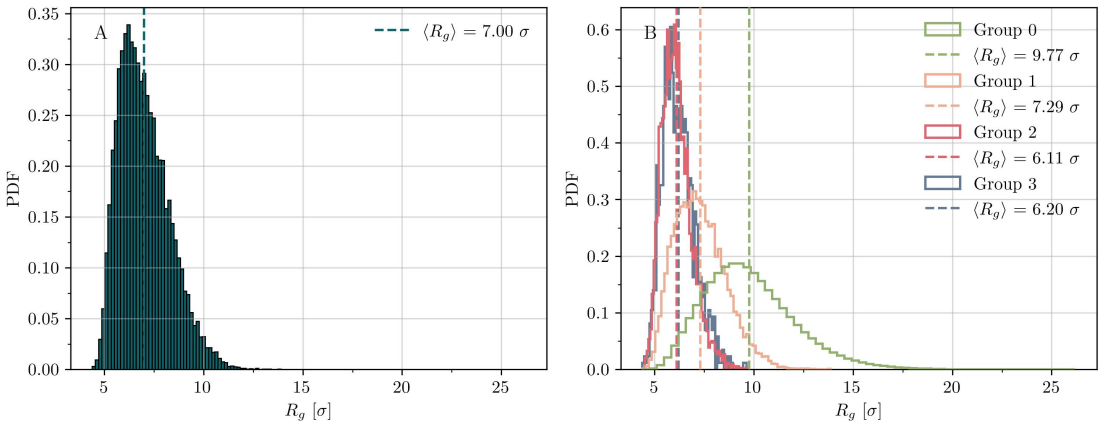

Figure 4.8.: Distribution of the radius of gyration, calculated from time-series ts_3. Panel A shows the R_g distribution for all pairs with $\xi > 0$, whereas panel B shows the group-dependent distributions.

We further quantify the shape of deadlocked polymer pairs by analyzing the eigenvalues of the gyration tensor. While the distribution of R_g provides a measure of the average compactness, the eigenvalues of the gyration tensor offer insight into the spatial anisotropy of the pairs. To make quantitative comparisons independent of the overall size of the polymer pair, the eigenvalues are rescaled by the corresponding R_g^2.
As shown in Figure 4.9, Group 0 exhibits a higher degree of anisotropy, with a relatively large difference between the largest and smallest eigenvalues. This suggests that non-deadlocked pairs are more elongated. However, as the degree of deadlocking increases, these differences become more balanced, indicating that the polymer pairs approach a more isotropic shape as ξ increases.

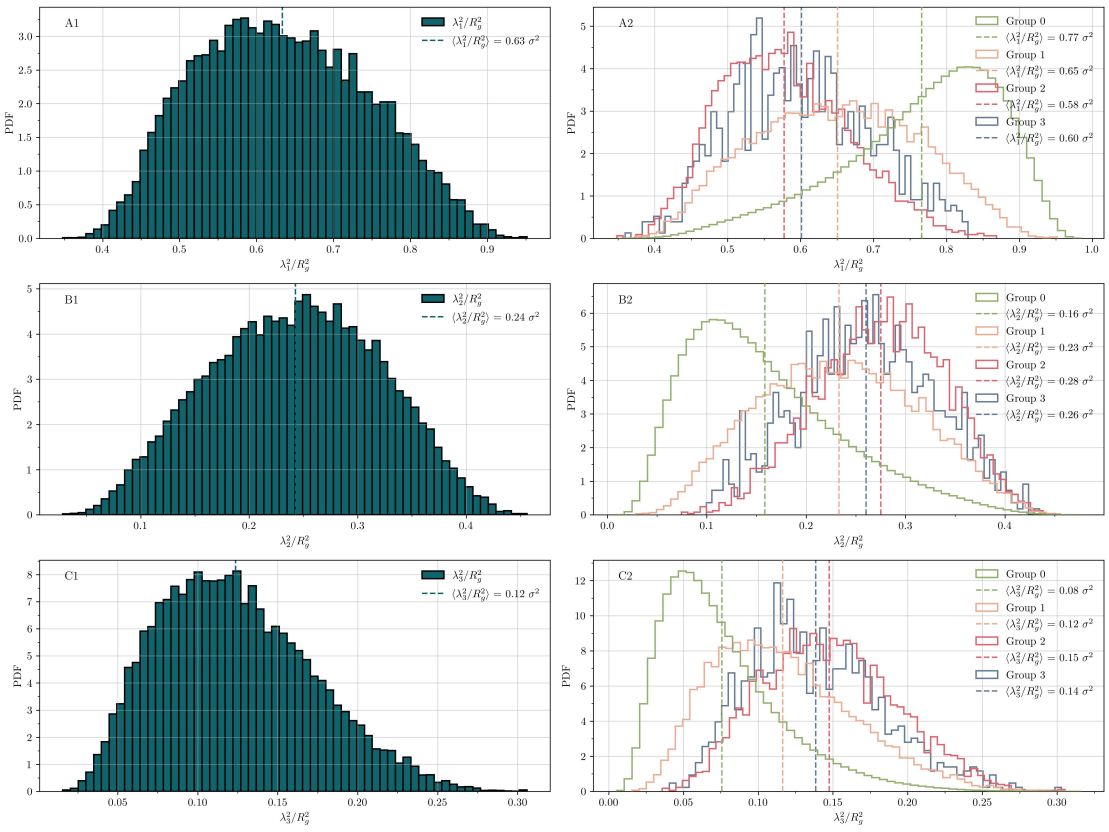

Figure 4.9.: Distribution of the eigenvalues of the gyration tensor, calculated from time-series ts_3 for every deadlocked polymer pair. Panels on the left show the distribution of eigenvalues for all pairs with $\xi > 0$, whereas panels on the right show the eigenvalue distribution for the grouped data.

.

Center of Mass Distance

We investigate the spatial relationship between the center of masses of deadlocked polymer pairs. By examining the distance between the center of masses (d_C), we aim to understand how the degree of deadlocking influences the relative positioning of the two rings.
For this analysis, we calculate the center of mass position for all linearly non-separable pairs of rings. In order to directly compare the data, we rescale the center of mass distance by the corresponding R_g values, presenting the distribution of d_C/R_g. This rescaling removes the dependence on the overall size of the polymer pairs, allowing for a more meaningful comparison across different groups.
The rescaled center of mass distance distributions reveal a clear trend: the mean separation between the centers of mass of highly deadlocked pairs (Groups 2 and 3) is significantly

smaller compared to that of Group 0 and Group 1 (Figure 4.10). These findings suggest that, as the degree of deadlocking increases, the polymer pairs become more compact and the distance between the center of masses of the two rings decreases.

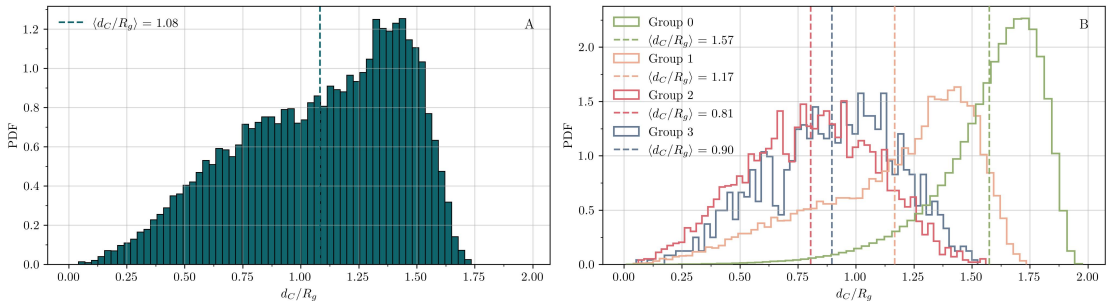

Figure 4.10.: Distribution of the center of mass distance between linearly non-separable pairs, calculated from time-series ts_3. Panel A shows the overall d_C distribution for all pairs with $\xi > 0$, while panel B shows the group-dependent distributions of d_C.

Maximum Intermonomer Distance

We next investigate, whether the maximal intermonomer distance (d_m) between any two monomers in the polymer pair is influenced by the degree of deadlocking. In order to make the distributions comparable across different groups, we again rescale d_m by the corresponding R_g, giving rise to the distribution of d_m/R_g shown in Figure 4.11.
So far, we have found that pairs with high degrees of deadlocking are more compact, their conformation approaches a more isotropic arrangement and their center of masses are closer together in space. Intuitively, we expected the maximal intermonomer distance to resemble the distribution of the largest eigenvalue of the gyration tensor, but the findings in Figure 4.11 do not support our intuition. Instead, deadlocked pairs behave similarly across all values $\xi > 0$, where only the distribution of the non-deadlocked pairs is shifted to smaller values.

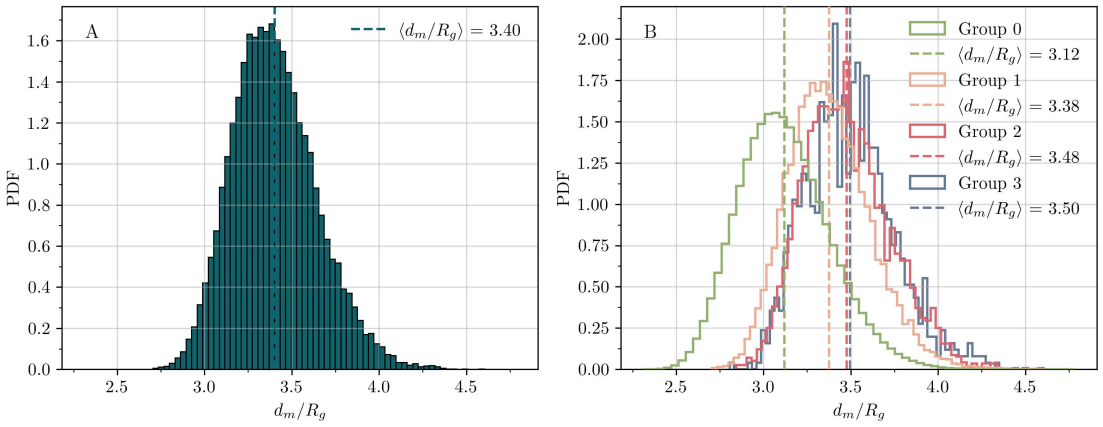

Figure 4.11.: Distribution of the maximal intermonomer distance d_m, normalized by the gyration radius R_g between linearly non-separable pairs, calculated from time-series ts_3. Panel A shows the overall distribution of d_m/R_g for all pairs with $\xi > 0$, while panel B shows the group-dependent distributions.

Overlapping Volume Analysis

We investigate the spatial characteristics of the overlapping region between two polymer rings in a deadlocked state. For this analysis, we identify all monomers of polymer i that are inside the convex hull of polymer j, and vise versa. These monomers, labeled *overlapping monomers*, define the overlapping region, where the volume of one polymer intersects with the volume occupied by the other ring involved in the deadlock. To obtain a measure of this volume, we construct a convex hull around all overlapping monomers. The volume of this convex hull gives rise to the *overlapping volume* (V_O).
The first step of this analysis is to find all overlapping monomers. We use an alternative expression of the convex hull of a set of points X

$$\text{conv}X = \left\{ \sum_{i=1}^{n} \alpha_i x_i \mid x_i \in X, n \in \mathbb{N}, \sum_{i=1}^{n} \alpha_i = 1, \alpha_i \geq 0 \right\}, \tag{4.1}$$

where the convex hull is described by the set of all finite convex combinations [32]. In our case, X is the dataset of all 3D monomer positions of polymer i. Monomer γ of polymer j ($m_{j,\gamma}$) is inside the convex hull of polymer i, if there exists a linear combination $\sum_{i=1}^{n} \beta_i x_i = m_{j,\gamma}$, with $\sum_{i=1}^{n} \beta_i = 1$ and $\beta_i \geq 0$. Practically, we use a linear programming algorithm [33] to find the combination of β_i, which determines whether a point $m_{j,\gamma}$ is inside or outside the convex hull of polymer i. We repeat this procedure for every monomer of polymer j ($m_{j,\gamma}$) and check if it is outside or inside the convex hull of polymer i. If $m_{j,\gamma}$ is inside the convex hull of polymer i, we label the monomer as an overlapping monomer, otherwise we proceed with the next monomer. Then, we reverse

the the expressions and check if a monomer of polymer i ($m_{i,\gamma}$) is inside or outside the convex hull of polymer j, again marking all the monomers that are inside the convex hull. Once we have identified all overlapping monomers of the pair, we construct a convex hull around all overlapping monomers and calculate its volume, as well as the gyration tensor of overlapping monomers. Note, that the overlapping volume might not be a single, continuous region in space - it could involve multiple overlapping sub-regions.
The procedure of finding the overlapping monomers is computationally expensive, and due to the inefficiency of this approach, we only analyze a subset of the data. Specifically, we select 3500 random samples from Group 0, Group 1 and Group 2, respectively, and use all available samples of Group 3, as the number of these pairs is fewer than 3500. For time-series ts_2, this corresponds to 984 conformations for representatives of Group 3.
The distribution of the overlapping volume V_O is shown in Figure 4.12, which presents both, the overall distribution of all pairs with $\xi > 0$ (panel A) and the group-dependent distributions (panel B). We observe clear differences between Groups 0 and 1 to Groups 2 and 3. Non-deadlocked pairs (Group 0) and slightly deadlocked pairs (Group 1) exhibit the maximum of the distribution at very low values, suggesting that the two rings do not overlap extensively but rather occupy their own distinct volumes. Pairs with higher values of ξ share more volume on average. As the degree of deadlocking increases, the overlapping volume increases as well.

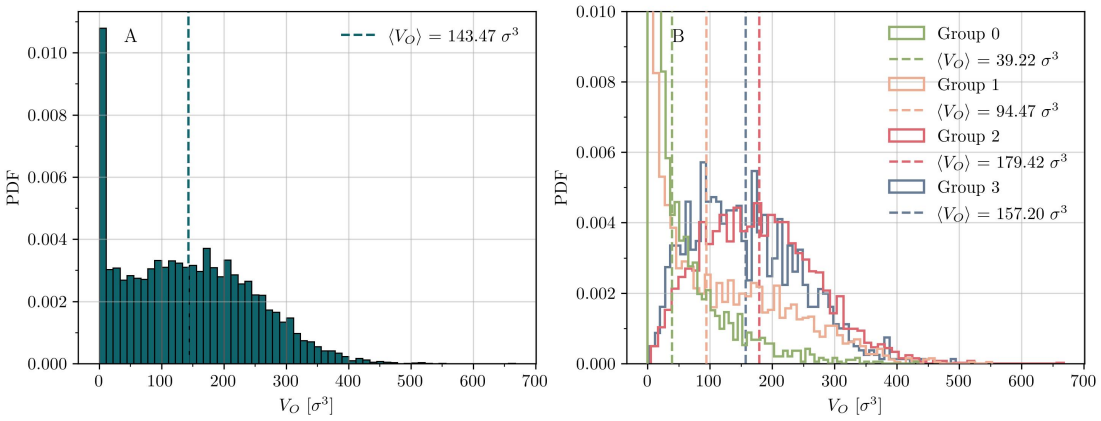

Figure 4.12.: Distribution of the overlapping volume V_O between two deadlocked polymer pairs. The data was generated by analyzing 3500 samples of Group 0 and 1, respectively, as well as all available samples from Group 2 and 3 of time-series ts_3. Panel A shows the overall distribution for all pairs with $\xi > 0$, whereas panel B shows the group-dependent distributions.

Next, we analyze the radius of gyration of the overlapping region, denoted as $R_{g,O}$. To do this, we compute the gyration tensor using the positions of the overlapping monomers, from which we have obtained the corresponding $R_{g,O}$ values.
Figure 4.13 presents the distributions of the radius of gyration of the overlapping region.

Group 2 and 3 exhibit a significantly large mean for $R_{g,O}$, reflecting an extended overlapping region. The mean value of $R_{g,O}$ for Group 2 and 3 is roughly half the value of the R_g of all monomers in the pair, suggesting a substantial portion of the polymer's overall shape is positioned in the overlapping region.
The degree of deadlocking is closely related to the spatial extend of the overlapping region. In fact, the two properties show a 50% cross-correlation.

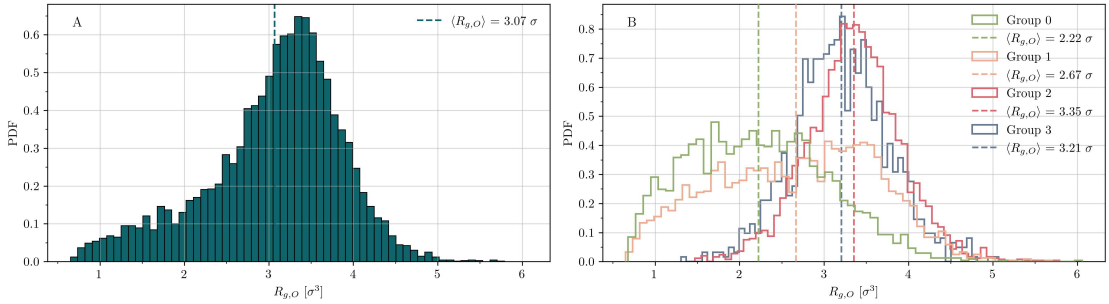

Figure 4.13.: Distribution of the Radius of Gyration, calculated for the sub-set of overlapping monomers of each polymer pair. The data was generated by analyzing 3500 random samples from Group 0 and 1, respectively, as well as all available samples of Groups 2 and 3 of time-series ts_3. Panel A shows the overall distribution of all pairs with $\xi > 0$. Panel B shows the group-dependent distribution of $R_{g,O}$.

To study the anisotropy and spatial distribution of the overlapping region, the eigenvalues of the gyration tensor are calculated for all overlapping monomers. To ensure comparability between different distributions, the eigenvalues are rescaled based on the respective $R_{g,O}$ value. Figure 4.14 displays the distributions of the three rescaled eigenvalues for both, the overall and the group-dependent distributions.
Group 2 and 3 exhibit more compact, constrained extensions along the first principle axis. However, since the overlapping volume might not stem from a single region, large $\lambda^2_{1,O}$ values could also indicate multiple sub-regions. The group dependent distributions of the second largest eigenvalue ($\lambda^2_{2,O}$) are relatively similar across all groups, with values centered around $0.23 - 0.27$. This similarity suggests that the intermediate spatial extension of the overlapping region is largely unaffected by the degree of deadlocking.

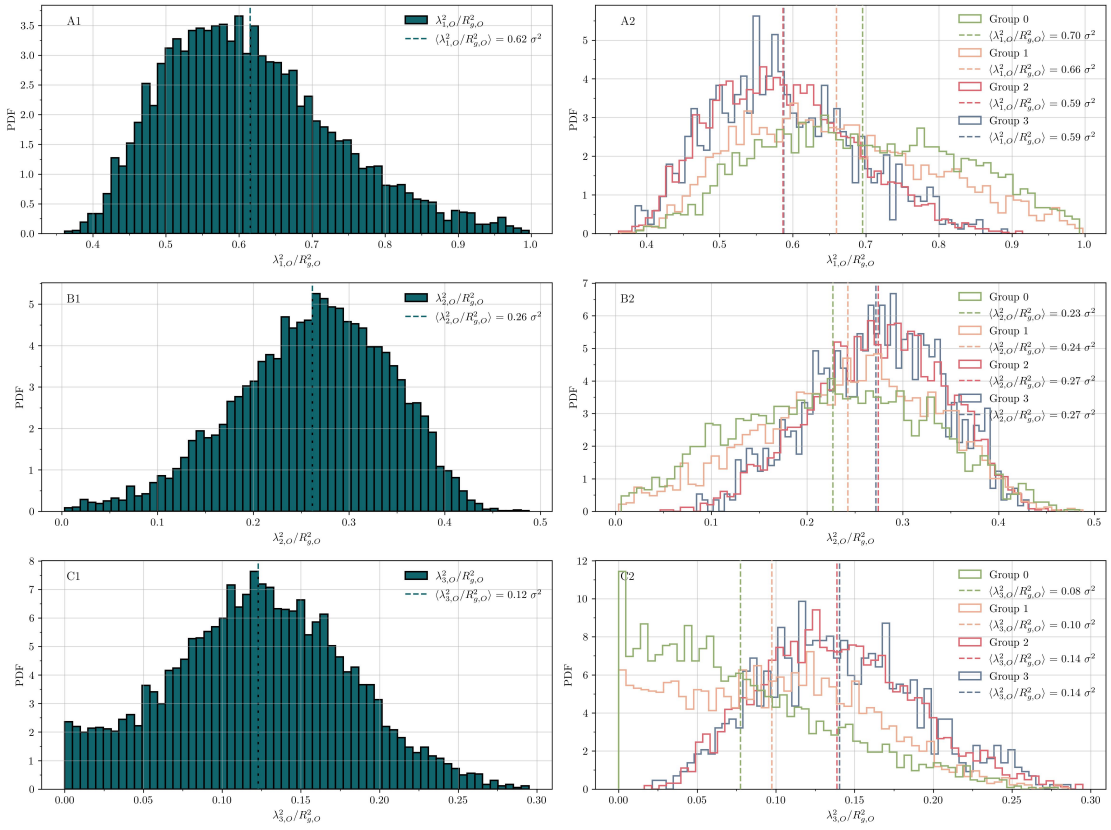

Figure 4.14.: Distributions of the eigenvalues of the gyration tensor, calculated for the overlapping monomers. The eigenvalues are rescaled by the corresponding $R_{g,O}$ value in order to compare different distributions. The data was generated by analyzing 3500 random samples of Group 0 and 1, respectively, and all available samples of Group 2 and 3 of time-series ts_3. Panels on the left display the overall distribution for pairs with $\xi > 0$, whereas panels on the right show the group-dependent distributions.

4.3.4. Dynamic Properties of Deadlocks in Equilibrium

In this section, we investigate the dynamic transport properties of deadlocked ring polymers by analyzing the individual chains motion through $g_3(\Delta t)$. We aim to understand, wether the individual chains movement is affected when it is deadlocked with another chain. Furthermore, we investigate the relative motion between the two rings involved in the deadlock. For the relative motion, we define the relative mean-squared displacement

$$g_{rel}(\Delta t) = \left\langle \left(\vec{R}_{COM,i}(t) - \vec{R}_{COM,j}(t)\right) - \left(\vec{R}_{COM,i}(t+\Delta t) - \vec{R}_{COM,j}(t+\Delta t)\right) \right\rangle^2, \tag{4.2}$$

where $\vec{R}_{COM,i}$ and $\vec{R}_{COM,j}$ are the center of masses of polymer i and polymer j, respectively.
We first investigate the transport properties on small timescales over a period of $1.15\tau_D$ using time-series ts_2. Figure 4.15 shows both, $g_3(\Delta t)$ (open symbols) and $g_{rel}(\Delta t)$ (closed symbols) for all deadlocked pairs with $\xi > 0$ (panel A) as well as for the group dependent distributions (panel B). We observe that the behavior of $g_3(\Delta t)$ across different groups remains is relatively similar. If $g_3(\Delta t)$ exhibited faster diffusion for smaller values of ξ, this could suggest an underlying physical trend. However, since the slopes are not ordered in a consistent way, the observed differences are likely due to statistical noise rather than reflecting any underlying physical behavior. As the behavior of $g_3(\Delta t)$ is largely unaffected by the degree of deadlocking, we conclude that the individual chains motion on small time-scales is not constrained by the deadlock, with individual chains exhibiting similar levels of diffusion across all values of ξ.
The behavior of $g_{rel}(\Delta t)$ validates what we have already found in the previous chapters. For Group 1, we have shown that these pairs are unstable, with deadlocks disentangling quickly. As the deadlock is released, the constraint between the two rings is broken, allowing them to move independently of one another. On average, they are more likely to diffuse in different directions, rather than in the same direction, increasing the absolute distance between them. This behavior is reflected by the fast increase of $g_{rel}(\Delta t)$ for Group 1. Group 0 follows a similar trend, although in this case, the two rings were not deadlocked to begin with, leading to an even faster increase in $g_{rel}(\Delta t)$. On the contrary, pairs with a higher value of ξ are meta stable configurations, lasting longer then one diffusion time. For Group 2 and Group 3, the deadlock forces the two polymers to move coherently, while the individuals chains movement is largely unaffected by the deadlock.

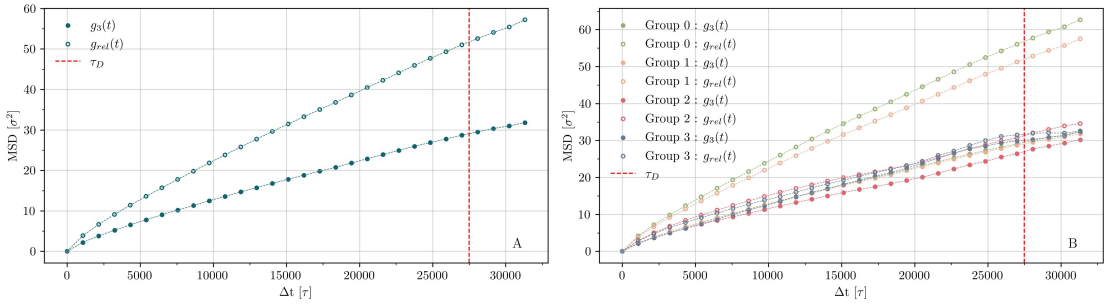

Figure 4.15.: Mean squared displacements of the center of mass motion of individual polymers ($g_3(\Delta t)$) and the relative motion between the center of masses of the two rings ($g_{rel}(\Delta t)$) for all pairs with $\xi > 0$ (panel A) and for the individual groups (panel B). The data was obtained form time-series ts_2.

Next, we evaluate the (squared) displacement of the polymers after one diffusion time. The distance corresponding to the center of mass diffusion of the polymers is denoted as $g_3(\tau_D)$, while the relative distance between the two rings is denoted as $g_{rel}(\tau_D)$. The

distributions of these distances are shown in Figures 4.16 and 4.17, respectively.
For the polymers individual motion, the distributions of $g_3(\tau_D)$ across all groups show similar behavior, with no significant difference between Groups 0, 1, 2, and 3. This suggests that the center of mass motion is largely unaffected by the degree of deadlocking, indicating that the polymer pairs exhibit similar levels of overall mobility on these time-scales.

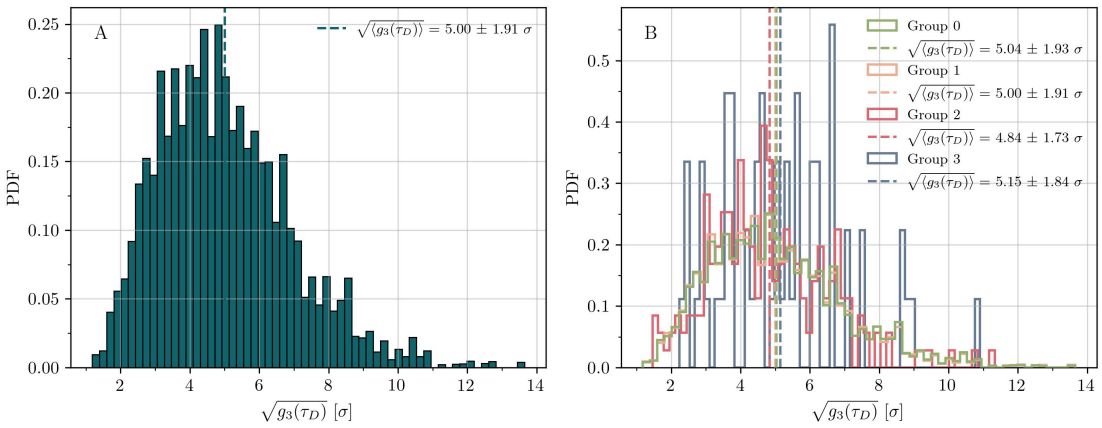

Figure 4.16.: Distributions of the center of mass distance traveled after one diffusion time, for all deadlocked pairs with $\xi > 0$ (panel A) and for the individual groups (panel B). The data was obtained from time-series ts_2.

In contrast, the distributions of $g_{rel}(\tau_D)$ show slight differences across the different groups. As observed from the MSD curves, the relative motion for pairs in Group 2 and Group 3 is more constrained, as reflected by the smaller mean values compared to Groups 0 and 1.

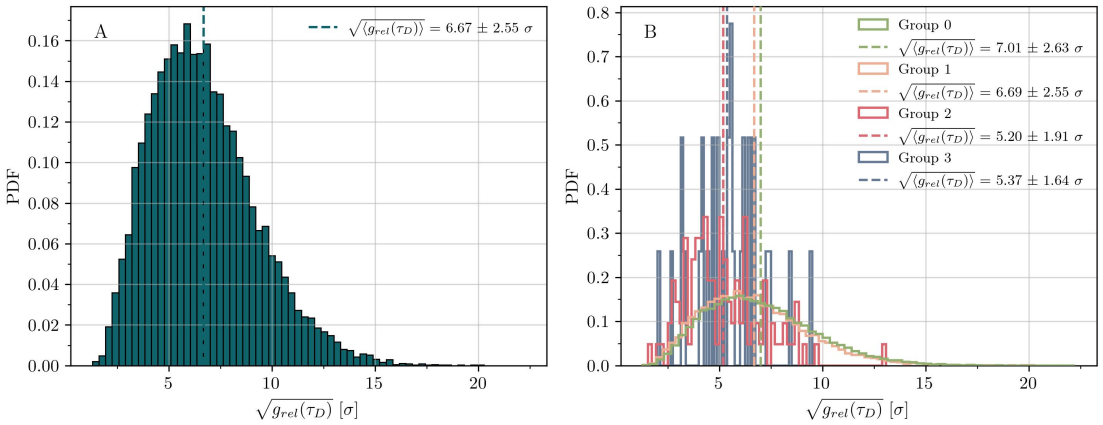

Figure 4.17.: Distributions of the relative distance traveled between the two polymers in the pair after one diffusion time, for all deadlocked pairs with $\xi > 0$ (panel A) and for the individual groups (panel B). The data was obtained from time-series ts_2.

Although evaluating the MSD over a single diffusion time provides insight into the motion of the polymer pairs, it does not fully capture the long-term transport behavior, as deadlocked structures can persist far longer than a single diffusion time. To explore this further, we repeated the MSD analysis for a longer time range of $4.56\tau_D$, using time-series ts_3. The MSD curves over this extended time range are shown in Figure 4.18.
The MSD curves obtained from the extended time-range reveal additional insights into the dynamics of the polymer pairs. Notably, Group 3's $g_{rel}(\Delta t)$ shows clear plateauing at longer times, suggesting that highly deadlocked pairs reach a maximum separation distance. This further indicates, that the deadlock indeed acts as a constraint on the two rings. However, the center of mass motion continues to increase, indicating that while the pair is constrained relative to one another, they still move coherently.

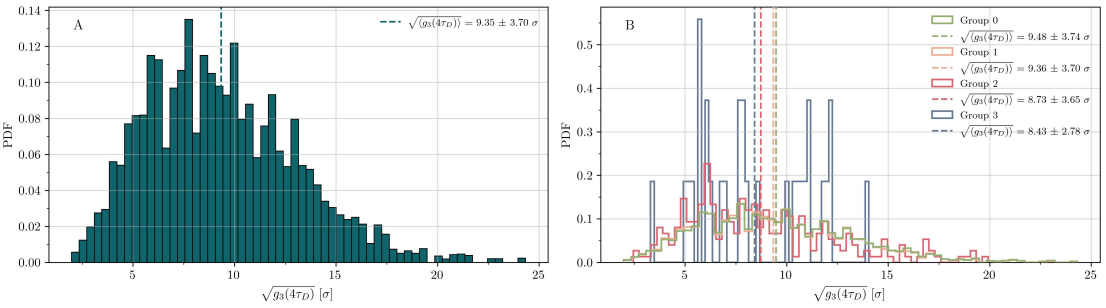

Figure 4.19.: Distributions of the center of mass distance traveled after four diffusion times, for all deadlocked pairs with $\xi > 0$ (panel A) and for the individual groups (panel B). The data was obtained from time-series ts_3.

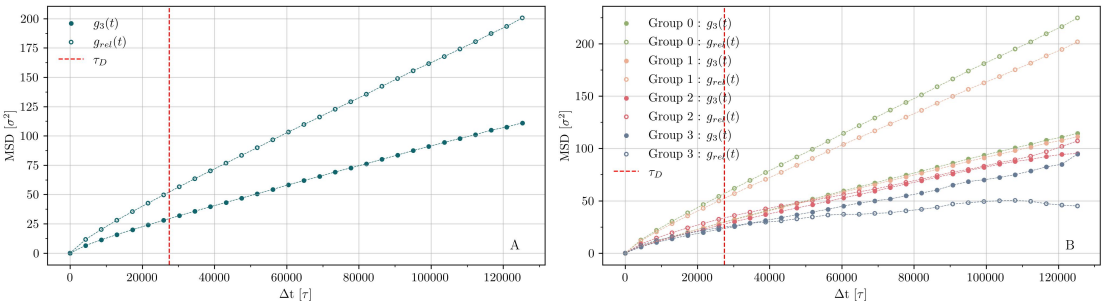

Figure 4.18.: Mean squared displacements of the center of mass motion of the polymer pairs ($g_3(\Delta t)$) and the relative motion between the center of masses of the two rings ($g_{rel}(\Delta t)$) for all pairs with $\xi > 0$ (panel A) and for the individual groups (panel B). The data was obtained form time-series ts_3.

In the longer time interval, the individual chains motion ($g_3(\Delta t)$) shows consistently slower increases as the degree of deadlocking increases. From the shape of $g_3(\Delta t)$ in Figure 4.18, it looks as if the diffusion constant for highly deadlocked pairs is lower than for non-deadlocked and slightly deadlocked pairs. Physically, we expect highly deadlocked pairs to diffuse more slowly than non-deadlocked pairs, as the constraint forces them to move coherently. Two coherently moving polymers have a higher molecular mass, therefore we expect them to diffuse more slowly. However, it is important to note that the differences are highly influenced by the limited samples in Group 3. When looking at the distribution of $g_3(4\tau_D)$ (Figure 4.19), the differences in the distributions is smaller than the uncertainty of the histogram. To figure out whether the diffusion constant is different for pairs that are highly deadlocked compared to the diffusion constant of non-deadlocked pairs, we would have to run further checks.
In conclusion, the analysis of the dynamic properties of deadlocked ring polymer pairs has

provided insights into how deadlocks influence the motion of ring polymer pairs. Highly deadlocked pairs (Groups 2 and 3) exhibit more constrained relative motion, moving coherently, whereas less deadlocked pairs (Groups 0 and 1) show more independent relative diffusion. $g_3(t)$ remains largely unaffected by the degree of deadlocking at small time-scales, indicating that the overall mobility of the pair is less constrained. Over longer time scales, deadlocking effects become more pronounced, particularly in Group 3, where the relative motion plateaus, suggesting a limit to the separation distance between deadlocked rings. Note, that the maximum separation distance found from the plateau of $g_{rel}(t)$ for Group 3 is at 7σ, similar to the mean R_g of Group 3 ($\langle R_g \rangle = 6.2\sigma$) and the mean center-of-mass distance between the two rings ($\langle d_C \rangle = 5.69\sigma$).
The individual chains motion is harder to interpret, as the statistical noise of Group 3 is dominating. We suspect that highly deadlocked rings might diffuse more slowly compared to non-deadlocked pairs as their molecular weight is higher because of the coherent nature of the pair's diffusion. However, the poor statistics do not allow for a definite conclusion.

4.3.5. Correlation Matrix of Equilibrium Quantities

To further investigate the relationships between the various equilibrium properties of deadlocked ring polymers, we construct a correlation matrix, shown in Figure 4.20. The purpose of this analysis is to explore whether any of the polymer properties are strongly correlated with the degree of deadlocking (ξ), which could potentially allow us to predict whether a polymer pair is in a deadlocked state without needing to perform the computationally expensive deadlock detection algorithm.
From the correlation matrix, it becomes clear that there is no single, dominating property that strongly correlates with the degree of deadlocking, making it difficult to predict deadlocking based solely on one static or dynamic property. The highest correlation with ξ is found with the longest survival time (t_s) of the deadlocked state, with a coefficient of 0.89. This suggests that more complex deadlocks, once formed, tend to be more stable over time. However, in order to determine the longest survival time, one already needs the evaluated deadlocked states.

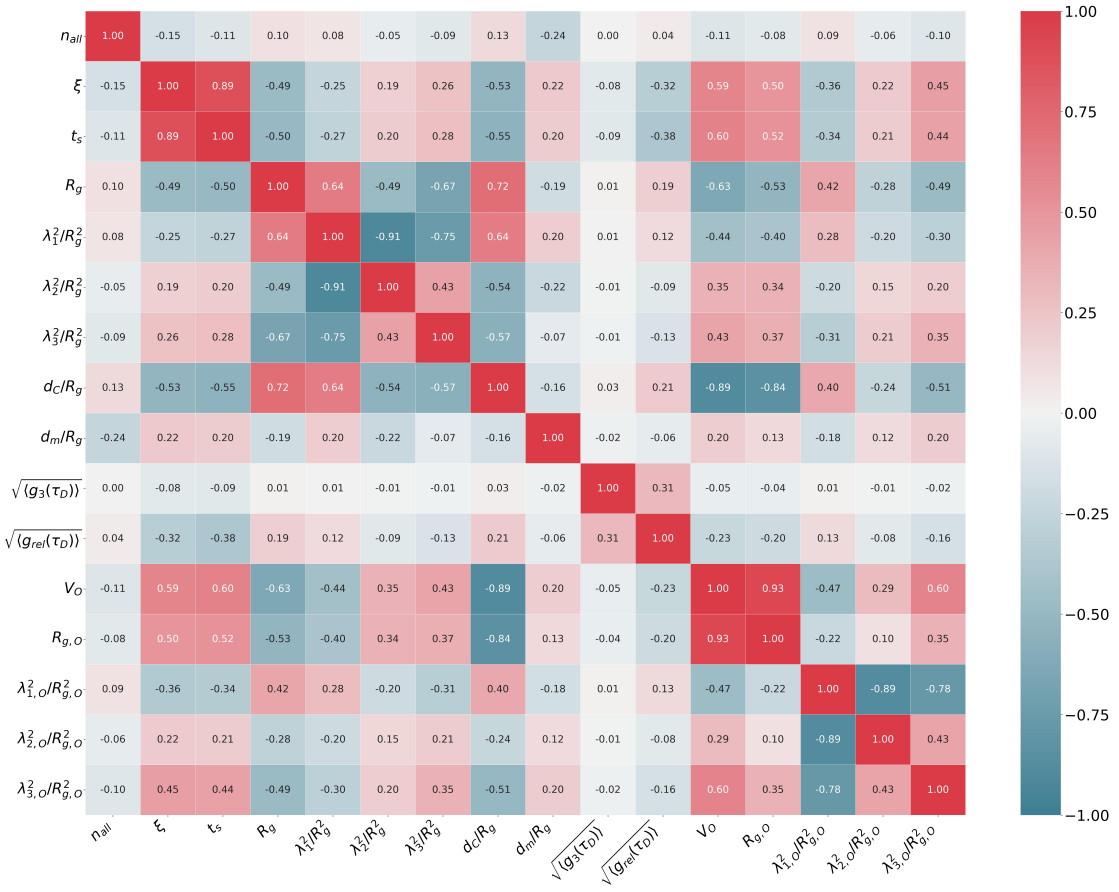

Figure 4.20.: Correlation Matrix of all analyzed equilibrium quantities of sections 4.3.2, 4.3.3 and 4.3.4 of time-series ts_3.

The second strongest correlation with ξ is with the overlapping volume (V_O), with a coefficient of 0.59. As the degree of deadlocking increases, the volume of the overlapping region increases. Additionally, there is an anticorrelation between ξ and the center of mass distance (d_C) with a coefficient of -0.54. This negative correlation suggests that deadlocked pairs tend to have a smaller center-to-center distance compared to non-deadlocked pairs. The radius of gyration of the entire polymer pair (R_g) is moderately anticorrelated with ξ (-0.49), indicating that deadlocked pairs tend to have a smaller overall extension.
However, despite these correlations, there is no property that alone can unambiguously determine whether a polymer pair is deadlocked or not. To further investigate if a combination of structural and dynamical properties can predict the deadlocked state, we conducted principle component analysis (PCA). The results of the PCA analysis revealed that no linear combination of static and dynamic properties was able to predict the deadlocked state. This is why we still rely on the deadlock detection algorithm to accurately identify whether a pair is deadlocked or not.

In conclusion, the correlation matrix highlights several significant relationships between the degree of deadlocking and structural properties such as the overlapping volume, center of mass distance, and radius of gyration. However, it also emphasizes that predicting the deadlocked state of a polymer pair based solely on these properties is not possible, and that the deadlock detection algorithm remains essential for accurately identifying deadlocked configurations.

5. Shear Flow

This chapter investigates the behavior of deadlocks in a ring polymer melt under steady-state shear conditions. Specifically, we examine how the composition of deadlocks is affected by shear forces and whether the viscoelastic properties of the melt correlate with a change in the deadlock composition. The behavior of deadlocks under shear flows is still an ongoing investigation. Here, we present the results of two analyzed shear rates: $\mathrm{Wi} = 8.8$ and $\mathrm{Wi} = 30.0$. We focus on comparing various properties related to the overall composition of deadlocked pairs, their persistence and static behavior of these pairs under two different shear rates.

5.1. Shear Simulation

We performed a non-equilibrium molecular dynamic (NEMD) simulation of a ring polymer melt using the SLLOD integration method to simulate steady-state shear flows. Although the correct implementation of SLLOD for a ring polymer melt would involve using molecular SLLOD equations of motion [29], our simulations were carried out using the atomistic SLLOD approach. While this might restrict certain polymer rotations and deformations (if they even occur), the atomistic SLLOD algorithm has been shown to align well with experimental data [4]. Nevertheless, we explicitly want to point out that using an atomist SLLOD algorithm might lead to slightly different conformations and *could* alter the results of deadlocks under shear. We present the results of deadlocks under steady-state shear conditions under the assumption that the atomistic SLLOD equations of motion are applicable.
We furthermore performed shear simulations using the Müller-Plathe NEMD simulation method, which imposes a momentum flux to obtain the velocity gradient. As this simulation method does not enforce the flow profile directly into the system, the Müller Plathe Method does not suffer from the same problems as the atomistic SLLOD method. For brevity, we will not report on these results but we do plan it in future publications.
In the following sections, we describe our simulation setup and integration method for simulating the ring polymer melt under steady-state shear conditions using the atomistic SLLOD equations of motion (see equation 3.15 and 3.16).

5.1.1. Initialization, System Parameters and Integration

As in our equilibrium simulation, our system comprises $M = 1600$ ring polymers, each of $N = 200$ monomers at a monomer density of $\rho = 0.85\sigma^{-3}$. While we used a cubic simulation box for the equilibrium simulation, the box dimensions are not well suited

for shear simulations. As polymers elongate in the flow direction, the simulation box has to be chosen large enough, so that two completely stretched rings fit into a single box, making sure a polymer pair does not interact with itself. Therefore, we repeated the equilibrium simulation setup for a box of $M = 320$ polymers, each of $N = 200$ monomers at a monomer density of $\rho = 0.85\sigma^{-3}$ in a smaller cubic simulation box and confirmed that the system was in equilibrium. We then replicated this smaller box five times along the x-direction to create a cuboid with $M = 1600$ polymers. After confirming the system reached equilibrium again, we used this configuration as the initial state for all shear simulations.
We carried out seven shear simulations, each corresponding to a different shear rate, ranging from Wi = 0.85 to Wi = 30.0. The NEMD simulations were performed in LAMMPS [31] using the atomistic SLLOD equations of motion, in combination with a Nosé-Hoover thermostat to maintain the correct temperature throughout the simulation. The potential parameters are identical to the equilibrium simulation. The explicit implementation of the atomistic SLLOD equations of motion are provided in Appendix A.0.2.

5.1.2. Confirming Steady State Shear Flow

Before performing the deadlock detection algorithm, we confirm that the system experiences steady-state shear flow, by confirming the linear nature of the velocity profile v_x along the flow gradient direction y. For all analyzed steady-state simulations, the slopes were perfectly linear with a standard deviation on the order of 10^{-5}. However, since the SLLOD algorithm enforces the velocity profile, this check is not sufficient to confirm the correct behavior of the simulation.
To further verify the systems behavior, we examine the viscosity, η, as a function of the Weissenberg number (Wi), for the seven shear simulations. The Weissenberg number Wi is a dimensionless number that characterizes the relative importance of elastic forces compared to viscous forces in a flowing fluid. In the context of shear, it is defined as the product of the characteristic relaxation time of the polymer in equilibrium, τ_{relax}, and the shear rate $\dot{\gamma}$, giving insight into how the material responds to the applied shear flow.

$$Wi = \tau_{relax} \cdot \dot{\gamma} \tag{5.1}$$

The viscosity data, shown in Figure 5.1, exhibits shear-thinning behavior, which can be described by the following expression

$$\eta(\mathrm{Wi}) = \frac{\eta_0}{(1 + \mathrm{Wi})^{\alpha}}, \tag{5.2}$$

where η_0 is the zero-shear viscosity, and α is the shear thinning exponent. For our simulations, we obtained a shear thinning exponent of $\alpha = 0.6$, which agrees with literature values [4] for both experiments ($\alpha = 0.57 \pm 0.08$) and simulations ($\alpha = 0.56 \pm 0.02$). The theoretical fit shown in Figure 5.1 is obtained through equation 5.2 with α=0.6.

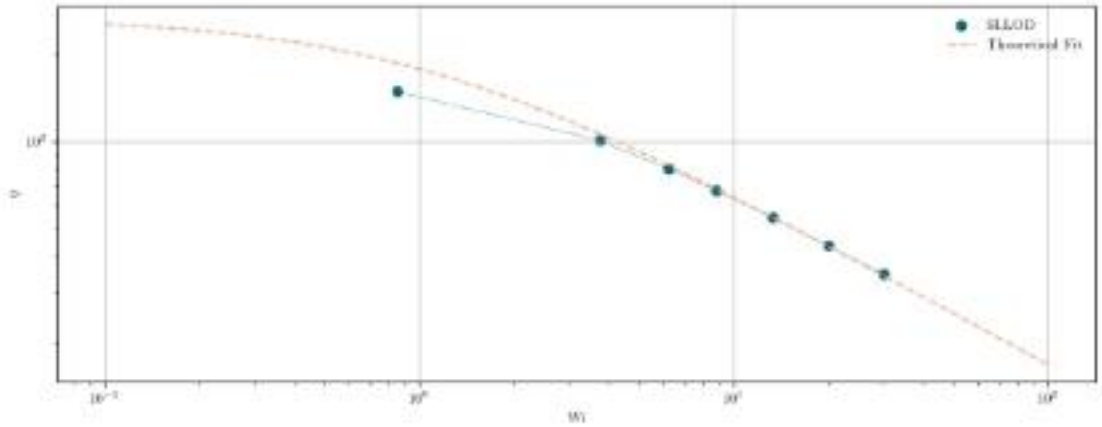

Figure 5.1.: Viscosity versus Weissenberg Number in log-log scale. The theoretical fit is equation 5.2 with fit parameter $\alpha = 0.6$.

The properties of all seven simulations are summarized in Table 5.1, where τ_D is the diffusion time in equilibrium, $\tau_{sr} = 1/\dot{\gamma}$ is a characteristic time-scale for shear simulation, where $\dot{\gamma}$ is the corresponding shear rate and η is the viscosity of the material in the steady-state regime.

Time-Series Abbreviation	Wi	Shear rate $\dot{\gamma}$	$\tau_{sr}[\tau]$	Viscosity η
S_1	0.85	$3.01\ 10^{-5}$	33176.47	148.78
S_2	3.75	$1.33\ 10^{-4}$	7520.00	100.86
S_3	6.2	$2.20\ 10^{-4}$	4548.39	80.48
S_4	8.8	$3.12\ 10^{-4}$	3204.55	67.77
S_5	13.3	$4.72\ 10^{-4}$	2120.30	54.58
S_6	20.0	$7.09\ 10^{-4}$	1410.00	43.35
S_7	30.0	$1.06\ 10^{-3}$	940.00	34.87

Table 5.1.: Overview of all seven steady-state shear simulations S_1 through S_7.

5.2. Deadlock Detection Series

Once the correct behavior of the shear simulations is confirmed, we selected a series of snapshots of the steady-state regime of two distinct shear rates, respectively, Wi = 8.8 and 30.0. For each simulation, we selected 30 snapshots and applied them to the full deadlock detection algorithm. As the deadlock detection algorithm is computationally expensive, we executed the deadlock detection on a scientific cluster. Unfortunately, the cluster had some storage issues, and not all conformations could be successfully processed. For each timestep, this corresponds to about 150 pairs, making up roughly 0.05% of all

pairs, which were excluded from the results. As the encountered error affects all pairs equally, deadlocked or not, we suspect that the error is homogeneously distributed across all degrees of deadlocking and does not significantly alter the distributions. We present the results under the assumption, that the error is indeed uniformly distributed and that the small percentage of pairs that could not be processed does not significantly change any distributions.
The analyzed time-series are summarized in Table 5.2.

Time-Series Abbreviation	Wi	Number of Snapshots n_s	Separating Timesteps Δt $[\tau]$	Total Time-Range t_{tot} $[\tau]$
TS_4	8.8	30	3000=$0.94\tau_{sr}$=$0.11\tau_D$	90000=$28.05\tau_{sr}$=$3.19\ \tau_D$
TS_7	30.0	30	1000=$0.94\tau_{sr}$=$0.033\tau_D$	129600=$28.2\tau_{sr}$=$1\tau_D$

Table 5.2.: Analyzed Time-Series of Deadlocks in steady-state shear flows.

5.3. Results and Interpretation

In this section, we investigate the properties of deadlocks in ring polymer melts under steady-state shear conditions. Specifically, we examine two shear rates, Wi = 8.8 and Wi = 30.0, to explore how deadlocks evolve under shear. For each shear rate, we analyze the overall population of deadlocked pairs, followed by an investigation into the persistence of these deadlocks and an analysis of their static properties. All distributions are presented as the overall distribution of all deadlocked pairs with $\xi > 0$, as well as group-dependent distributions, as defined by equation 3.22. These group-dependent distributions include Group 0, which serves as a reference and represents linearly non-separable pairs that do not exhibit any degree of deadlocking.
While these two shear rates already provide insights into the behavior of deadlocks under shear, they are not sufficient to fully capture the influence of shear forces on deadlocks. Future work will involve sampling all seven shear rates to obtain a more comprehensive understanding of deadlock dynamics in shear. This will be further discussed in the Outlook section of the thesis.

5.3.1. Deadlock Formation in Shear

In this section, we present the composition of deadlocks in ring polymer melts under steady-state shear conditions for two shear rates: Wi = 8.8 and Wi = 30.0. Specifically, we focus on the total number of deadlocks in each group as a function of time and the distribution of the degree of deadlocking, averaged over time.
At Wi = 8.8, we observe a significant increase in the total number of deadlocked pairs with $\xi > 0$, more than twice as many compared to the equilibrium state of the system, as shown in Figure 5.2. The population in Group 1, which corresponds to deadlocked pairs

with low degrees of deadlocking, remains comparable to that in equilibrium. The number of deadlocks in Group 1 fluctuates around a mean value of $N_{0<\xi\leq 0.1} \sim 610$ deadlocks, with fluctuations similar in magnitude to those observed in equilibrium.
However, the populations in Groups 2 and 3 show clear differences when compared to their equilibrium counterparts. First, the absolute number of pairs in these groups has increased drastically, with Group 3 representing more than 15 times the number of deadlocks observed in equilibrium. Interestingly, the population of Group 3 exceeds that of Group 2, whereas, in equilibrium, Group 2 had a higher population than Group 3. This might be an indication for tight deadlocked structures, where the deadlocked portion of the rings is sufficiently localized. The fluctuations in Group 2 and Group 3 are notably more pronounced than those of Group 1 and occur in a synchronized manner, suggesting an underlying physical cause. These periodic fluctuations lead us to suspect a connection to the tumbling dynamics of the melt, which could influence the formation and disappearance of deadlocks in shear. Furthermore, the synchronization of fluctuations in Group 2 and 3 point to the possibility that, under shear, the deadlocks can be classified into just two regimes: a low-deadlocking regime (Group 1) and a high-deadlocking regime (comprising Groups 2 and 3), in contrast to the three distinct deadlock classes observed in equilibrium.

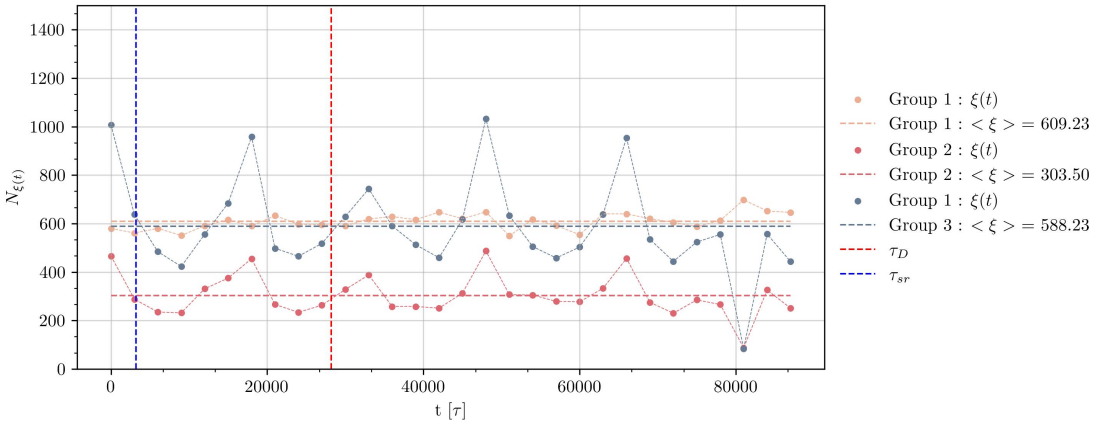

Figure 5.2.: Number of deadlocks found in each group of time-series TS_4 for Wi = 8.8.

At a higher shear rate of Wi = 30.0, the number of deadlocks with $\xi > 0$ has increased even further, summing up to nearly 2000 pairs per timestep - more than three times the number seen in equilibrium, as shown in Figure 5.3. The behavior of Groups 2 and 3 at Wi = 30.0 mirrors that observed at Wi = 8.8, with extremely similar mean values, fluctuations of comparable magnitude and synchronized periodicity. Notably, the periodicity of these fluctuations, measured in units of the inverse shear rate τ_{sr}, is identical to that observed at Wi = 8.8, indicating that the underlying physical processes governing the deadlock dynamics are consistent across these two shear rates.

In contrast to Group 2 and 3, the population of Group 1 has doubled relative to its value at Wi = 8.8. However, while Group 1 shows similar characteristic fluctuations around the mean value, these fluctuations are not influenced by the same periodicity as those in Groups 2 and 3.

For both analyzed shear rates, the substantial increase in the number of representatives in Group 3, along with the corresponding rise in Group 2, and the lack of a significant decrease in Group 1 leads to the following interpretation: on time scales of the order of τ_{sr} (which is comparable to the timestep separating the analyzed configurations), ring polymer pairs transition from a non-deadlocked state to a fully deadlocked state and vice versa. This suggests that the shear forces drive a dynamic shift in the population of deadlocked pairs, with these transitions occurring rapidly within timescales comparable to τ_{sr}. In absolute time units, the formation and disappearance of deadlocks has a higher frequency for Wi = 30.0 compared to Wi = 8.8, indicating a faster transition from non-deadlocked to fully deadlocked states.

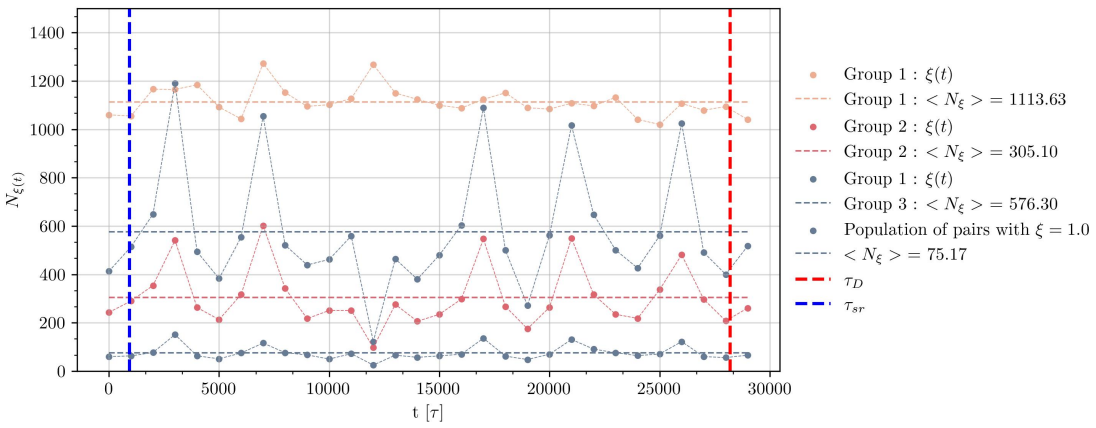

Figure 5.3.: Number of deadlocks found in each group of time-series TS_7 for Wi = 30.0.

We next investigate the distribution of the degree of deadlocking, averaged over all 30 analyzed timesteps, for the shear systems at Wi = 8.8 and Wi = 30.0, respectively. The results are shown in Figures 5.4 and 5.5, with the envelope of the equilibrium distribution included for comparison.
At Wi = 8.8, the distribution of the degree of deadlocking initially resembles the equilibrium distribution, with no significant differences observed for values of ξ up to 0.2. However, for higher values of ξ, the shear distribution begins to deviate from equilibrium. While the equilibrium distribution shows a strong decline in the population of deadlocked pairs as ξ increases, the shear distribution at Wi = 8.8 exhibits a more homogeneous population with a higher fraction of deadlocked pairs having ξ values greater than 0.2. Notably, the population of pairs with $\xi = 1$ is particularly large, which may indicate

configurations where the deadlock is "pulled tight" by the shear flow. In these cases, most of the cutting points for the path reconnections are outside the deadlocked region, entrapping the deadlock by our reconnection and resulting in an increased degree of deadlocking. While this interpretation remains speculative, further investigation is needed to clarify the exact dynamics responsible for this behavior.

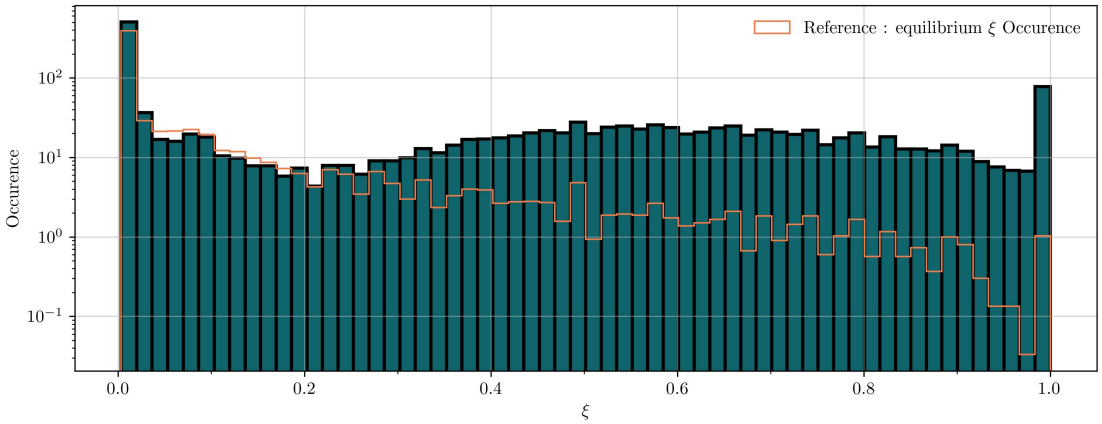

Figure 5.4.: Distribution of the time-averages occurrence of the degree of deadlocking (ξ) for time-series TS_4, corresponding to Wi = 8.8.

For the higher shear rate of Wi = 30.0, the distribution of the degree of deadlocking follows a similar trend as observed at Wi = 8.8, as shown in Figure . The general behavior of the ξ-distribution at Wi = 30.0 mirrors that of Wi = 8.8, suggesting that the overall composition of deadlocks is nearly identical at both shear rates.
As shown in Figure 5.5, the distribution of the degree of deadlocking at higher shear rates (Wi = 30.0) mirrors that of Wi = 8.8, suggesting that the overall composition of deadlocks is nearly identical at both analyzed shear rates. However, the increased population of Group 1 observed in Figure 5.3 corresponds to the appearance of deadlocks with extremely small ξ values, which is reflected in the increase in the first two bins of the histogram.

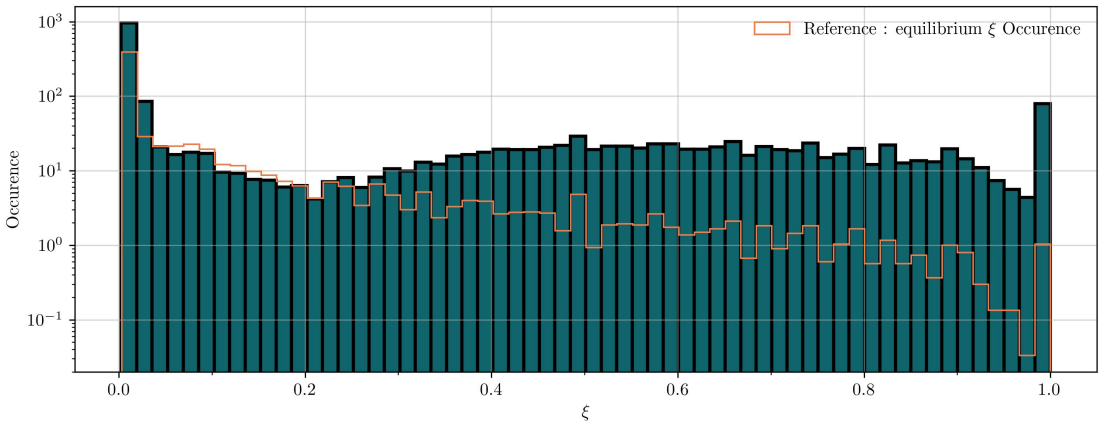

Figure 5.5.: Distribution of the time-averages occurrence of the degree of deadlocking (ξ) for time-series TS_7, corresponding to Wi = 30.0.

5.3.2. Deadlock Persistence in Shear

In this section, we investigate the persistence, or survival time, of deadlocked pairs under shear forces at the two shear rates Wi = 8.8 and Wi = 30.0. The primary goal is to understand how stable the deadlock configurations are in shear systems and to identify characteristic timescales over which the deadlocks remain stable before becoming disentangled. We explore several quantities related to the persistence of deadlocks, including the longest survival time, t_s, and the autocorrelation function, which measures the likelihood that a polymer pair stays deadlocked over subsequent timesteps.
The first property we analyze is the longest survival time t_s of the deadlocks, For details on how we obtained the distribution, please refer to the equilibrium chapter, where the procedure is explained.

The distribution of t_s for Wi = 8.8 is shown in Figure 5.6. This distribution reveals that most deadlocks disentangle within a timescale comparable to the inverse shear rate τ_{sr}, corresponding to the first bin in the distribution. While the majority of pairs disentangle rapidly, some pairs persist for longer times, up to $3\tau_D$.
In equilibrium, the distribution of t_s nicely decomposes into three distinct regimes: short lived deadlocks corresponding to Group 1, long-lived deadlocks corresponding to Group 3 and intermediate behavior for Group 2. In contrast, at Wi = 8.8, the peak of each distribution shifts to the left, indicating that most pairs, regardless of their group membership, disentangle quickly. Similar to the previous section, the distributions for Groups 2 and 3 are nearly indistinguishable, reinforcing the observation that their behaviors are quite similar under shear. Notably, the strong correlation between the degree of deadlocking and the longest survival time observed in equilibrium is absent in shear. However, for Group 1, pairs with a low degree of deadlocking disentangle within a timescale comparable to the diffusion time in equilibrium, while pairs in Groups 2 and 3

can persist for significantly longer periods, exceeding our observation window of $3\tau_D$. We conclude, that while the degree of deadlocking does not correlate as strongly with the longest survival time as in equilibrium, it is still a reasonable measure to detect short lived deadlocked structures, where pairs exhibiting a higher value of ξ have an increased chance for long survival, though not as meta-stable than in equilibrium.

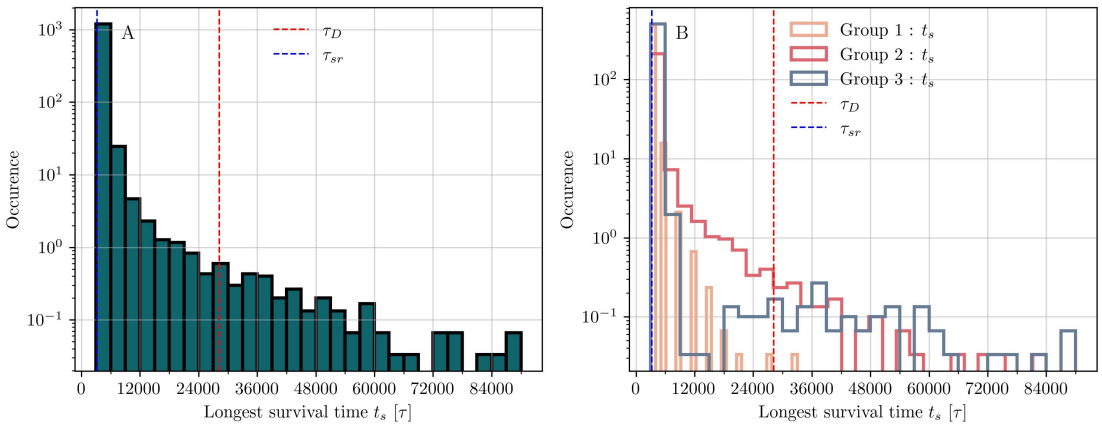

Figure 5.6.: Distribution of the longest survival time $t_s$of deadlocks in time-series TS_4 for Wi = 8.8. Panel A shown the overall distribution of all pairs with $\xi > 0$, whereas panel B shows the group-dependent data. The grouping in panel B is based on the mean degree of deadlocking over the longest sequence of consecutive deadlocked states.

The distribution of t_s at Wi = 30.0 is shown in Figure 5.7. It is important to note that the total time span over which we sampled the deadlocked configurations is different for the two shear rates. Despite this, the same qualitative behavior is observed at both shear rates. Independent of their group membership, most pairs disentangle within the fist observed timestep, highlighting the rapid disentangling mechanism for deadlocks in shear. Similar to Wi = 8.8, the distribution of Group 1 at Wi = 30.0 decays exponentially, with no pair surviving beyond 12000τ, which is approximately $0.5\tau_D$. Interestingly, in units of τ_{sr}, the timescales sufficient to disentangle all pairs in Group 1 is comparable to that of Group 1 at Wi = 30.0. While the majority of pairs in Groups 2 and 3 also disentangle quickly, a small fraction persists for extended periods, lasting for more than one diffusion time.

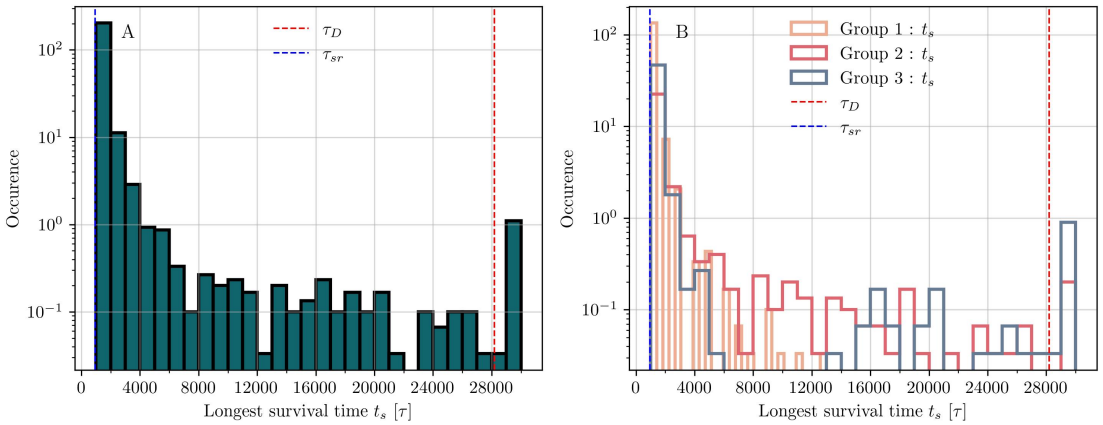

Figure 5.7.: Distribution of the longest survival time t_s of deadlocks in time-series TS_7 for Wi = 30.0. Panel A shows the overall distribution of all pairs with $\xi > 0$, whereas panel B shows the group-dependent data. The grouping in panel B is based on the mean degree of deadlocking over the longest sequence of consecutive deadlocked states.

Next, we investigate the likelihood that a polymer pair remains deadlocked over subsequent timesteps by analyzing the autocorrelation function $C(t)$ of the binary sequence representing the deadlocked/disentangled state of a polymer pair over time. For a detailed description of how the autocorrelation function was calculated, please refer to the equilibrium chapter, where we outline the procedure for this analysis.
The autocorrelation function for deadlocks at Wi = 8.8 is shown in Figure 5.8. The shape of $C(t)$ confirms the behavior observed in the distribution of the longest survival time: most pairs disentangle quickly, as evidenced by the sharp drop in $C(t)$ after the first timestep. Following this initial rapid decay, the autocorrelation function continues to decrease more gradually, highlighting the persistence of some deadlocked pairs. This gradual decay suggests that while many pairs disentangle at timescales of τ_{sr}, a smaller fraction of pairs remain deadlocked for extended periods, contributing to the slower decrease of the autocorrelation function.

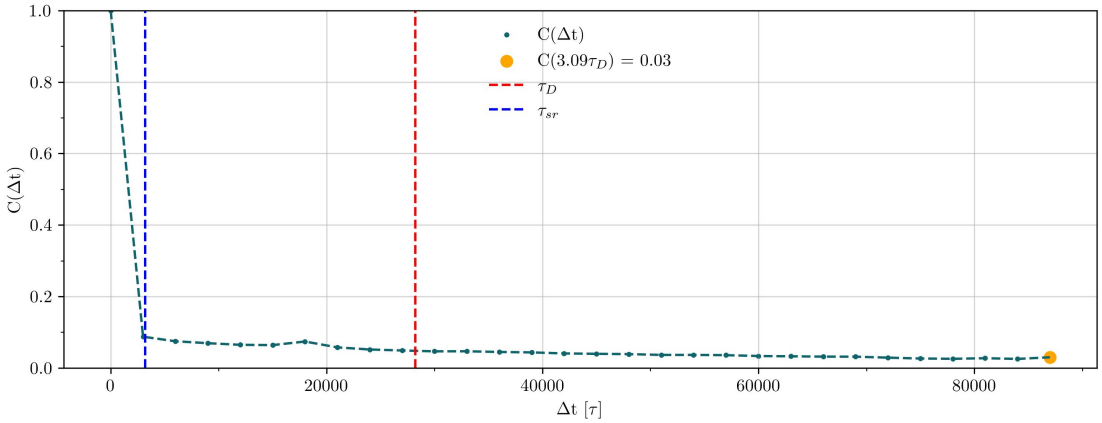

Figure 5.8.: Autocorrelation function of deadlocked pairs as a measure of likelihood that a polymer pair remains deadlocked over time, obtained through time-series TS_4 for Wi=8.8.

The autocorrelation function for deadlocks at Wi = 30.0 is shown in Figure 5.9. Similar to the observations at Wi = 8.8, we see a sharp initial decay of $C(t)$, followed by a more gradual decrease. This indicates that most pairs disentangle quickly at this higher shear rate as well, but a portion of deadlocked pairs also persists over longer timescales.

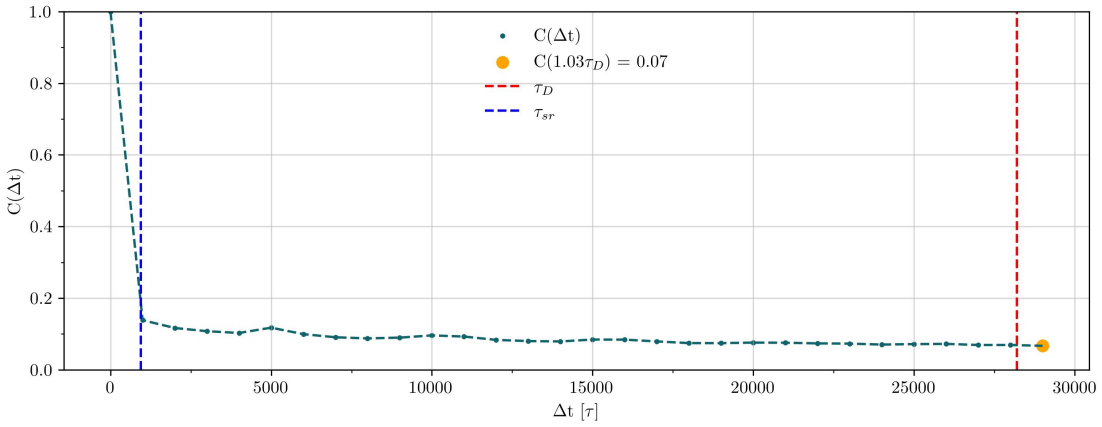

Figure 5.9.: Autocorrelation function of deadlocked pairs as a measure of likelihood that a polymer pair remains deadlocked over time.

We next investigate the group-dependent autocorrelation functions to assess the stability of polymer pairs within each group. Given that a pair is deadlocked in a particular group at time t, the autocorrelation functions reveal the probability that this pair will remain deadlocked in the same group after a later time $t + \Delta t$. For readers interested in how the

autocorrelation functions were obtained, we refer to the equilibrium chapter, where the procedure is detailed.
The group-dependent autocorrelation functions for Wi = 8.8 are shown in Figure 5.10 for Group 1 (panel A), Group 2 (panel B) and Group 3 (panel C), respectively. All three autocorrelation functions exhibit a rapid decrease during the first timestep, indicating that all pairs undergo quick conformational changes that influence their degree of deadlocking. Group 1 shows the fastest decay, with polymer pairs changing their group membership almost immediately. The autocorrelation function for Group 2 drops to a value of 0.13 after the first timestep, then decreases at a slower rate, suggesting that some pairs in Group 2 remain in Group 2 for longer durations before transitioning. For both, Group 1 and Group 2, the observation window was sufficient for all pairs to change their group membership at least once. In contrast, the autocorrelation function for Group 3 drops to ~ 0.06 after the first timestep, highlighting that also polymer pairs in this group change group membership rapidly, but the extremely slow decay after suggests, that those pairs that persist for τ_{sr}, remain highly deadlocked for extended periods.
When comparing the behavior of these autocorrelation function to those of the equilibrium state of the system, the stability of deadlocks under shear is less pronounced. In shear, deadlocked pairs change group membership more rapidly than in equilibrium, indicating that shear forces disrupt the long-term stability of deadlocked structures.

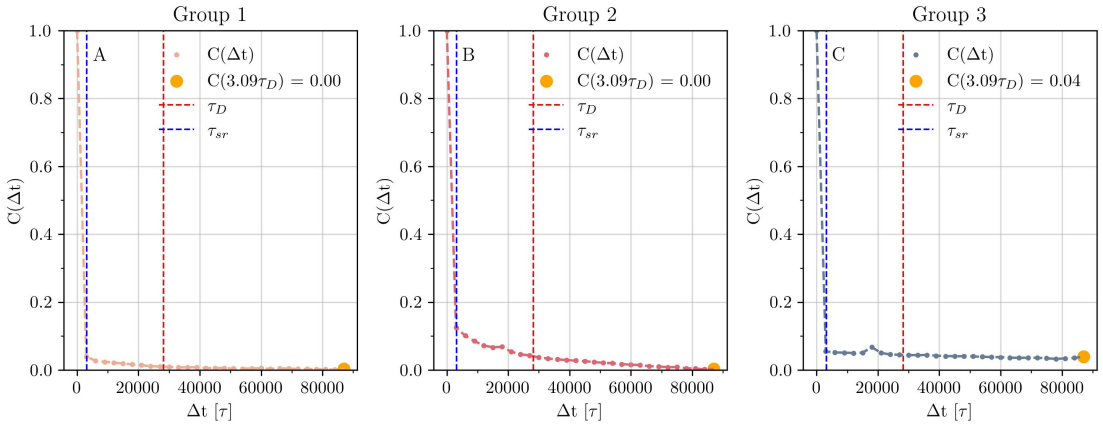

Figure 5.10.: Autocorrelation function of deadlocked pairs remaining in Group 1 (panel A), Group 2 (panel B) and Group 3 (panel C), respectively. The analysis is based on time-series TS_4 for a shear simulation at Wi = 8.8.

The group-dependent autocorrelation functions for Wi = 30.0, shown in Figure 5.11, reveal similar behavior to those at Wi = 8.8. In contrast to the lower shear rate, $C(t)$ for Group 3 drops only to ~ 0.18 during the first timestep and exhibits an extremely slow decay thereafter, suggesting that those pairs that survive a duration of τ_{sr}, those pairs are likely to stay highly deadlocked for extended periods.

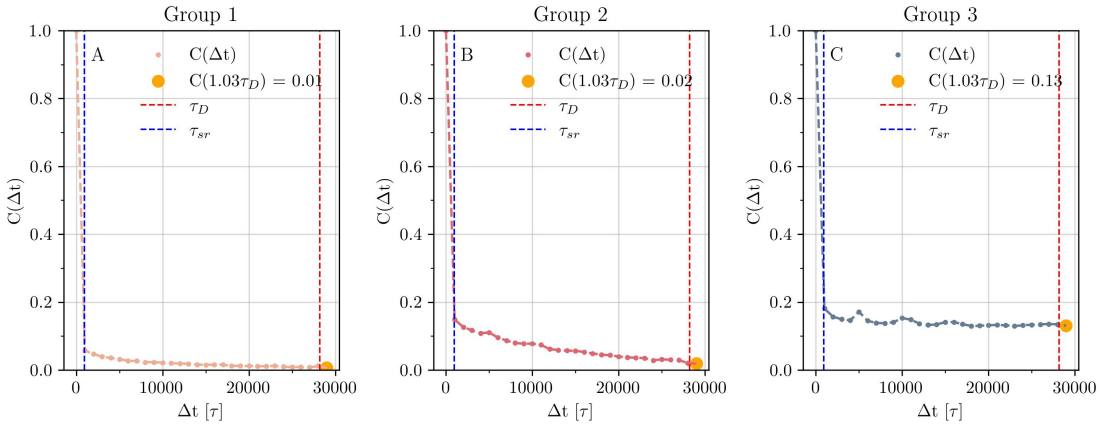

Figure 5.11.: Autocorrelation function of deadlocked pairs remaining in Group 1 (panel A), Group 2 (panel B) and Group 3 (panel C), respectively. The analysis is based on time-series TS_7 for a shear simulation at Wi = 30.0.

5.3.3. Static Properties of Deadlocks in Shear

In this section, we investigate the static properties of deadlocked pairs under shear flows at two different shear rates: Wi = 8.8 and Wi = 30.0. We analyze a range of distributions to explore the structure of deadlocked pairs, including the radius of gyration of the polymer pair, the eigenvalues of the gyration tensor (which measure the pair's anisotropy), the center of mass distance between deadlocked pairs, and the maximal intermonomer distance. Additionally, we examine the distribution of the overlapping volume between the two rings involved in a deadlock and characterize the deadlocked regions by the radius of gyration of the overlapping monomers as well as the distribution of the eigenvalues of the gyration tensor for monomers within the intersecting region. The goal is to understand whether the two deadlocked regimes ($\xi < 0.2$ and $\xi > 0.2$) exhibit different structural properties. Furthermore, we investigate the influence of shear forces on the conformations of deadlocked pairs by comparing the static properties of deadlocked pairs at Wi = 8.8 to the properties of deadlocked pairs at Wi = 30.0.

Gyration Analysis

To gain insight into the conformational properties of deadlocked pairs under shear, we examine the distribution of the radius of gyration (R_g) of the polymer pair as a measure of the average extension, as well as the eigenvalues of the gyration tensor to quantify the anisotropy of the pair's conformation.
The R_g distribution for deadlocked pairs at Wi = 8.8 is shown in Figure 5.12. The distribution reveals, that the overall compactness of the polymer pairs are similar for Group 1 and Group 3. The distribution for Group 0 shows a large tail towards large R_g

values, indicating that some pairs in Group 0 are extremely extended in space. Group 2, in contrast, shows a smaller overall extension, which might be a an indication for their less extended conformations.
Compared to the equilibrium state of the system, the values of R_g are higher under shear. This is due to the shear flow aligning the polymers in the flow direction, which results in more elongated conformations, increasing their average extension.

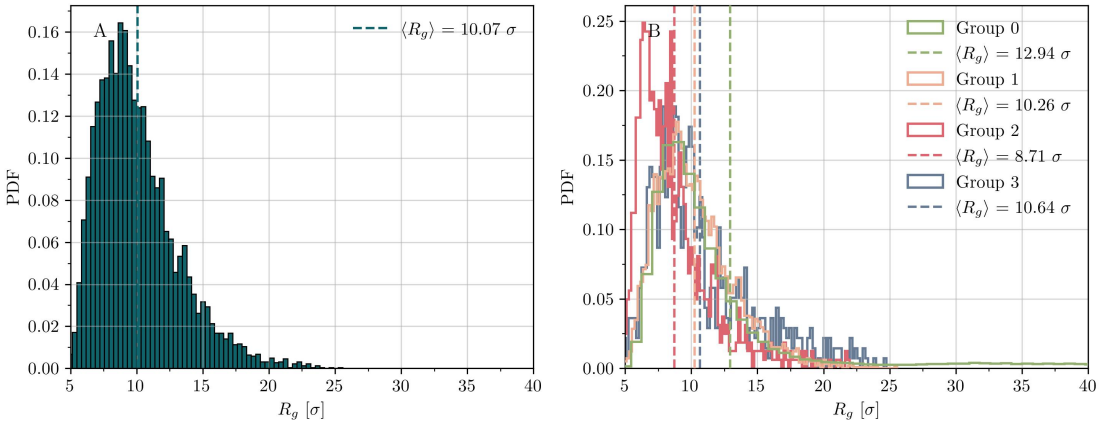

Figure 5.12.: Distribution of the radius of gyration, calculated from time-series TS_4 for a shear simulation with Wi = 8.8. Panel A shows the R_g distribution for all pairs with $\xi > 0$ and panel B shows the group-dependent distributions.

For Wi = 30.0, the R_g distribution is shown in Figure 5.13. As the shear rate increases, polymers become even more stretched, leading to generally larger values of R_g. The behavior of deadlocked pairs across different groups shows that representatives of Group 1 are slightly more extended, but otherwise shows little variations between the different groups.

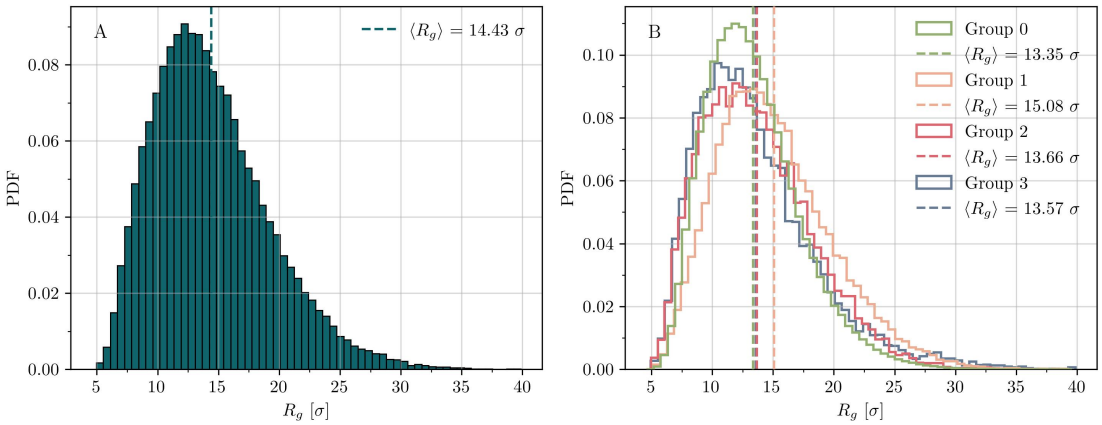

Figure 5.13.: Distribution of the radius of gyration, calculated from time-series TS_7 for a shear simulation with Wi = 30.0. Panel A shows the R_g distribution for all pairs with $\xi > 0$ and panel B shows the group-dependent distributions.

We examine the eigenvalues of the gyration tensor, which provide a measure of the anisotropy of the polymer pair. The eigenvalues, rescaled by their corresponding R_g, are shown in Figure 5.14 for Wi = 8.8 and in Figure 5.15 for Wi = 30.0. As expected under steady-state shear conditions, the conformations of deadlocked pairs are stretched along the first principal axis of the gyration tensor, while the other two eigenvalues remain relatively small. This behavior is more pronounced at higher shear rates, with Wi = 30.0 showing stronger stretching of conformations. Across different groups, the behavior largely coincides for both shear rates.

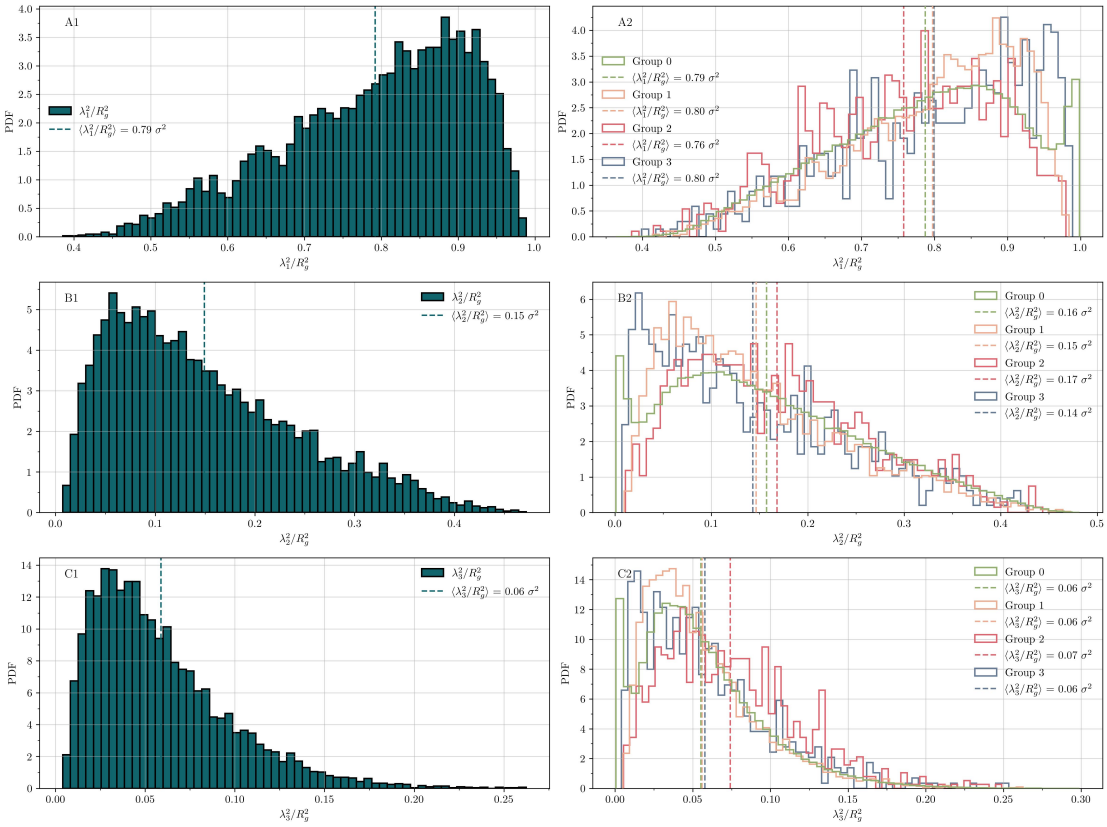

Figure 5.14.: Distribution of the eigenvalues of the gyration tensor of polymer pairs, calculated from time-series TS_4 of a shear simulation with Wi = 8.8. Panels on the left show the distribution of eigenvalues for all deadlocked pairs ($\xi > 0$), whereas panels on the left show the group-dependent eigenvalue distributions.

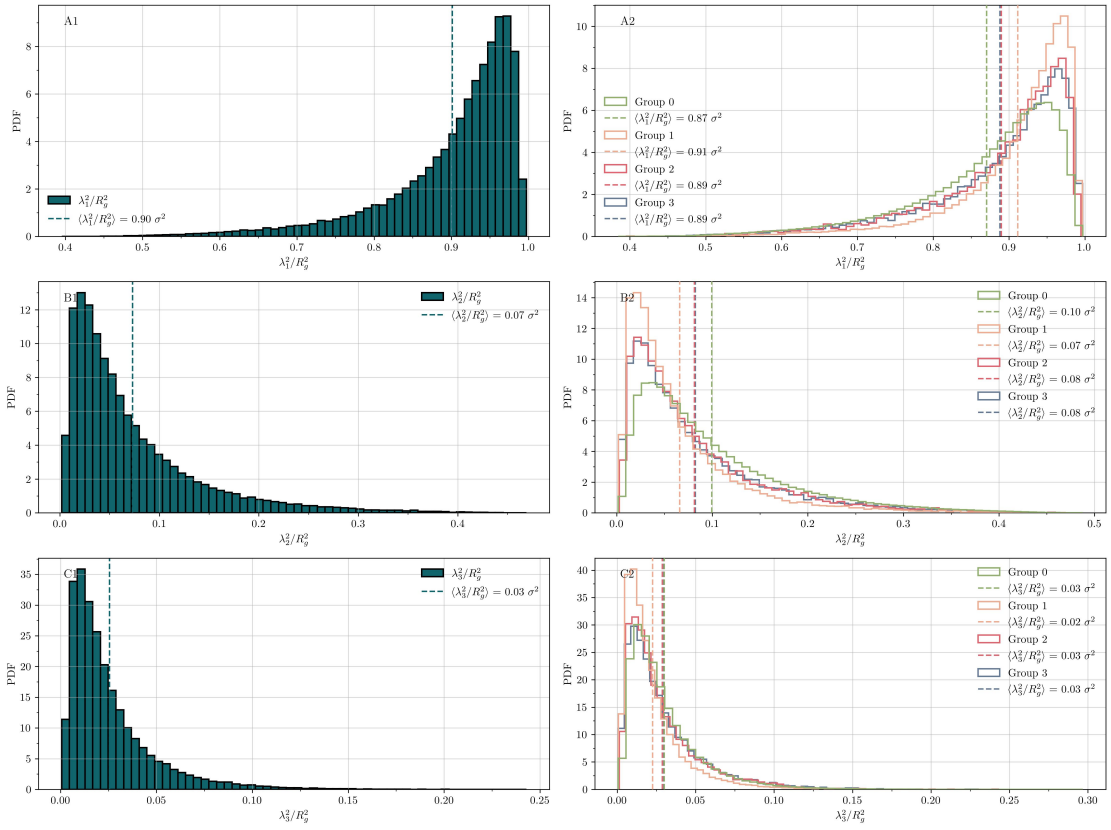

Figure 5.15.: Distribution of the eigenvalues of the gyration tensor of polymer pairs, calculated from time-series TS_7 of a shear simulation with Wi = 30.0. Panels on the left showsthe distribution of eigenvalues for all deadlocked pairs ($\xi > 0$), whereas panels on the left show the group-dependent eigenvalue distributions.

Center of Mass Distance

We next investigate the spatial relationship between the center of masses of deadlocked polymer pairs. By examining the distance between the centers of mass (d_C), we aim to understand how the degree of deadlocking influences the relative positioning of the two rings and how this composition changes for different shear rates.
The distribution of the rescaled center of mass distances for Wi = 8.8 is shown in Figure 5.16. The distribution reveals that, relative to their average extension, pairs in Group 2 tend to be close together in space, while some pairs in Group 0 are extremely separated. The bimodal nature of Group 0, especially the peak at high center of mass distances, remains an open question.

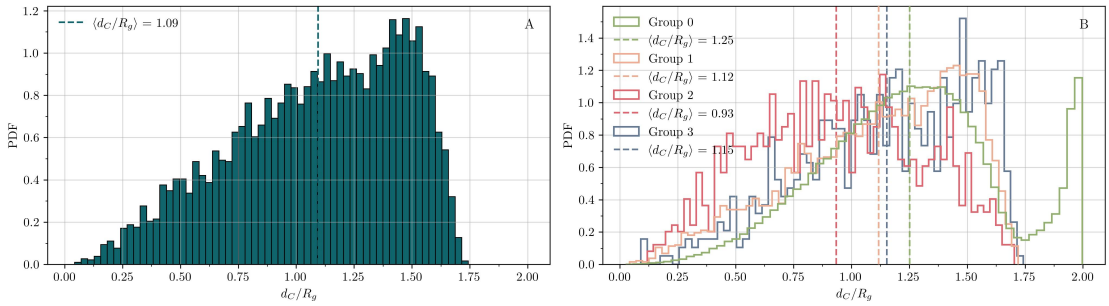

Figure 5.16.: Distribution of the center of mass distance between two linearly non-separable polymer pairs, calculated from time-series TS_4 of a shear simulation with Wi = 8.8. Panel A shows the overall distribution for all pairs with $\xi > 0$ and panel B displays the group-dependent d_C distributions.

Figure 5.17 shows the rescaled center of mass distance between two deadlocked rings in shear at Wi = 30.0. At the higher shear rate, the deviations between groups become less pronounced, with relatively similar mean values observed across all groups.

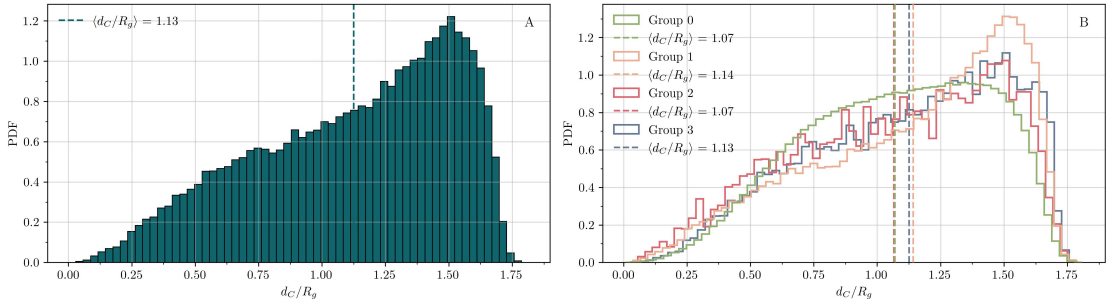

Figure 5.17.: Distribution of the center of mass distance between two linearly non-separable polymer pairs, calculated from time-series TS_7 of a shear simulation with Wi = 30.0. Panel A shows the overall distribution for all pairs with $\xi > 0$ and panel B displays the group-dependent d_C distributions.

Maximum Intermonomer Distance

We next investigate if the maximal intermonomer distance (d_m) between any two monomers in the polymer pair is influenced by the degree of deadlocking and whether there are any significant changes for different shear rates.
The rescaled maximal intermonomer distance for Wi = 8.8 is shown in Figure 5.18. The distribution suggests that the maximal intermonomer distance for deadlocked pairs is not

strongly influenced by the degree of deadlocking, except for the bimodal nature observed in Group 0, the cause of which remains unclear.

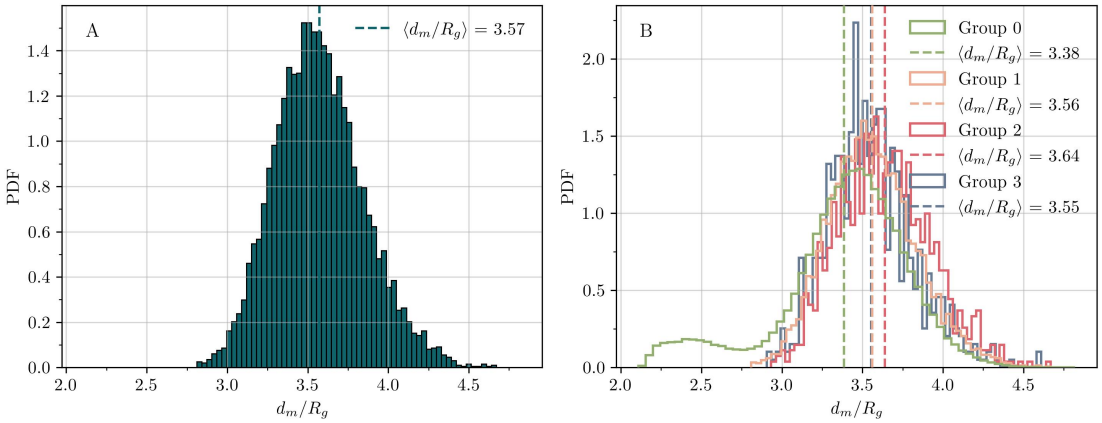

Figure 5.18.: Distribution of the maximal intermonomer distance d_m between any two monomers of a pair, normalized by the corresponding gyration radius R_g. Panel A shows the overall distribution for all deadlocked pairs with $\xi > 0$, whereas panel B shows the group-dependent distributions. The data was obtained through time-series TS_4 for a shear simulation with Wi = 8.8.

The d_m distribution for Wi = 30.0 is shown in figure 5.19. At this higher shear rate, we find that the deviations between groups are even smaller than at Wi = 8.8, suggesting that shear forces have a more uniform effect on the intermonomer distances. Additionally, the absolute value of d_m/R_g has slightly increased compared to Wi = 8.8, which can be attributed to the greater elongation of the polymer chains under higher shear rates.

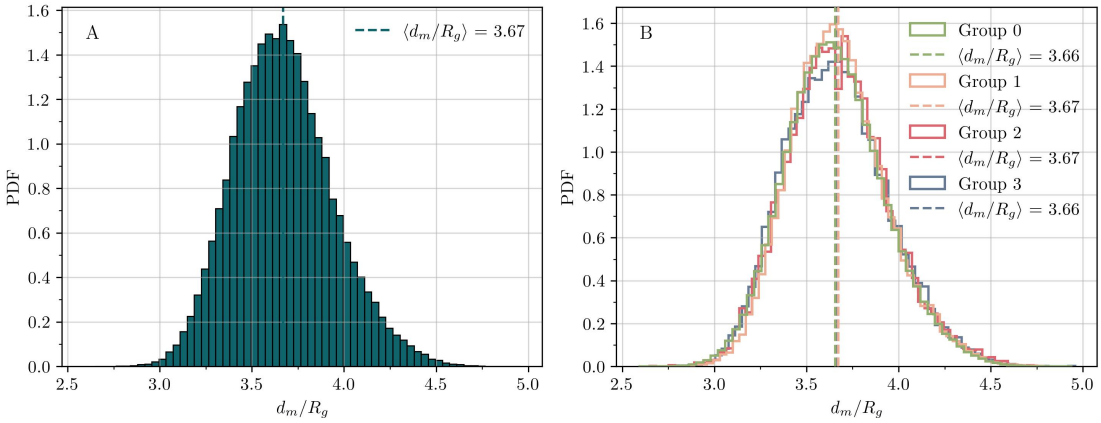

Figure 5.19.: Distribution of the maximal intermonomer distance d_m between any two monomers of a pair, normalized by the corresponding gyration radius R_g. Panel A shows the overall distribution for all deadlocked pairs with $\xi > 0$, whereas panel B shows the group-dependent distributions. The data was obtained through time-series TS_7 for a shear simulation with Wi = 30.0.

Overlapping Volume Analysis

We investigate the overlapping volume between the two rings involved in the deadlock. For computational details regarding how the overlapping volume was obtained, please refer to the corresponding explanation in the equilibrium section of this thesis.
The calculation of the overlapping monomers is computationally expensive, and as such, we performed this analysis only on a subset of the data, specifically selecting 3500 random samples from each group of both shear rates.
The results for the overlapping volume are shown in Figure 5.20 for Wi = 8.8 and in Figure 5.21 for Wi = 30.0. The distributions across all groups and both shear rates exhibit a similar trend; the overlapping volume function peaks at very low values, indicating that most pairs have limited overlap between the two rings. For Wi = 8.8, the mean overlapping volume is relatively small across all groups. In contrast, for Wi = 30.0, the mean value increases substantially, suggesting that the shear forces at higher rates lead to more significant overlap between the rings.

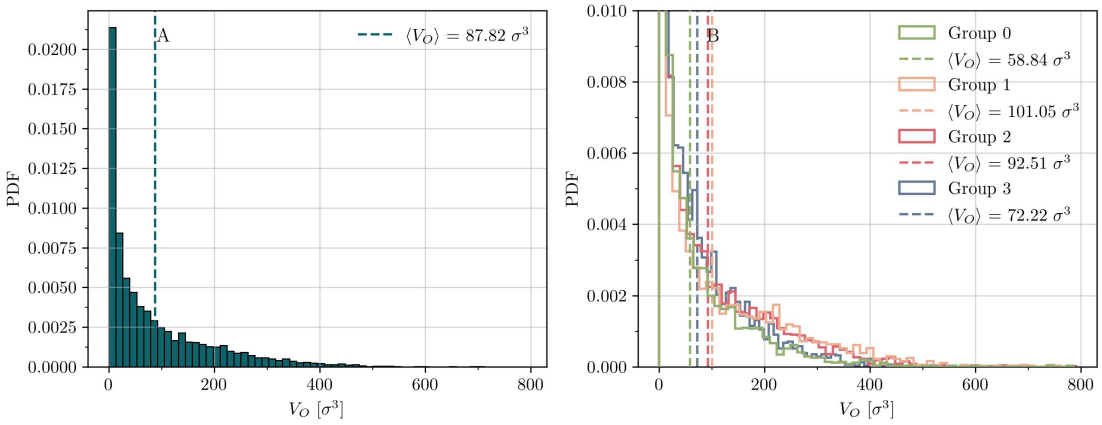

Figure 5.20.: Distribution of the overlapping volume between two non-linear separable polymer rings of time-series TS_4, corresponding to a shear simulation with Wi = 8.8. The data was generated by analyzing 3500 random samples each group, respectively. Panel A shows the overall distribution for all pairs with $\xi > 0$, while panel B shows the group-dependent distributions.

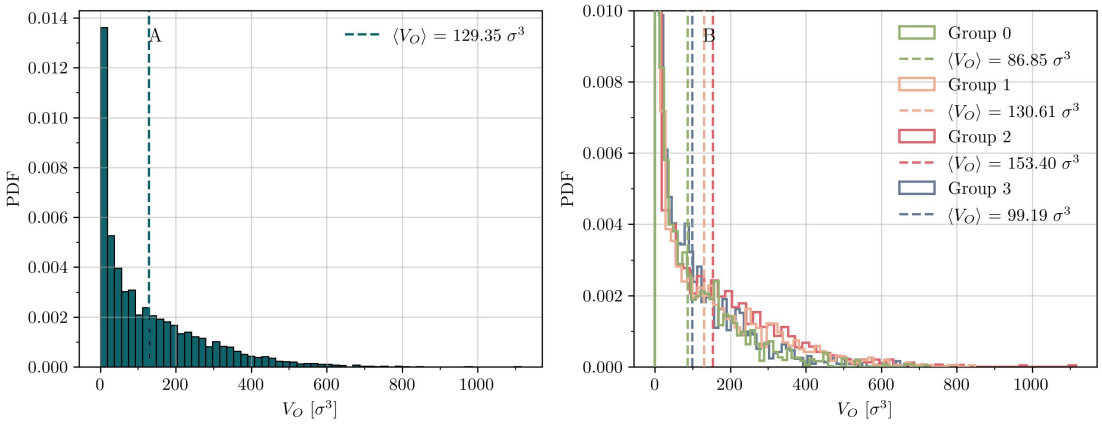

Figure 5.21.: Distribution of the overlapping volume between two non-linear separable polymer rings of time-series TS_7, corresponding to a shear simulation with Wi = 30.0. The data was generated by analyzing 3500 random samples each group, respectively. Panel A shows the overall distribution for all pairs with $\xi > 0$, while panel B shows the group-dependent distributions.

To further explore the properties of the deadlocked region, we calculate the radius of gyration for the monomers within the overlapping volume ($R_{g,O}$). The distribution for Wi = 8.8 is shown in Figure 5.22, and the distribution for Wi = 30.0 is shown in Figure

5.23. Both shear rates exhibit little dependence on the degree of deadlocking, with different groups following the same trends. For Wi = 8.8, the mean $R_{g,O}$ value is on the order of 3σ, indicating that the overlapping volume is likely confined to a single, continuous region where the deadlock is localized and pulled tight. In contrast, for Wi = 30.0, the mean $R_{g,O}$ values are on the order of 20σ, pointing to a much more extended region of overlap compared to Wi = 8.8. As the distribution for Wi = 30.0 is much broader compared to the distribution at Wi = 8.8, the deadlocked region for deadlocks under high shear rates show greater variation.

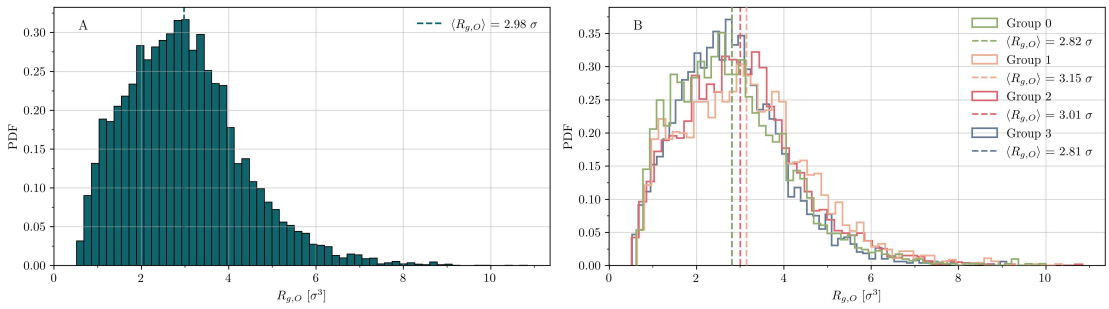

Figure 5.22.: R_g distribution of overlapping monomers between a polymer pair, calculated from the sub-set of 3500 random samples from each group, respectively, for time-series TS_4 of a shear simulation with Wi = 8.8. Panel A shows the overall distribution for all pairs with $\xi > 0$, while panel B shows the group-dependent distributions.

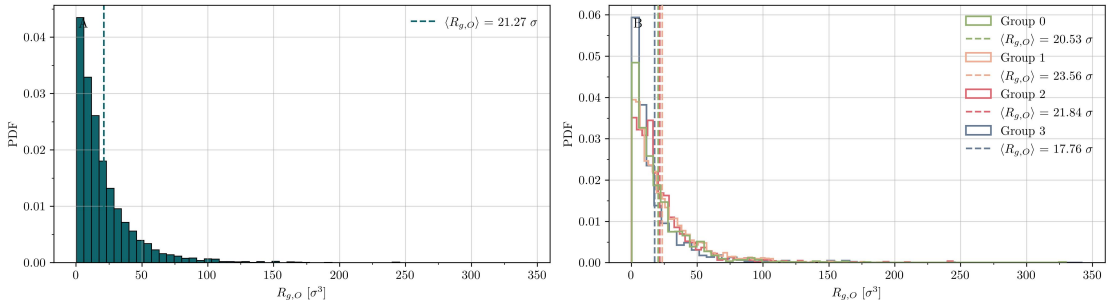

Figure 5.23.: R_g distribution of overlapping monomers between a polymer pair, calculated from the sub-set of 3500 random samples from each group, respectively, for time-series TS_7 of a shear simulation with Wi = 30.0. Panel A shows the overall distribution for all pairs with $\xi > 0$, while panel B shows the group-dependent distributions.

To further investigate the difference in behavior between the two shear rates, we computed

the distribution of the eigenvalues of the gyration tensor for the monomers in the overlapping region, rescaled by $R_{g,O}$. At Wi = 8.8 (Figure 5.25), the overlapping region shows a slightly elongated shape, suggesting a more compact deadlocked structure compared to Wi = 30.0, whose overlapping volume is more elongated (Figure 5.25). Moreover, the distribution of eigenvalues for Group 3 at Wi = 30.0 is more isotropic compared to Group 0 and Group 1.

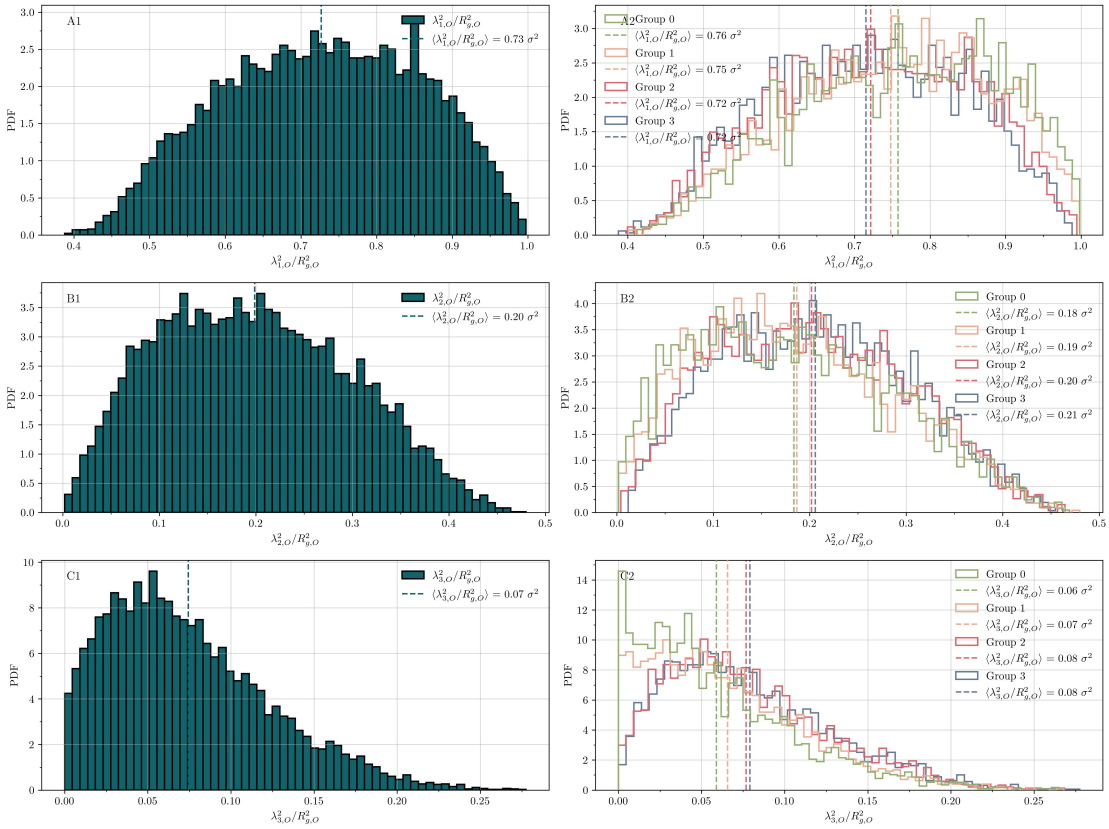

Figure 5.24.: Distributions of the eigenvalues of the gyration tensor for monomers within the intersecting region between the polymer pair, calculated from the sub-set of 3500 random samples from each group, respectively, for time-series TS_4 of a shear simulation with Wi = 8.8. Panel A shows the overall distribution for all pairs with $\xi > 0$, while panel B shows the group-dependent distributions.

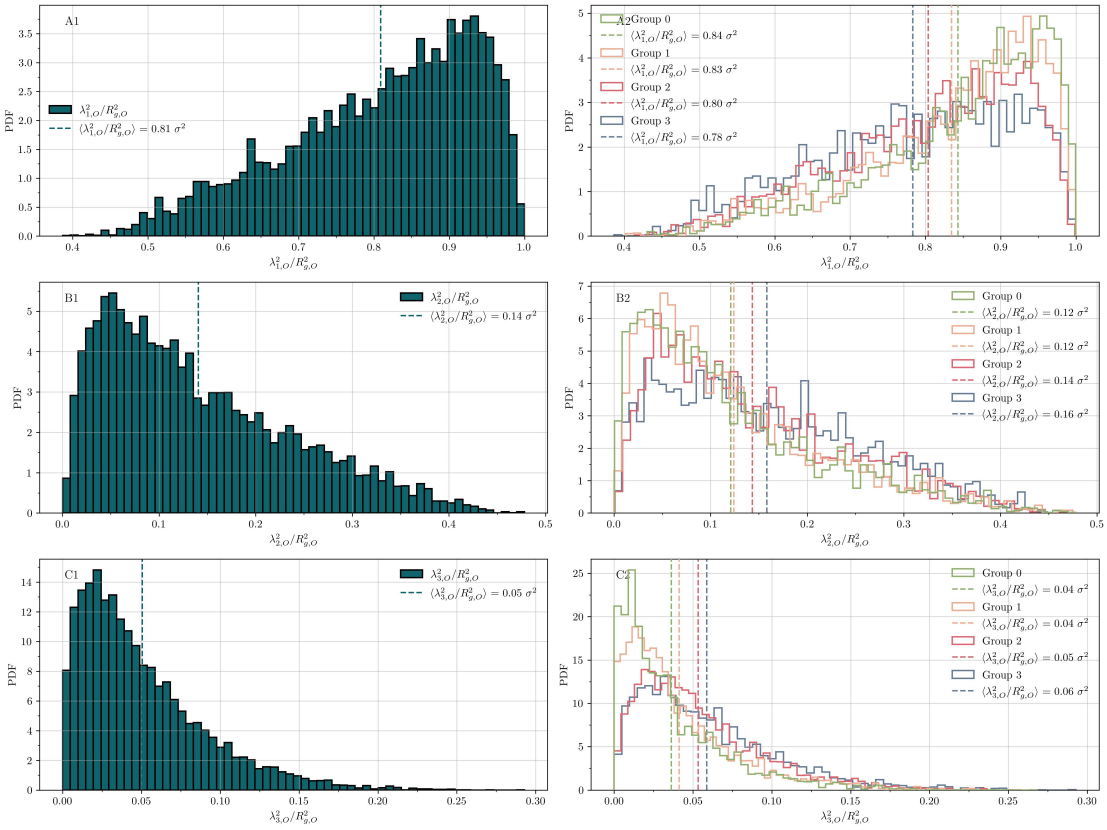

Figure 5.25.: Distributions of the eigenvalues of the gyration tensor for monomers within the intersecting region between the polymer pair, calculated from the sub-set of 3500 random samples from each group, respectively, for time-series TS_4 of a shear simulation with Wi = 8.8. Panel A shows the overall distribution for all pairs with $\xi > 0$, while panel B shows the group-dependent distributions.

6. Conclusions and Outlook

In this study, we successfully devised and implemented a deadlock detection method that allows for the identification of deadlocked pairs within ring polymer melt systems. Unlike the original method [8], which chose cutting points furthest away from the common center of mass, our version of the algorithm incorporates the results from multiple reconnections of the same pair at the same timestep. With this modification, we introduce a new measure: the *degree of deadlocking* ξ, a statistical measure that characterizes the deadlocked state. This measure has proven useful in distinguishing between loose and tight knots and allowed us to investigate and characterize the behavior of deadlocks with a similar value of ξ. Using the modified version of the deadlock detection algorithm, we were able to distinguish between different deadlocked states which paved the way to characterize their different behavior.

We applied our deadlock detection algorithm to equilibrium conformations of a ring polymer melt, with the overall goal to investigate whether deadlocked structures are a natural feature of the rings equilibrium state. We found that while deadlocks naturally emerge in the equilibrium state (in the absence of external stresses), the number of deadlocked pairs is generally low, accounting for $\sim 1\%$ of linearly non-separable pairs. Most of these deadlocked pairs exhibit a low degree of deadlocking, with highly deadlocked pairs being extremely rare. Further investigation of the persistence of deadlocked pairs shed light on the time scales associated with the formation and disappearance of deadlocked structures. Slightly deadlocked pairs were found to disentangle rapidly, typically within less than $0.04\tau_D$, driven by random fluctuations. In contrast, highly deadlocked pairs remain meta-stable in equilibrium for time periods extending beyond the observation window of $4.56\tau_D$. We also observed that the total number of deadlocked pairs in each group remained stable, showing no significant drift over time. This suggests that the formation and disappearance of deadlocked pairs is balanced, indicating an equilibrium state. While these highly deadlocked pairs are rarely formed and equally rarely disentangle, the correlation function shown in Figure 4.7 indicates that about 80% of these pairs experience group-membership changes at least once during the observation period. This suggests that although highly deadlocked pairs remain meta-stable, they undergo conformational changes that influence their degree of deadlocking. However, the question of how long highly deadlocked pairs remain locked before becoming disentangled remains unanswered. Answering this would require tracking these pairs over extended periods, which we plan to do in the future. An analysis of the conformational states of the deadlocked pairs revealed that highly deadlocked pairs tend to adopt compact shapes, with their centers of mass positioned close together and significant overlap in volume. In contrast, loosely deadlocked pairs exhibit more elongated structures, particularly along

the first principal axis, suggesting a rod-like conformation of the pair. These loosely deadlocked pairs typically have larger separations between their centers of mass and minimal overlap, highlighting the differences in structural properties between the two groups. While their two-ring properties show clear distinctions between different groups, the individual rings conformation is *not* influenced by the fact that this ring is part of a deadlock. When examining the motion of individual polymer chains in equilibrium, we found that the degree of deadlocking has little impact on the mobility at time-scales comparable to the diffusion time. However, at longer time-scales, different diffusive regimes *may* emerge for different groups, with pairs in tighter deadlocked configurations exhibiting slower diffusion. As the deadlock forces the two chains to move coherently, a deadlocked pair has a higher effective mass compared to a single, freely moving ring, potentially leading to slower diffusion. However, the distribution of $g_3(\Delta t)$ for highly deadlocked pairs is quite noisy and the differences in $g_3(\Delta t)$ between groups fall within the standard deviation. While we suspect that different diffusive regimes may emerge at longer time-scales, the statistical error in $g_3(\Delta t)$ prevents us from drawing definite conclusions. In contrast, the relative MSD over longer time-scales clearly distinguishes between different groups. Loosely deadlocked pairs, which have a shorter survival time, typically disentangle quickly, breaking the topological constraint and allowing the rings to move independently. Two unconstrained pairs are more likely to diffuse in different directions, as indicated by the rapid increase in $g_{rel}(\Delta t)$ for Group 1. In contrast, the $g_{rel}(\Delta t)$ for highly deadlocked pairs plateaus, suggesting a maximal separation distance between the two rings. Notably, the plateau value of $g_{rel}(\Delta t)$ is comparable to the pair's radius of gyration and the distance between their centers of mass, confirming that a conformation with a high degree of deadlocking represents a strongly entangled two-ring state.

While we thoroughly characterized the behavior of deadlocked pairs in equilibrium, no single static or dynamic quantity was found to correlate strongly with the degree of deadlocking. Even when combining static and dynamic properties, no strong correlations emerged, highlighting the need of the topological features of our deadlock detection algorithm. Nevertheless, we did observe a significant correlation between the longest survival time and the degree of deadlocking. This supports the meta-stable nature of highly deadlocked pairs, setting them apart from loosely deadlocked pairs, which undergo rapid disentangling.

We extended our investigation to study the behavior of deadlocked pairs under steady-state shear, examining two different shear rates: Wi = 8.8 and Wi = 30.0. The goal of this investigation was to explore how the composition and properties of deadlocks are affected by shear forces and to investigate any potential correlations between deadlocks and the viscoelastic properties of the melt. Our results show that, for both shear rates, deadlocked structures were not only formed under shear, but the total number of deadlocks was significantly higher than in equilibrium. This is especially pronounced for highly deadlocked pairs, where the number of pairs in Group 3 is more than 15 times greater than in equilibrium. At both shear rates, the population in Group 3 exceeded that of Group 2, contrasting

with the equilibrium state where the opposite trend is observed. Interestingly, when comparing the two shear rates, the number of pairs with $\xi > 0.1$ remains constant, while the population of Group 1 increased by a factor of two for Wi = 30.0 compared to Wi = 8.8

We observed periodic peaks in the population of Groups 2 and 3 at both shear rates, suggesting an underlying physical mechanism driving the formation of deadlocked pairs. These peaks coincided for Group 2 and 3, indicating that the behavior of deadlocks in these groups is influenced by the same underlying cause. In contrast, Group 1 was unaffected by these large periodic fluctuations and displayed normal fluctuations around its mean value. The cause of these periodic fluctuations remains unclear, though we suspect a connection to the tumbling dynamics of polymers. Further investigation is needed to confirm this hypothesis.

The investigation into the persistence of deadlocked structures revealed that most pairs, regardless of their group membership, disentangle within the first analyzed timestep, corresponding to a time-scale comparable to the inverse shear rate τ_{sr}. For both shear rates, $30\tau_{sr}$ is sufficient to disentangle all pairs in Group 1, highlighting their limited survival time. While most highly deadlocked pairs disentangle within the observation window, some persist for longer timescales. We found that, across all groups, deadlocked pairs undergo rapid conformational changes influencing their degree of deadlocking, as seen in the rapid decay of the group-dependent autocorrelation functions after the first analyzed timestep. Since these disentangling mechanisms occur within timescales of τ_{sr}, we plan to evaluate conformations on shorter timescales to better understand the precise nature of deadlock formation under shear.

An analysis of the static properties of deadlocked pairs reveals that the structural properties of loosely and highly deadlocked pairs were largely indistinguishable. An investigation of the center of mass distance between two deadlocked rings for Wi = 8.8 revealed a bimodal distribution for Group 0, which also appeared in the maximal intermonomer distance. The cause of this behavior remains unidentified, and we plan to further investigate this unusual observation. We also found that the properties of the deadlocked region different when comparing shear rates. For Wi = 8.8, the overlapping volume function peaks at very low values, suggesting that most pairs have limited overlap between the rings. For Wi = 30.0, the mean overlapping volume increases substantially, indicating that higher shear rates lead to more significant overlap between rings. Further analysis of the overlapping region shows that the overlap distribution followed the same trend across all groups. For Wi = 8.8, the overlapping region is likely a single, continuous region where the deadlock is localized, whereas for Wi = 30.0, the overlapping region exhibits more variability. While some pairs still have small, localized overlapping regions, more substantial overlaps do occur.

While we gained some insight into how deadlocks behave under shear, many open questions remain, and further investigation is needed to fully understand the dynamics of

deadlocks under shear. We briefly outline our plans for future studies:

- We have analyzed only two shear rates so far. To gain a deeper understanding of how the behavior of deadlocks change under shear conditions, we plan to evaluate deadlocked configurations for at least five more different shear rates.
- Given that much of the deadlock dynamics occurs within timescales of τ_{sr}, we plan to analyze conformations at smaller time scales to gain a better understanding of the underlying mechanisms.
- We plan to investigate the tumbling behavior of rings to see if it is correlated with the periodic peaks observed in the number of deadlocks over time.
- Unlike in the equilibrium state, the degree of deadlocking for shear does not correlate strongly with the survival time of deadlocked structures. Although ξ can distinguish between short-lived Group 1 deadlocks, it is insufficient to differentiate between short- and long-lived deadlocks in Groups 2 and 3. We plan to investigate other properties that may be more predictive of the survival behavior of deadlocks under shear.
- We aim to get further insight into the formation dynamics of deadlocks under shear and to understand the factors that drive their formation.

Bibliography

[1] PG de Gennes. *Scaling Concepts in Polymer Physics*. Cornell University Press, 1979.

[2] M Doi, S F Edwards, and S F Edwards. *The theory of polymer dynamics*, volume 73. oxford university press, 1988.

[3] M Kapnistos, M Lang, D Vlassopoulos, W Pyckhout-Hintzen, D Richter, D Cho, T Chang, and M Rubinstein. Unexpected power-law stress relaxation of entangled ring polymers. *Nature materials*, 7(12):997–1002, 2008.

[4] D Parisi, S Costanzo, Y Jeong, J Ahn, T Chang, D Vlassopoulos, J D Halverson, K Kremer, T Ge, M Rubinstein, et al. Nonlinear shear rheology of entangled polymer rings. *Macromolecules*, 54(6):2811–2827, 2021.

[5] T McLeish. Floored by the rings. *Nature materials*, 7(12):933–935, 2008.

[6] Q Huang, J Ahn, D Parisi, T Chang, O Hassager, S Panyukov, M Rubinstein, and D Vlassopoulos. Unexpected stretching of entangled ring macromolecules. *Physical review letters*, 122(20):208001, 2019.

[7] T C O'Connor, T Ge, M Rubinstein, and G S Grest. Topological linking drives anomalous thickening of ring polymers in weak extensional flows. *Physical review letters*, 124(2):027801, 2020.

[8] C Micheletti, I Chubak, E Orlandini, and J Smrek. Topology-based detection and tracking of deadlocks reveal aging of active ring melts. *ACS macro letters*, 13(2):124–129, 2024.

[9] M Rubinstein and R H Colby. *Polymer Physics*. Oxford Press, 2003.

[10] X Xu, J Chen, and L An. Shear thinning behavior of linear polymer melts under shear flow via nonequilibrium molecular dynamics. *The Journal of chemical physics*, 140(17), 2014.

[11] R Everaers, H Karimi-Varzaneh, F Fleck, N Hojdis, and C Svaneborg. Kremer–grest models for commodity polymer melts: Linking theory, experiment, and simulation at the kuhn scale. *Macromolecules*, 53(6):1901–1916, 2020.

[12] K Kremer and G S Grest. Dynamics of entangled linear polymer melts: A molecular-dynamics simulation. *The Journal of chemical physics*, 92(8):5057–5086, 1990.

[13] J D. Weeks, D Chandler, and H C Andersen. Role of repulsive forces in determining the equilibrium structure of simple liquids. *The Journal of chemical physics*, 54(12):5237–5247, 1971.

[14] G S. Grest and K Kremer. Molecular dynamics simulation for polymers in the presence of a heat bath. *Phys. Rev. A*, 33:3628–3631, May 1986.

[15] W L Mattice. *Conformational theory of large molecules : the rotational isomeric state model in macromolecular systems*. A Wiley Interscience publication. Wiley, New York, NY, 1994.

[16] D N Theodorou and U W Suter. Shape of unperturbed linear polymers: polypropylene. *Macromolecules*, 18(6):1206–1214, 1985.

[17] J D. Halverson, W B Lee, G S. Grest, A Y Grosberg, and K Kremer. Molecular dynamics simulation study of nonconcatenated ring polymers in a melt. ii. dynamics. *The Journal of Chemical Physics*, 134(20):204905, 05 2011.

[18] C Schneck, J Smrek, C N Likos, and A Zöttl. Supercoiled ring polymers under shear flow. *Nanoscale*, 16(18):888–8899, 2024.

[19] L Tubiana, G P Alexander, A Barbensi, D Buck, J H E Cartwright, M Chwastyk, M Cieplak, I Coluzza, S Čopar, D J Craik, M Di Stefano, R Everaers, P F N Faísca, F Ferrari, A Giacometti, D Goundaroulis, E Haglund, Y Hou, N Ilieva, S E Jackson, A Japaridze, N Kaplan, A R Klotz, H Li, C N Likos, E Locatelli, T López-León, T Machon, C Micheletti, D Michieletto, A Niemi, W Niemyska, S Niewieczerzal, F Nitti, E Orlandini, S Pasquali, A P Perlinska, R Podgornik, R Potestio, N M Pugno, M Ravnik, R Ricca, C M Rohwer, A Rosa, J Smrek, A Souslov, A Stasiak, D Steer, J Sułkowska, P Sułkowski, D W L Sumners, C Svaneborg, P Szymczak, T Tarenzi, R Travasso, P Virnau, D Vlassopoulos, P Ziherl, and S Žumer. Topology in soft and biological matter. *Physics reports*, 1075:1–137, 2024.

[20] C C Adams. *The knot book : an elementary introduction to the mathematical theory of knots*. Freeman, New York, NY, 1994.

[21] E Orlandini and S G Whittington. Statistical topology of closed curves: Some applications in polymer physics. *Reviews of modern physics*, 79(2):611–642, 2007.

[22] C Livingston. *Knot theory*. The Carus mathematical monographs ; 24. Math. Assoc. of America, Washington, DC, 1993.

[23] M P Allen and D J Tildesley. *Computer Simulation of Liquids*. Oxford University Press, 06 2017.

[24] L Verlet. Computer "experiments" on classical fluids. i. thermodynamical properties of lennard-jones molecules. *Phys. Rev.*, 159:98–103, Jul 1967.

[25] P H Hünenberger. Thermostat algorithms for molecular dynamics simulations. *Advanced computer simulation: Approaches for soft matter sciences I*, pages 105–149, 2005.

[26] S Nosé. A unified formulation of the constant temperature molecular dynamics methods. *The Journal of Chemical Physics*, 81(1):511–519, 07 1984.

[27] S Li and J Li. *Introduction to Computational Nanomechanics: Multiscale and Statistical Simulations*. Cambridge University Press, 2022.

[28] F Müller-Plathe. Reversing the perturbation in nonequilibrium molecular dynamics: An easy way to calculate the shear viscosity of fluids. *Phys. Rev. E*, 59:4894–4898, May 1999.

[29] B D Todd and P J Daivis. *Homogeneous Flows for Molecular Fluids*, page 229–265. Cambridge University Press, 2017.

[30] A P Thompson, S J Plimpton, and W Mattson. General formulation of pressure and stress tensor for arbitrary many-body interaction potentials under periodic boundary conditions. *The Journal of chemical physics*, 131(15), 2009.

[31] A P Hompson, H M Aktulga, R Berger, D S Bolintineanu, W M Brown, P S Crozier, P J in 't Veld, A Kohlmeyer, S G Moore, T D Nguyen, R Shan, M J Stevens, J Tranchida, C Trott, and S J Plimption. LAMMPS - a flexible simulation tool for particle-based materials modeling at the atomic, meso, and continuum scales. *Comp. Phys. Comm.*, 271:108171, 2022.

[32] F P Preparata and M I Shamos. *Computational geometry: an introduction*. Springer Science & Business Media, 2012.

[33] C H Papadimitriou and K Steiglitz. *Combinatorial optimization: algorithms and complexity*. Courier Corporation, 1998.

A. Appendix

A.0.1. Equilibrium Simulation Parameters and Protocol

We provide a detailed overview of the implementation of the interaction potentials, the integration scheme and the thermostat used for the molecular dynamics simulation of ring polymers in equilibrium. This section serves as a comprehensive guide to the simulation parameters and their corresponding LAMMPS [31] commands for readers interested in the technical details of the implementation.
In LAMMPS, the WCA interaction is defined using the following commands:

```
pair_style lj/cut 1.122462048                    (A.1)
pair_coeff * * 1.0 1.0 1.122462048               (A.2)
pair_modify shift yes                            (A.3)
```

Equation A.1 defines the Lennard-Jones potential with a cutoff distance of 1.122462048σ. Equation (A.2) specifies the coefficients for the WCA potential, where the first two values (1.0 and 1.0) define the interaction strength (ϵ) and the monomer diameter (σ), respectively. The third value, 1.122462048σ, sets the cutoff distance, beyond which the potential is considered to be zero. Finally, equation (A.3) shifts the potential to zero at the cutoff distance, ensuring the potential is smooth and continuous.
The FENE potential in LAMMPS is specified by the following commands:

```
bond_style fene                                  (A.4)
bond_coeff 1 30.0 1.5 1.0 1.0                    (A.5)
```

In equation A.4, the `bond_style` command defines the FENE potential for bonds between monomers. The `bond_coeff` command in equation A.5 specifies the parameters for the FENE potential, where the first parameter (1) identifies the bond type, while the second value (30.0) sets the spring constant K_0 of the potential. The third value, $R_0 = 1.5\sigma$, specifies the maximum bond length and the final two values (1.0 1.0) are specific to the FENE potential's behavior in the simulation.
The cosine bending potential is specified with the following commands:

```
angle_style cosine                               (A.6)
angle_coeff 1 1.5                                (A.7)
```

The `angle_style` command defines the cosine bending potential, while the `angle_coeff` command (A.7) sets the bending stiffness coefficient K_θ. The value of 1.5 corresponds to a moderate stiffness, typical for polymer systems that are neither too rigid nor too flexible.
With the interaction potentials set, we proceed with time integration. The Velocity Verlet algorithm, described in section 3.1.2, was used to propagate the system forward in time. The parameters for the Langevin thermostat were set as follows:

```
neighbor 0.3 bin
```
(A.8)

```
neigh_modify every 2 delay 0 check yes
```
(A.9)

```
fix 1 all nve
```
(A.10)

```
fix 2 all langevin 1.0 1.0 1.0 42
```
(A.11)

In these equations, the `neighbor` and `neigh_modify` commands control the neighbor list update frequency and the binning method used for efficient interaction calculations. The `fix 1 all nve` commands sets the system to perform an NVE integration. The `fix 2 all langevin 1.0 1.0 1.0 42` command applies the Langevin thermostat, with a damping coefficient $\gamma = 1.0$ to maintain the system at the desired temperature.
Finally, the integration time step for the simulation was set to `0.012`, ensuring numerical stability during the time evolution and the random seed (`42`) was chosen arbitrarily.

A.0.2. Shear Simulation Parameters and Protocol

For the interested reader, we provide a more detailed overview into our simulation protocol used to propagate the steady-state shear system over time, focusing on the explicit implementation in LAMMPS [31]. To compare the response of the ring polymer melt subject to shear flow to their equilibrium counterpart, the potential was set up identically as in the equilibrium simulation, hence we do not repeat this information here. Furthermore, the neighbor list update frequency was set as shown in equation A.8 and A.9.
The first LAMMPS command that deviates from the equilibrium simulation protocol is to change the simulation box to a triclinic box. Periodic boundary conditions can be implemented by Lees-Edwards Boundary conditions, or equivalently, tilting the simulation box as a function of time. The LAMMPS command is

```
change_box all triclinic units box,
```
(A.12)

where the parameter `all` applied the changes to all atoms in the simulation, `triclinic` specifies the box geometry and `units box` ensures that the box is defined in terms of LAMMPS units.

The `fix` command

```
fix 1 all nvt/sllod temp 1.0 1.0 1.0
```
(A.13)

sets the integration method in combination with setting the thermostat. The parameter `all` applies the fix to all monomers in the simulation box. `nvt/sllod` sets the integration scheme, which is integrated with the atomistic SLLOD equations of motion, applying the streaming term at the position of each monomer. The command `temp 1.0 1.0 1.0` sets a Nosé-Hoover thermostat for the simulation with a target temperature of `1.0` and a temperature damping parameter of 1.0 in reduced time units.
The line

```
fix 2 all deform 1 xy erate ${sr} remap v
```
(A.14)

applied a shear deformation to the system. `deform` deforms the simulation box at a constant shear rate along the `xy` plane, set by the shear rate input parameter `${sr}`. `remap v` ensures that the monomers velocities are adjusted as the box is deformed.
Finally, the integration step for the shear simulation is set to `0.005`.